DESIGN, FABRICATION AND TEST OF SURFACE TENSION-DRIVEN MICROBOATS AND THERMALLY OSCILLATORY BUBBLE-PROPELLED MICROSUBMARINES

by

LEI QIAO

Presented to the Faculty of the Graduate School of

The University of Texas at Arlington in Partial Fulfillment

of the Requirements

for the Degree of

DOCTOR OF PHILOSOPHY

THE UNIVERSITY OF TEXAS AT ARLINGTON

August 2013

ACKNOWLEDGEMENTS

I would never have been able to finish my dissertation without the guidance of my committee members, help from friends, and support from my family.

First of all, I would like to thank my advisor Dr. Cheng Luo, who provided me the opportunity to work in his outstanding group and also encouraged and challenged me throughout my academic program. I joined his group in fall 2008. Before that I did not have any background in MEMS. He patiently brought me to this exciting research field. During the past five years under his supervision, I have been impressed by his deep understanding and vision about our research field. He always inspires me to think independently and create new ideas continuously. As a supervisor, he will not only ask me to finish some projects, but also teach me how to think. Five years later, I am not only skilled in microfabrication but understand the principles as well. What is most valuable is that Dr. Cheng Luo gives me the key to explore and see the whole different world under the microscope. Also he supported me to attend several top academic conferences in MEMS to present my research results.

Second, I would like to thank my advisory committee members, Dr. Bo Yang, Dr. Frank K. Lu, Dr. Haiying Huang and Dr. Hyejin Moon. They gave me lots of advice and help for this dissertation. I also thank all the faculty and staff in the Department of Mechanical and Aerospace Engineering at University of Texas at Arlington, especially the staff in Nanofab who trained and helped me with the fabrication of devices.

Third, I thank my friendly group members, Xinchuan Liu, Hao Li, Hui Wang, Neal Bowden, Anirban Chakraborty, Di Xiao, Mingming Xiang, Xin Heng, Zhihui Lu, Varun Garg, and Prasha Sarwate for their co-operation and continuous support.

Finally (but not the least), during my Ph.D. study, my parent and friends gave me a lot of supports. You are always most important to me. Life is not always easy. When things do not

go well, it is your company and supports that keep me face challenge with a smile. When wonderful things happen, it is the most enjoyable part that I can share with you. I always love you!

July 01, 2013

ABSTRACT

DESIGN, FABRICATION AND TEST OF SURFACE TENSION-DRIVEN MICROBOATS AND THERMALLY OSCILLATORY BUBBLE-PROPELLED MICROSUBMARINES

Lei Qiao, PhD

The University of Texas at Arlington, 2013

Supervising Professor: Cheng Luo

In this work, we develop microboats and microsubmarines, which are capable of moving on and under water, respectively.

The microboat is propelled due to the difference between surface tensions around stern and bow. This difference is generated by releasing a liquid with lower surface tension than water from the stern. We explore both horizontal and vertical motions of the microboats through a combination of experimental and theoretical investigations. It has a length of 8 mm and weight of 20 mg with the highest speed of 25 cm/s and travel distance of 85 cm. Moreover, we design, fabricate and test microboats with rudders. Such a microboat is capable of having a radial motion in an open water area. The radii of the motion are controlled by lengths of the rudders.

The microsubmarine is also designed, fabricated and tested. It is driven by thermally oscillatory bubbles. A submarine has a length of 8 mm and weight of 40 mg. Its thrust can be as large as 67.6 nN when applied voltage, pulse frequency and duty are, respectively, 16 V, 100 Hz and 50%. Its travel distance is 1.28 cm with the highest speed of 1.8 mm/s. A micro

submarine is further incorporated with micropillars to be able to float up from the under water. After this incorporation, micro submarine may still rise up to water surface from the bottom of water tank even if it is denser than water.

TABLE OF CONTENTS

LIST OF ILLUSTRATIONS

LIST OF TABLES

CHAPTER 1

INTRODUCTION AND DISSERTATION OVERVIEW

1.1 Introduction

Similar to what boats and submarines are, microboats and microsubmarines might be used to transport targets of interest from one place to another for microfluidic applications. Although a variety of MEMS devices that are capable of walking [1-4] and flying [5-8] have been developed, little work has been done on those that can move in liquids. Therefore, our group has recently developed microboats [9-12], microflotillas [13-14] (each microflotilla consists of an array of linked microboats), and microsubmarines. This dissertation aims to (i) test translational and rotational motions of microboats, (ii) investigate the circular motions of microboats with rudders, (iii) develop microsubmarines that are driven using thermally oscillatory approaches, and (iv) introduce a technique to let the underwater vehicle with higher density than water float up from under the water.

Previous work mainly focused on horizontal motions of microboats [9]. We would like to further consider translational and rotational motions of a mm-scaled SU-8 boat in the vertical plane, which are also called squat and trim phenomena, respectively, in the case of a macroboat. Through two types of tests, we demonstrated that dramatic squat and trim phenomena observed in the motions of the SU-8 boat were mainly induced by the surface tension difference between water and isopropyl alcohol (boat propellant), instead of horizontal movements of the miniaturized boat. This difference created a hollow spot behind the stern and made the boat sink and tilt along the sidewall of the hollow spot. In addition, we found that the motion of an SU-8 boat in a channel consists of two stages. In the first stage, it is propelled by the difference between fore-and-aft surface tensions. In addition to moving forward, it also had

dramatic squat and trim movements. However, in the second stage, in which no more isopropyl alcohol exited the boat, it is driven by a water wave generated in the first stage and did not show any visible squat and trim phenomena. The results of this work provided a better understanding of motions of the SU-8 boats. These results might also apply to surface tension-driven motions of other miniaturized objects.

Second, due to lack of steering systems, microboats and microflotillas that have been developed to date can move along their longitudinal directions, but are unable to execute radial motions in an open area. Therefore, a side rudder is incorporated into an existing microboat to allow a radial motion of this micro transportation device. On simple and early watercrafts, a stick or pole might act as a rudder to turn a boat. To date, rudders are extensively used in steer a conventional ship, boat, submarine, hovercraft, and aircraft. On a boat, a rudder operates by re-directing the fluid past the hull, thus imparting a turning or yawing motion to the ship. Basically, a rudder is a flat plane or a sheet of material attached with hinges to the craft's stern or tail. A rudder is incorporated into one side of a microboat, creating a radial motion. The radius of this motion depends on the length of the rudder.

Third, the aforementioned microboats are driven due to the difference between fore-and-aft surface tensions. Accordingly, they are mobile on a water surface, while not submerged. In addition to microboats, we also desire to develop microsubmarines that are able to move under water. The first prototype of conventional submarines was built in 1620 by Cornelius Jacobszoon Drebbel (a Dutchman). Currently, submarines are widely employed for military and civil uses, such as defense, exploration, tourism, oil and gas platform inspections, and pipeline surveys. Likewise, microsubmarines can also be employed on demand, for example, to deliver chemical and biological solutions in microfluidic applications, or to carry sensors for detecting targets in liquids. Existing approaches use stationary devices for material supply and sensing detection. Compared with these stationary devices, microsubmarines will be mobile. This enables the microsubmarines to actively deliver materials and sensors according to in-situ

needs. For example liquid mixing is important for the success of the micro-total analysis system [23]. Several approaches have been proposed by researchers to enhance mixing results, including dividing liquids into tiny drops followed by mixing [24], control of the injection of two mixing liquids [25] and thermal-bubble actuation [26]. These approaches have a common point: the control of the mixing happens at a particular point with the aid of an external device. However, microsubmarines can actively promote the mixing throughout a microchannel via traveling through the channel and delivering materials simultaneously. Also, the liquids can be mixed at a desired location by stopping a microsubmarine at the location. Furthermore, a microsubmarine can carry sensors through a toxic liquid environment on its own, scanning the whole environment and giving much more information than stationary sensors. Based on the feedback, the submarine can carry sensors again to particular points for specific detection.

Fourth and finally, we would like to make micro submarine floating up from under water. Due to the difficulty of fabrication of sealed tank into a micro vehicle, we explored a novel technique to decrease the average density of the micro submarine. This method has simple structure. This structure can be fabricated by one time UV-Lithography. We call these structure micropillars. Micropillars can be incorporated on to the surface of a micro vehicle (microsubmarine for example). Air is trapped in between micropillars, so the average density of the micro submarine is lowered. This micropillars-covered surface is a super hydrophobic surface. Initially, this effect was observed on some self-clean plants, such as lotus and colocasia, which can form spherical (super-hydrophobic) water droplets on their leaves in rain, fog and dew to avoid getting wet. This phenomenon is usually called the ‘lotus effect’ [15]. It was found that the microstructures on the leaves played a great role in this effect [16]. This motivated researchers to modify the wettability of the surface of a certain material through changing the roughness of the surface. Singh et al. [17] replicated surfaces of lotus and colocasia leaves onto thin polymeric films using a capillarity-directed soft lithographic technique. Onda et al. [18] demonstrated a superwater-repellent fractal surface made of alkylketene dimer.

Bico et al. [19] examined the water droplets on three surfaces with different microstructures, such as spikes, shallow cavities and stripes. They found that the contact angle can be predicted and thus quantitatively tuned by the design of the surface microstructure. Nosonovsky and Bhushan [20] built an analytical model to provide a relationship between local roughness and contact angle and created super-hydrophobic surfaces through patterning. The super-hydrophobic surfaces may reduce the frictional drag force pressure that is needed to drive a flow forward. Joseph et al. [21] tested the flow slippage over super-hydrophobic surfaces made of carbon nanotube forests in microchannels. Other than that, because super-hydrophobic surfaces were proven to have the ability to trap air, they have a potential to reduce the mean density of small object. This may make the object with higher density than water float up to the water surface when submerged. It is known that when a solid fragment has a higher density than water, it may still float on water surface due to the support of surface tension. However, once the solid fragment is completely immersed in water, it sinks down to due to elimination of the surface tension. In this work, we demonstrate that, after the incorporation of micropillars on such a solid fragment, it may still return to the water surface. The air trapped between micropillars increases the space that the solid fragment occupies under water. Accordingly, the buoyancy is increased. The critical values of trapped air, micropillar-covered area, micropillar height and water depth for a micropillar-covered fragment to rise up to water surface were formulated. Four micropillar-incorporated SU-8 fragments were fabricated and tested to validate the derived relationships. Experimentally determined critical values of micropillar-covered areas and trapped air volumes match well with theoretically predicted ones. In addition, through force analysis, we showed that surface tension at the triple lines between water, micropillars and trapped air retains the volume of the trapped air but does not provide any lifting force to make the fragment rise up to water surface. Since the incorporation of the micropillars may make a completely immersed fragment get back to water surface, the presented results have potential applications in developing miniaturized devices, such as micro submarines, under water robots

and so on.

1.2 Technical Review on Miniaturized Objects that are Mobile in Liquid Environment

Since the 1990s, there have been significant research efforts devoted to the development of micro-scale objects that are mobile in a liquid environment. However, engines or motors, which are considered as the most common machines, are not applicable in MEMS devices because their complicated systems cannot be fabricated using standard micro fabrication techniques. In addition, along with miniaturization the surface force is inversely proportional to volume force, which causes failure when applying macroscopic concepts directly to microscopic cases. Normally there are two approaches to overcoming these challenges. The first approach uses various actuators which have a structure that can be microfabricated to provide propulsive forces, while the propulsion in the second approach is based on surface tension gradient around objects. Researches turn to use fin-like propeller through various driving schemes such as SMA (shape memory alloy) actuator, IPMC (ionic polymer-metal composite) actuator, PZT (lead zirconate titanate, a type of piezoelectric material) actuator, and ICPF (ionic conducting polymer film) actuator [27-38]. The second approach uses a surface tension gradient induced chemically, electrically, or thermally [39-46]. In addition, researches are also full of enthusiasm in developing novel actuators [47-49].

1.2.1 Fin-like Propeller-driven Objects

Commonly used fin-like actuators can be classified into three groups. They are shape-memory alloys, piezoelectric materials, and ionic polymer-metal composites. Compared to traditional motors, they are all light-weighted. However, these actuators have different disadvantages. Shape memory alloys need external condition to activate its one-time shape change. A shape memory alloy cannot output a continuous mechanical motion. Besides, the actuating speed and force are both low. Ionic polymer-metal composite also have slow actuating speed. Furthermore, the power consumption is very high. Compared to the previous

two kinds, piezoelectric materials have higher working efficiency. However, manual assembly is needed to fabricate the fin-like propeller-driven devices no matter which actuator. Accordingly, it is difficult to fabricate micro versions of due to difficulty of manually assembling the tiny components.

1.2.2 Surface tension-driven Objects

As long as the miniaturization of objects, the surface tensions applied on the object will dominant. There are three dimensionless number helps us to judge the weight of the surface tension force also called capillary force. These are Weber number, Capillary number, and Bond number. Weber number is the ratio between inertial force and capillary force. When it is small, the intermolecular interactions take the control of the bulk flow. Capillary number is the ratio between viscous force and capillary force. When it is small, we consider the viscous force as a minor. Bond number is the ratio between gravitational force and the capillary force. The capillary force dominants when this number is small. As an example, the water strider can walk on water because the capillary force dominants over gravitational forces.

Surface tension gradients may induce movements of a liquid droplet on the surface of another liquid. For example, when a drop of alcohol is laid on the middle of water, the water rushes away from the middle which creating a hollow spot. Water has a higher surface tension than alcohol. As such, more watery portion draws itself away from the more alcoholic portion, as interpreted by Thomson [41]. Surface tension gradients may also cause movements of a floating solid fragment on a liquid surface. These surface tension-driven motions of liquids and solid fragments are so-called Marangoni effect [42]. In the past 15 years, this effect has been applied to drive gels, whose dimensions ranged from millimeter to centimeter scales [43-46]. A gel was firstly immersed in a liquid (such as ethanol) and then placed in water. This liquid has a lower surface tension than water. Once it is expelled from the gel, the surface tension difference between water and the liquid enables the gel to have translational and rotational motions. These motions depend on the size, shape, symmetry, and spouting hole of the gel. A gel of a smaller

size might move faster [43]. Disk- [43, 44] or rectangular-shaped gels [46] mainly had translational motions, while cubic- [44] or Y-shaped gels [46] had rotational motions. Our group also demonstrated an mm-scale SU-8 microboat and microflotilla using IPA as propellant [9-11], which had a longitudinal speed at 0.1 m/s. Instead of changing the surface tension distribution by chemical approaches, Chung et al. also reported using a EWOD approach (electowetting-on-dielectric) [39]. It was demonstrated that after applying 160V on electrodes attached on boat and in water separately, an mm-scale boat would move and steer on the water surface. Another kind of surface tension driven MEMS device, water strider robot, was demonstrated in Song et al. [40]. The driving forces were generated mechanically by motion of strider legs. Although much works had been done utilizing surface tension as the driving force, the motion of objects is restricted to the water surface. Despite a large amount of effort, few control theorems have been developed. More effort needs to be done on control theorem development.

1.2.3 Objects driven by other approaches

Moreover, a microsubmarine was developed which can float upward or sink downward by thermopneumatic mechanism [47]. When heat is applied to the air trapped in a close chamber, the chamber expands and microsubmarine floats upward. It can also moving forward by generate steam bubble to one side of microsubmarine. The demonstrated moving distance is 1.7 mm. In addition, researchers developed a micro-boat propelled by electrohydrodynamic mechanism [48]. This method uses a coulomb force which interacts between the induced electrical charges in liquid and the electrical field. This force transfers momentum to the fluid and the reactant force propel the micro-boat forward. It can travel 0.15 mm in 2 seconds with an applied potential of 30 V DC. Third, a pond skater was propelled by electrowetting on dielectric mechanism [49]. It traveled 1.35 mm with a speed of 0.8 mm/s under contraints of gold wires. A wireless powered pond skater was also developed and demonstrated, but the travel distance was still limited by the mechanism of the propulsion. Those three approaches are applied to actuate small objects in liquids. Nevertheless, it appears that the corresponding thrusts may not

be large, since the total travel distances are 1.7 mm [47] or less [48,49].

In Table 1.1, the aforementioned propulsive approaches for small water vehicles are categorized and summarized. The details of sizes, motions and power consumptions of various small vehicles driven by different propulsive approaches are given and compared. Surface tension driven mechanism is able to actuate a comparatively small object (for example: has a length of mm-scale and a weight of dozens of mg) to travel with a high speed (order of 10 cm/s). Unfortunately, this driving mechanism can only apply on water surface where surface tension exists. Much work has been done on the design, optimization, and fabrication of bio mimic fin-like propellers. More work needs to be done to simplify the fabrication process, shrink the device size, enhance the efficiency, and develop control mechanism. Therefore, other different approaches with simpler structural design and propulsive mechanism are being developed. A novel propulsion technique for a micro-submarine was developed as part of the present research.

Table 1.1: Summarization of the size, motion and power consumptions of various small vehicles driven by different propulsive approaches. (The approaches adopted in this work are labeled with *)

Propulsive approaches	Size		Motions			Power		Year
	Mass (g)	Length (mm)	Maximum Speed (mm/s)	Thrust (μN)	Maximum Travel Distance (cm)	Wireless (Yes/Not)	Power source	
ICPF Fin-Like Actuator [27]	0.6	40	5.35	4	1	No	2 V 0.14 A 1 Hz electrical pulse	1998
SMA Fin-Like Actuator [28]	30	146	112	N/A	N/A	Yes	Battery cell	2008
IPMC Fin-Like Actuator [29]	16.2	96	23.6	4000	N/A	Yes	Battery cell	2005
IPMC Fin-Like Actuator [30]	1.45	57	7	370	N/A	Not	3 V 4 Hz electrical pulse	2006
PZT Fin-Like Actuator [31]	1	12	N/A	1000	N/A	Not	150 V peak-to-peak sinusoidal voltage	2005
Magnet Fin-Like Actuator [32]	>0.2	40	63	7000	N/A	Yes	40 Hz external magnetic field	2007
FMP Fin-Like Actuator [33]	N/A	20	40	N/A	N/A	Yes	20 Hz 13 mT external magnetic field	2002

Table 1.1 – *Continued*

Propulsive approaches	Size		Motions			Power		Year
	Mass (g)	Length (mm)	Maximum Speed (mm/s)	Thrust (μN)	Maximum Travel Distance (cm)	Wireless (Yes/Not)	Power source	
Surface tension* (chemical) [9]	2×10^{-2}	8.15	250	250	85	Yes	1.5 μl IPA	2008
Surface tension (chemical) [12]	1.3	14	85	631	321	Yes	101 μl IPA	2012
Surface tension (chemical) [45]	0.13	30	70	N/A	N/A	Yes	Tetrahydrofuran (THF)	2000
Surface tension (chemical) [46]	N/A	6	31	N/A	N/A	Yes	Ethanol	2008
Surface tension (EWOD) [39]	N/A	20	4	N/A	N/A	No	160 V 1 kHz AC voltage	2009
Steam Bubble [47]	N/A	3.7	1.7	N/A	0.17	No	6.5 V DC voltage	2011
Electrohydrodynamic [48]	N/A	15	0.11	N/A	0.04	No	40 V DC voltage	2007
Bubble moved by EWOD [49]	0.3	10	8	N/A	0.135	Yes	15 V DC voltage	2009
Thermal Oscillatory bubble*	0.04	8	1.8	0.068	1.26	No	16 V 100 Hz AC voltage	2013

1.3 Dissertation Outline

In chapter one, we introduce research motivations and review approaches used to propel small object in liquid environment. In chapter two, we present trim and squat motions of microboats travelling in a straight channel. In chapter three, we present that design, fabrication and analysis of microboats with rudders. In chapter four, we investigate the design, fabrication and analysis of microboats (or solid fragments) with super-hydrophobic hull. In chapter five, we demonstrate the development of microsubmarines. In Chapter six, we summarize current and near-future work.

CHAPTER 2

DRAMATIC SQUAT AND TRIM PHENOMENA OF MM-SCALED SU-8 BOATS INDUCED BY MARANGONI EFFECT

Surface tension gradients may induce motions of a floating solid fragment. This mechanism has been employed to drive miniaturized objects on a water surface, which could potentially serve as rotators, mixers, locomotives, and so on. To properly apply these objects, it is important to understand their motions. The previous consideration mainly focused on the horizontal motions of these small objects. In this chapter, we considered translational and rotational motions of an mm-scaled SU-8 boat in the vertical plane, which were so-called squat and trim phenomena, respectively, in the case of a macroboat. Through two types of tests, we demonstrated that dramatic squat and trim phenomena observed in the motions of the SU-8 boat were mainly induced by the surface tension difference between water and isopropyl alcohol (IPA, boat propellant), instead of horizontal movements of the miniaturized boat. This difference created a hollow spot behind the stern and made the boat sink and tilt along the sidewall of the hollow spot. In addition, we found that the motion of a SU-8 boat in a channel included two stages. In the first stage, it was propelled due to the difference between fore-and-aft surface tensions. In addition to moving forward, it also had dramatic squat and trim movements. However, in the second stage, in which no more isopropyl alcohol exited the boat, it was driven by a water wave generated in the first stage and did not show any visible squat and trim phenomena. The results of this chapter provided a better understanding of motions of the SU-8 boats. These results might also apply to surface tension-driven motions of other miniaturized objects.

2.1 Introduction

In a recent work, we have developed mm-scaled SU-8 boats [9], whose motions were induced by Marangoni effect. Such a boat comprised two SU-8 layers. The top layer included a reservoir and a nozzle, and the bottom layer sealed the bottom of the reservoir and nozzle. SU-8 is a negative photoresist. Its density was measured to be 1.16×10^3 kg/m^3, slightly larger than that of water (10^3 kg/m3). The surface tension was large enough to overcome this minor difference between the two densities, making the SU-8 float on the water. These SU-8 boats were fabricated in a massive manner using ultra-violet microlithography [9]. An isopropyl alcohol (IPA) solution (91% IPA and 9% water by volume; CVS Pharmacy) was adopted as the propellant. It was loaded into the reservoir of a SU-8 boat using a needle. There was a large difference between surface tensions of IPA and water, which are about 22.8 and 72.8 mN/m, respectively, at 20°C (the temperature at which the experiments were conducted). When the IPA exited the rear of the boat, surface tension behind this boat was reduced, becoming lower than that in front of the boat. This difference in surface tension propelled the boat forward along its longitudinal direction.

The aforementioned structures in chapter 1.2.2 may potentially serve as rotors, mixers, locomotives, etc. For example, Mitsumata et al. [45] employed an mm-scaled gel bar as a rotator. Based on the rotational motions of this rotator, they further constructed a generator, which produced an electric power with an electromotive force as high as 15 mV for over 30 min. On the other hand, in order to properly apply these miniaturized structures, it is important to have a good understanding of their surface tension-driven motions. The previous consideration mentioned above focused on exploration of horizontal motions of the miniaturized structures. In the second chapter, we reported that in addition to making miniaturized SU-8 boats have translational and rotational movements along the horizontal directions, Marangoni effect might also induce translational and rotational movements in the vertical plane, which are so-called squat and trim effects, respectively, in the case of macroboats. The understanding of these

vertical motions would enable better applications of the miniaturized objects.

2.2 Driving Mechanism

The microboat floats on the water supported by the surface tension. When it is totally submerged in water it will sink down to the bottom of the container because it is denser than water. As shown in Fig. 2.1, a microboat includes a reservoir in the rear of boat. IPA is initially applied and stored in the reservoir. Once microboat is placed on the water surface, IPA will contact with water. Then, it will spread on water surface driven by the surface tension gradient and form a layer of IPA liquid on the water surface. This surface tension gradient is generated by the concentration asymmetry of the IPA in water. Simultaneously, it diffuses into water through the interface between water and IPA. Other than that, it evaporates to the air across the IPA air interface. This layer of IPA can stay on the water surface due to its density is lower than that of water. It is important for this motion. We also test to switch the role of IPA and water which means put water in the reservoir and place the microboat on IPA surface. There are no continuous motions observed because water cannot stay on the surface of IPA due to its higher density.

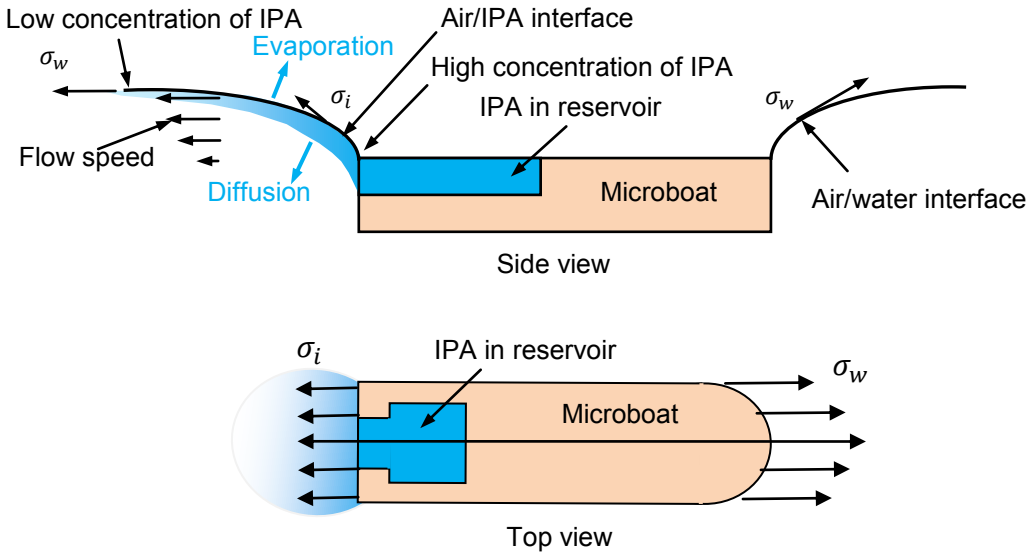

Fig. 2.1: Driving mechanism of surface tension driven microboat.

To understand the physics behind this motion, we first consider the governing equation which approximately describes the gradient of the surface tension. The surface tension distribution can be approximated as:

$$\sigma(c) = \frac{c_0}{c + a}, \tag{2.1}$$

where c_0 and a denote two constant, $\sigma(c)$ the surface tension in the liquid surface, and c_0 / a the surface tension of pure water. When the concentration of the IPA in liquid is 0 or 100, σ equals to 72 or 22 mN/m respectively. During the process of the IPA being released in water, its concentration is affected by Marangoni effect induced convection, gravitational convection, diffusion, and evaporation (Fig. 2.1). To estimate the driving force, we only need to know the distribution of the IPA around the microboat. If we simply consider the concentration of IPA around boat bow and stern are 0 and 100 respectively. Also, during the motion, the effect of the contact angle is too small to be considered. Following Newtonian equation, the motion of the microboat is

$$m\frac{dv(t)}{dt} = F_{drv}W - F_{drg}W, \tag{2.2}$$

where m is the mass, $v(t)$ is the speed, W is the width of the microboat, and F_{drv} and F_{drg} are driving and drag forces on microboat. F_{drv} and F_{drg} and be approximated as [11]

$$F_{drv} = (\sigma_w - \sigma_i)W, \quad \text{and } F_{drg} = \eta v(t)W, \tag{2.3}$$

where σ_w and σ_i are the surface tension of pure water and IPA, and η is a coefficient decided by drag. The experimental results of the longitudinal motion are studied in [9].

2.3 Design And Fabrication

Schematic of a microboat is shown in Fig. 2.2. The microboat comprised two SU-8 layers. The top layer included a reservoir and a nozzle, and the bottom layer sealed the bottom of the reservoir and nozzle. SU-8 was chosen to be the microboat material because of two reasons. First, the density of SU-8 was measured to be 1.16×10^3 kg/m3, slightly larger than that of water (10^3 kg/m^3). The surface tension was large enough to overcome this minor difference between the two densities, making the SU-8 float on the water. Looking into the portion of reservoir, the air water solid interline is on the top corner of the surface of the reservoir. This ensures the contact of the IPA with water during the motion of the boat. Second, SU-8 is a negative photoresist. It can be patterned to desired shapes using UV lithography and its thicknesses can be controlled for producing SU-8 boats with proper thicknesses.

The fabrication of a microboat included three steps (Figs. 2.3a-c): (i) placed a transparency on an S1813-coated silicon wafer, spin-coated the first SU-8 layer on the transparency, and patterned the SU-8 to form the bottom layer of the boat using the UV lithography approach, (ii) spin-coated the second SU-8 layer on the first SU-8 film and produced reservoirs and nozzles in the second SU-8 layer using the UV lithography techniques, and (iii) dissolved S1813 using acetone and removed the transparency, together with the generated SU-8 microboat, from the silicon wafer. Two masks were used in the fabrication for patterning the two SU-8 layers, respectively. In the final step, the SU-8 microboat was released from the substrate.

A representative microboat generated and its dimensions are given in Figs. 2.3d-e. The top layer was 140μm thick. The reservoir and nozzle had dimensions of 2.7mm x 2.7mm x 140μm and 2.4mm x 1.4mm x 140μm, respectively. The bottom layer was 270μm thick. The mass of the boat was 19.5mg. The total volume of the reservoir and nozzle was 1.49μl.

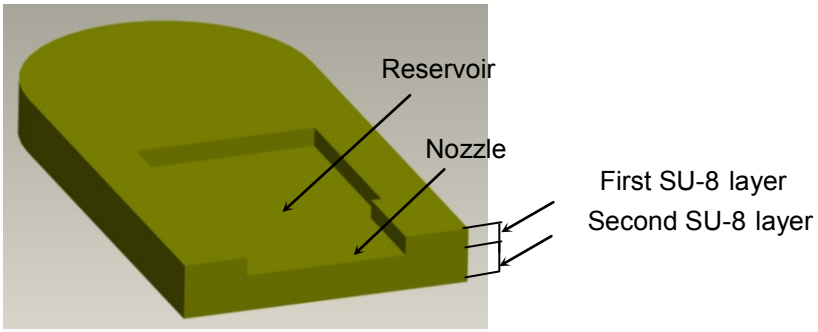

Figure 2.2: Schematic of a microboat used in this work [9].

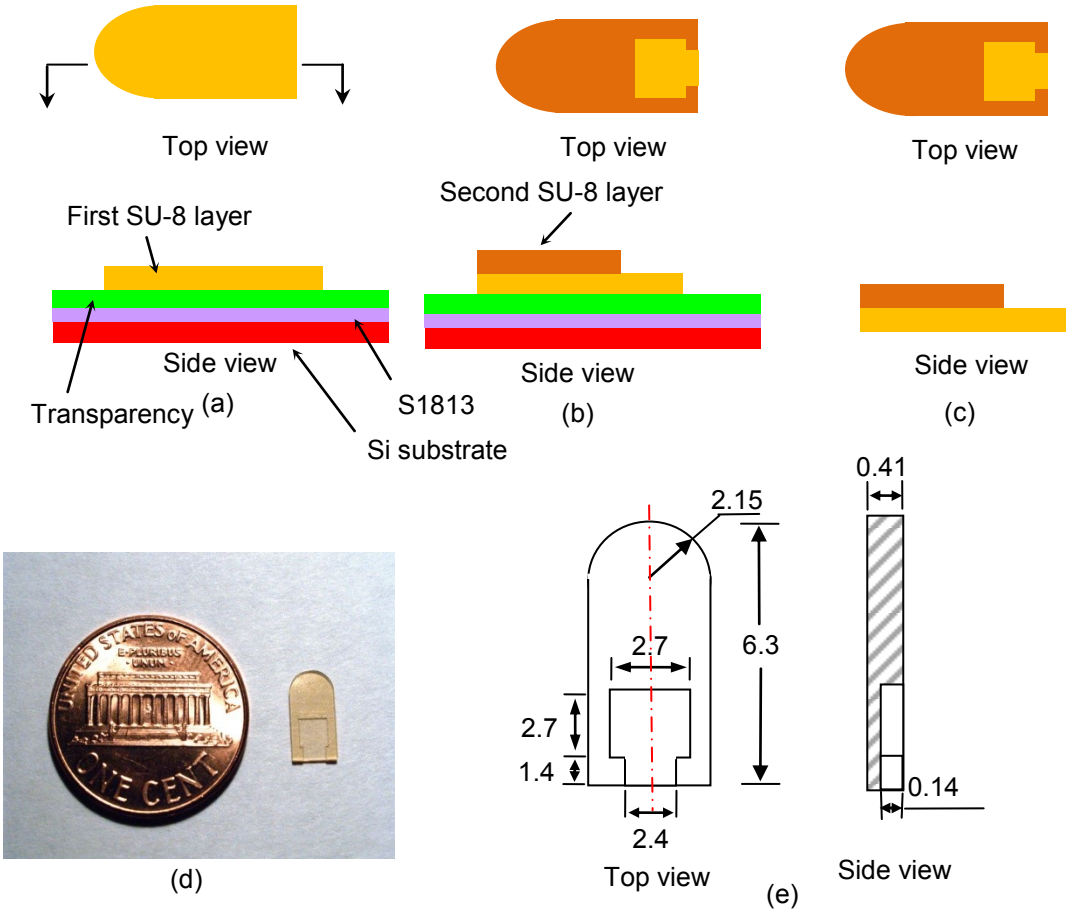

Figure 2.3: Three-step fabrication procedure: (a) place a transparency on an S1813-coated 4-inch silicon wafer, and pattern the first SU-8 layer on the transparency using the standard ultra-violet lithography approach, (b) pattern the second SU-8 layer, and (c) dissolve S1813 using acetone and remove the transparency, together with the generated SU-8 microboat from the silicon wafer. (d) A representative microboat generated, and (e) its dimensions (unit: mm).

2.4 Squat And Trim Phenomena In The Motions Of SU-8 Boats

The squat and trim phenomena are often observed when a macroboat travels in shallow water [50-56]. The horizontal speed around the hull is higher than that of the macroboat due to the restriction of the shallow water. According to Bernoulli's equation, the pressure underneath the hull becomes lower, and thus the macroboat sinks toward the bottom of water. In case the cross section of the bow is smaller than that of the stern, the pressure underneath the stern decreases more than that below the bow. This pressure difference makes the macroboat rotate in the vertical plane.

In recent tests conducted in a 1.2-cm-wide glass channel of 2.5-mm-deep water, we have found dramatic squat and trim phenomena in the motions of SU-8 boats. A representative motion is shown in Figs. 2.4a–c. It included two basic stages. The dramatic squat and trim phenomena appeared at the first stage and disappeared at the second stage. At the beginning of the first stage, the mid-boat gradually sank toward the bottom of the channel. In the meanwhile, the stern of the boat lowered down, while the bow of the boat rose up. The water depths right behind and in front of a boat were decreased and increased, respectively, to the same vertical levels as those of the stern and bow. However, the water depths far away from the stern and bow of the boat still remained the original level. That is, these depths were higher and lower than their counterparts around the boat, respectively. A hollow spot was seen behind the stern. The stern had the maximum sinkage of 2.0 mm and the bow was 0.5 mm above the original water level (Fig. 2.4a). At the end of the first stage, the stern and bow of the boat began to rise up and lower down, respectively (Fig. 2.4b). At the beginning of the second stage, the boat rose up to just below the water level and remained horizontal. In the meanwhile, the water far behind the boat moved forward. Once it reached the boat, the hollow spot behind the boat was completely filled, and this water pushed the boat forward (Fig. 2.4c). The boat continued to move forward until the water resistance made it finally stop. No visible squat and trim effects were observed during the second stage.

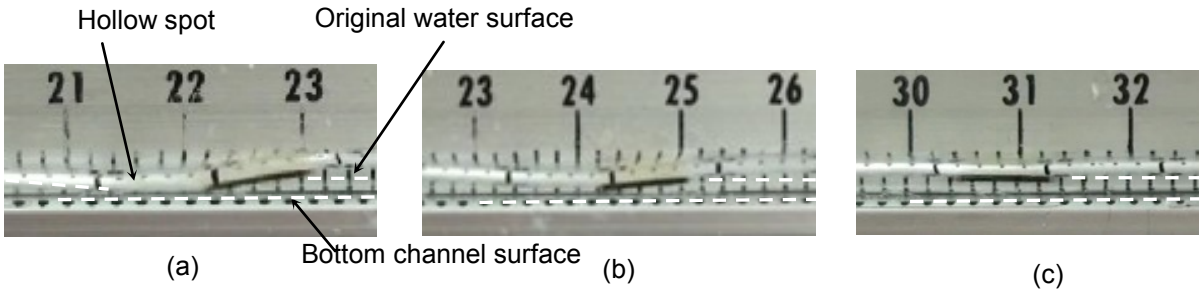

Figure 2.4: (a) the microboat had the maximum stern sinkage of 2.0 mm and the bow was 0.5 mm above the original water level (speed was 90 mm/s at t=0.93 s), (b) the stern and bow were rising up and lowering down, respectively, and their sinkages were 1.5 mm and 0 (speed was 60 mm/s at t=1.27 s), and (c) the microboat was moving forward and the sinkages of the stern and bow were both 0 (speed was 30 mm/s at t=3.00 s). The measurement error of the sinkages was ±0.25 mm.

2.5 Two Types Of Tests

Two types of tests were further performed to examine the dramatic squat and trim phenomena of the SU-8 boats. In the first type of tests, the boat only moved along the vertical direction, while in the second type of tests, it could move along both vertical and horizontal directions. All the tests were conducted in a 7-mm-wide glass channel, and 90% of the boat reservoir was filled with IPA in each test. To enhance squat and trim phenomena, as well as to examine these phenomena over a wider range of horizontal speeds, the channel used in these two types of tests was much narrower than the one used in the previous tests, and more fuel was loaded in the reservoir. Rulers were placed beside the channel to determine both vertical and horizontal positions of this boat. The motions were recorded using a camcorder (model: SONY HDR-XR 500 with 30 frames per second). The videos were then played in software Adobe Premier Element to determine the positions and sinkages at different time instants. In the first type of tests, a boat was placed inside the glass channel, and water depths were changed from 0.5 mm to 10 cm. A nylon rope was put in front of the bow to stop the horizontal movements of the boat. Independent of the water depth, the at-rest boat was submerged in water with its top surface just below the water level in the middle of the channel. After IPA was loaded into the boat reservoir using a needle, an interesting phenomenon was observed. Once

the IPA exited the reservoir and had contact with water, water rushed away from the reservoir, creating a hollow spot behind the stern. As indicated in Thomson in year of 1855 [41], this was due to the difference between the surface tensions of water and IPA, which made water flow away from IPA. In the meantime, the boat was titled along the sidewall of the hollow spot. The stern was located at the bottom of the hollow spot, and its sinkage equaled the depth of this spot (Fig. 2.5a). However, the bow was just a little below the original water surface. Since the horizontal speed of the boat was almost zero, squat and trim phenomena were not induced by the horizontal movement of this boat. Instead, they were caused by Marangoni effect, which created a hollow spot behind the stern and consequently caused the sinkage and rotation of the boat in the vertical plane.

The largest hollow spot generated behind the stern was related to the water depth in the channel. According to our tests, when water was 2.0 mm deep or below, the largest hollow spot generated was as deep as the original water depth in the channel, and no water was left underneath this hollow spot. If water was more than 2.0 mm deep, then the largest hollow spot was not as deep as that in the shallow water. Also, this hollow spot was more quickly filled by surrounding water. As the original water depth was 2.5 mm and above, the largest hollow spots remained to be 1 mm deep. The maximum stern sinkage was also related to the water depth in the same manner (Fig. 2.5b). When the original water depth ranged from 0 to 0.5 mm, the maximum bow sinkage was the same as this depth, while remained to be 0.5 mm after the original water depth was 0.5 mm or above. These results indicate that the squat and trim phenomena were more dramatic in shallow water than in deep water. The bottom of a hollow spot was covered by a thin IPA film. Water would not flow back to fill the hollow spot until the IPA at the bottom completely evaporated or diffused into water. During the filling process, the boat moved up due to the lift of water from underneath. After oscillating several times along the vertical direction, the boat recovered its original orientation and became horizontal. In addition, a hollow spot always existed behind the stern until no more IPA exited the boat reservoir.

Based on the experimental results, we found the existing of hollow spot is an important reason of squat effect of a microboat. Fluid flow is driven by the gradient of surface tension during the occurrence of the hollow spot. As shown in Fig. 2.5c, the horizontal coordinate toward the thinner region is assumed to be positive $-x$, that is the direction of $+x$. After IPA is applied to the region of water around center line, the concentration of IPA in that region is highest. A concentration gradient appears on the liquid surface. A mass transfer occurs due to the surface tension gradient induced by the concentration gradient. The liquid level in the center dropped. At the same time, due to the viscosity, the liquid beneath the surface move with the liquid on the liquid surface. A low pressure region is generated at bottom of hollow spot. Liquid near the bottom of container moves back to the center line from all directions. Vertex patterns are observed. Along with the mass transfer, the concentration of IPA around the center line will drop. The hollow spot will recover to the flat liquid surface. Similar phenomena happen when IPA is released from the reservoir of the microboat. The hollow spot appear right at the exit of the nozzle, Due to the lower of liquid level, the stern of the boat has a motion of squatting.

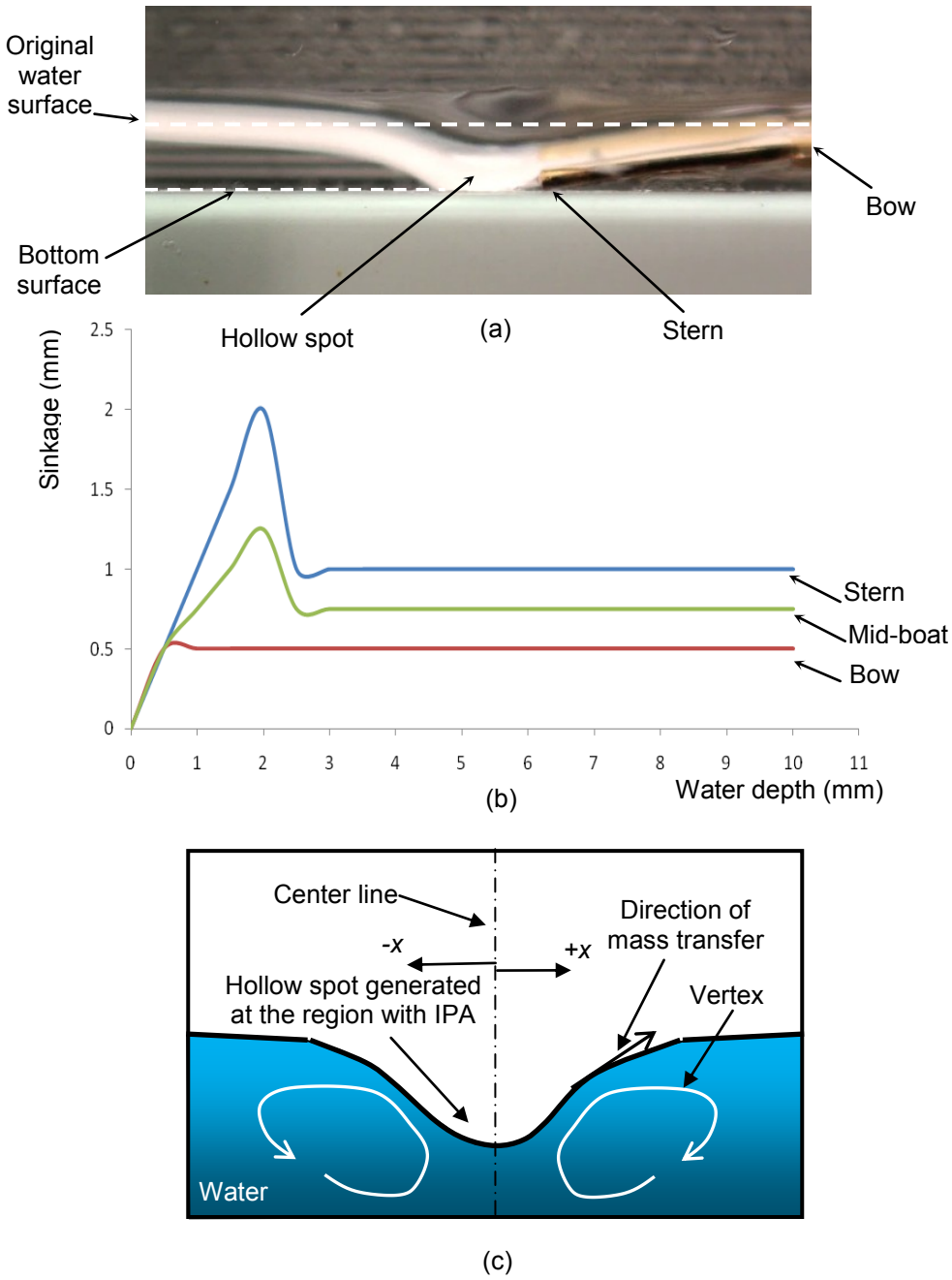

Figure 2.5: (a) Recorded scene at the time instant when the microboat had the maximum stern sinkage in the first type of tests; water was 2 mm deep, and the maximum sinkages of the bow and stern were 0.5 mm and 2 mm, respectively, and (b) experimentally determined relationships between the maximum (stern and bow) sinkages and the water depths in the first type of tests. The mid-boat shrinkage equaled the average value of the stern and bow sinkages. The measurement error in the sinkages was ±0.25 mm. The increment of the water depth was 0.5 mm, and experimental data points were not marked to see the corresponding curves clearly. (c) Flow induced by the surface tension gradient.

Based on the understanding gained from the first type of tests, we conducted the second type of tests, in which water depths in the channel were, respectively, 10 cm and 2 mm, to consider the deep- and shallow-water motions of the boat. Similar to what was observed from Figs. 2.4a–2.4c, the motions in these tests each included two basic stages. The corresponding speed–displacement and sinkage–displacement curves are given in Fig. 2.6. The motions in the deep- and shallow-water tests differed in both speeds and sinkages. At the first stage, the speed in the shallow water dropped from the highest value of 330 mm/s to the lowest of l30 mm/s, while the speed in the deep water dropped from the highest value of 300 mm/s to the lowest of 180 mm/s (Fig. 2.6a). The total travel distance in the deep water was 562 mm, much longer than that in the shallow water, which was 388 mm. These imply that the boat suffered much higher water resistance in the shallow water. The translational speeds of mm-scaled, disk-shaped polymer gels were reported to have an order of 10 mm/s [43, 44], while those of a mm-scaled, rectangular-shaped gel had an order of 100 mm/s [46]. Our mm-scaled SU-8 boat in the first stage of a motion in either shallow- or deep-water tests had the same order of speeds as the rectangular-shaped gel.

The following equation or its modified version has been previously used to predict the mid-boat sinkage induced by the horizontal movement of a macroboat in a narrow channel [50, 51, 53-56]:

$$F_h = \sqrt{\frac{2d(1-d-S)^2}{1-(1-d-S)^2}} \tag{2.4}$$

where $d = \frac{y_2}{y_1}$, $F_h = \frac{V}{\sqrt{gy_1}}$, and $S = \frac{\int_0^L A(x)dx}{by_1 L}$ represent depth, Froude number and mean blockage factor, respectively. V represents the horizontal speed of the boat, g gravitational acceleration, L the boat length, b the channel width, x the coordinate of a point on the middle line of the boat with the origin located at the stern, $A(x)$ the wetted cross-

sectional area of the boat, y_1 original water depth, and y_2 the mid-boat sinkage. Eq. (2.4) was derived based on Bernoulli's equation and equation of continuity. Experimentally measured horizontal speeds, which were the relative speeds between the boat and the at-rest water, were used to calculate F_h at the first stage of a motion. Since at the second stage of a motion the boat was pushed forward by water, the relative speed between the water and boat was 0. Therefore, F_h was considered to be 0 at this stage. After F_h was determined, the relationship of the mid-boat sinkage with the displacement was found using Eq. (2.4) (Fig. 2.6b). According to the theoretical prediction, at the first stage of the motion in the 2-mm-deep water (the travel distance was 284 mm), the mid-boat sinkage was negative (i.e., the mid-boat should rise above the original water surface) when the displacement was between 0 and 231 mm. The corresponding F_h varied between 1.06 and 2.33 in this range of the displacement. The mid-boat sinkages were also found to be negative in the experimental tests of macroboats when F_h was larger than 1 [51-53]. On the other hand, the measured mid-boat sinkage was 0 when the displacement was between 0 and 167 mm, and increased to 0.25 or 0.5 mm if the displacement was between 167 and 231 mm. When the displacement was between 231 and 284 mm, the theoretically predicted sinkages were between 0 and 0.33 mm (the corresponding F_h varied between 0.21 and 0.85). They were still lower than the measured sinkages, which ranged between 0.5 and 0.75 mm. In the case of the 10-cm-deep water, at the first stage of the motion (the travel distance was 194 mm), F_h was about 0 and the theoretically predicted mid-boat sinkages were also about 0. Nevertheless, at this stage, the measured mid-boat sinkages varied between 0.25 and 0.75 mm. At the second stage of a motion in either 2-mm- or 10-cm-deep water, we did not observe any visible squat and sinkage phenomena. The theoretically predicted sinkages were all 0. On the other hand, no hollow spots were observed behind the stern, implying there was no Marangoni effect involved at this stage. This further implies that no

IPA exited the boat reservoir at the second stage of the motion, and that the boat was driven by a water wave from behind as described in section 2.2.

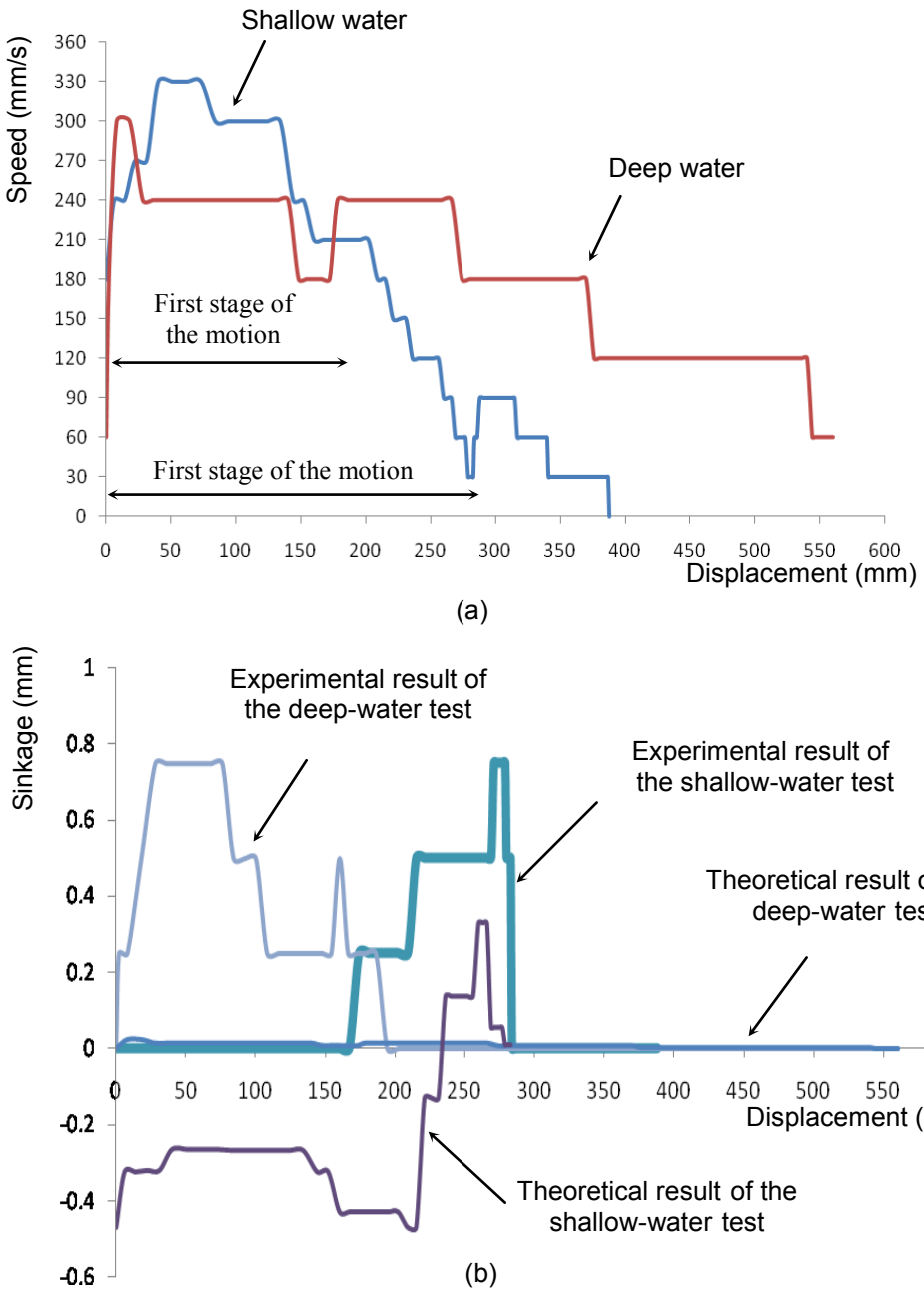

Figure 2.6: (a) Experimental speed-displacement curves in the second type of tests when water depths were 2 mm and 10 cm, respectively, and (b) the corresponding experimentally measured and theoretically predicted relationships of mid-boat sinkages with displacements. The measurement errors of the displacement and speed were ±0.25 mm and ±15 mm/s, respectively. The experimental data points were obtained every 0.033 s and not marked to see the corresponding curves clearly.

Based on the comparison between the theoretically predicted and experimentally measured mid-boat sinkages, the sinkages generated by the horizontal movements of the boat were much smaller than those observed in the experiments. Furthermore, the hollow spot induced by Marangoni effect made the boat have a large sinkage, as demonstrated in the first type of tests. Therefore, based on the two types of tests, we concluded that Marangoni effect could cause dramatic squat and trim phenomena in a miniaturized boat.

2.6 Summary And Conclusions

In conclusion, in this chapter, based on the results in two types of tests, we demonstrated that, in addition to propelling an mm-scaled SU-8 boat, Marangoni effect could also induce dramatic squat and trim phenomena in the motions of the boat. In addition, we found that the motion of the boat in a channel included two stages. In the first stage, it was propelled by surface tension gradients, accompanied with dramatic squat and trim movements. However, in the second stage, in which the propellant was used up, the boat was driven by a water wave, generated in the first stage. These results might also apply to surface tension-driven motions of other miniaturized objects.

CHAPTER 3

CONTROL OF THE RADIAL MOTION OF A SELF-PROPELLED MICROBOAT THROUGHT A SIDE RUDDER

In this chapter, using a combination of theoretical, numerical and experimental investigations, we explored another type of self-propelled microboat that could have radial motions. This type of microboat has side rudders. The side rudder induced an additional drag on one side, creating a moment to set the boat into an approximately circular motion. The radii of this motion could be controlled by varying the length of the side rudder. In this work, we designed, fabricated and tested eight microboats, whose rudders ranged from 0 to 10 mm in length. The speeds of these microboats were also in the order of 0.1 m/s. Depending on the rudder lengths, their moving paths had radii varying from infinity to 20 mm. According to moving trajectories, the radius of motion and the travel distance both decreased with the increase in the rudder length. We further built a theoretical model to predict the radius of the first loop of the moving path. By comparing experimental results with numerical solutions to the theoretical model, we found: (i) the numerical results had reasonably good agreement with the experimental results, and (ii) the mismatch between numerical and experimental results increased with an increase in the rudder length due to the simplified consideration in the simulation.

3.1 Principles Of Propulsion And Steering

When a liquid, which has a surface tension lower than water, exits the rear of the boat and covers the stern, the surface tension behind the boat is reduced, becoming lower than that at the bow. This difference in surface tensions propels the boat forward in a straight path (Fig. 3.1). As in our previous work [9-12], IPA (with 91% concentration) was also chosen as the

propellant in this work. There is a large difference between the surface tensions of IPA and water, which are, respectively, 22.8 mN/m and 72.8 mN/m at 20 °C.

The presence of a side rudder induces an additional water resistance, which creates a moment to rotate the microboat (Fig. 3.1). Consequently, the microboat is able to have a radial motion. The path of such a motion is related to the length of the side rudder.

3.2 Design And Fabrication

A schematic of a microboat is shown in Fig. 3.2a. The microboat is comprised of two SU-8 layers. The top layer included a reservoir and a nozzle. The bottom layer sealed the bottom of the reservoir and nozzle. An SU-8 side bar, which had the same thickness as the microboat, served as a rudder. Two masks were, respectively, used in the fabrication to define the structures in the bottom and top layers of the microboat.

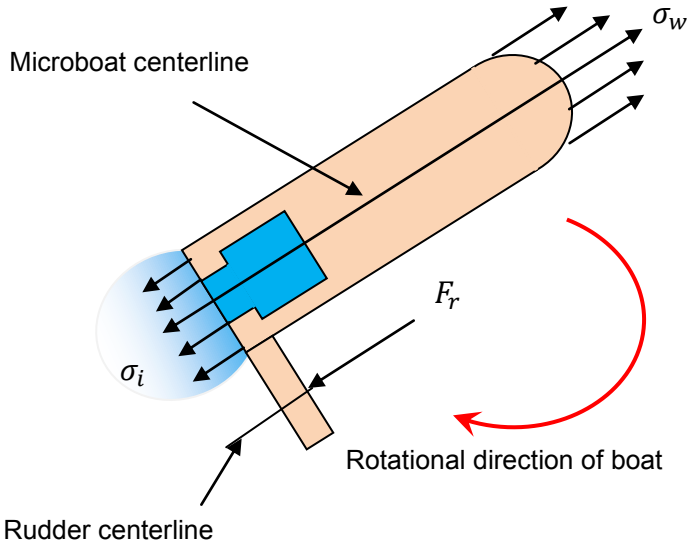

Figure 3.1: Free body diagram of a microboat. σ_w and σ_i are surface tensions before and after the boat, respectively, and F_r is water resistance on the side rudder. σ_w is larger than σ_i.

Ultra-violet (UV) lithography was adopted to fabricate such a microboat, which included four steps (Figure 3.2c): (i) place a transparency on an S1813-coated Si wafer, spin-coat the first SU-8 layer on the transparency, and expose it in a UV mask aligner through the first mask, (ii) spin-coat the second SU-8 layer on the first SU-8 film, and exposed it in the UV mask aligner through the second mask, (iii) develop the two SU-8 layers together using SU-8 developer, and (iv) dissolve S1813 using acetone and remove the transparency, together with the generated SU-8 microboat, from the Si wafer. Eight microboats were fabricated. They had the same hulls as the one shown in figure 3.2b, while their side rudders were 0, 2, 4, 6, 7, 8, 9 and 10 mm long, respectively. These rudders had the same width of 2 mm and the same thickness of 1 mm. A representative microboat generated, with a 2-mm-long rudder, is shown in figure 3.2d.

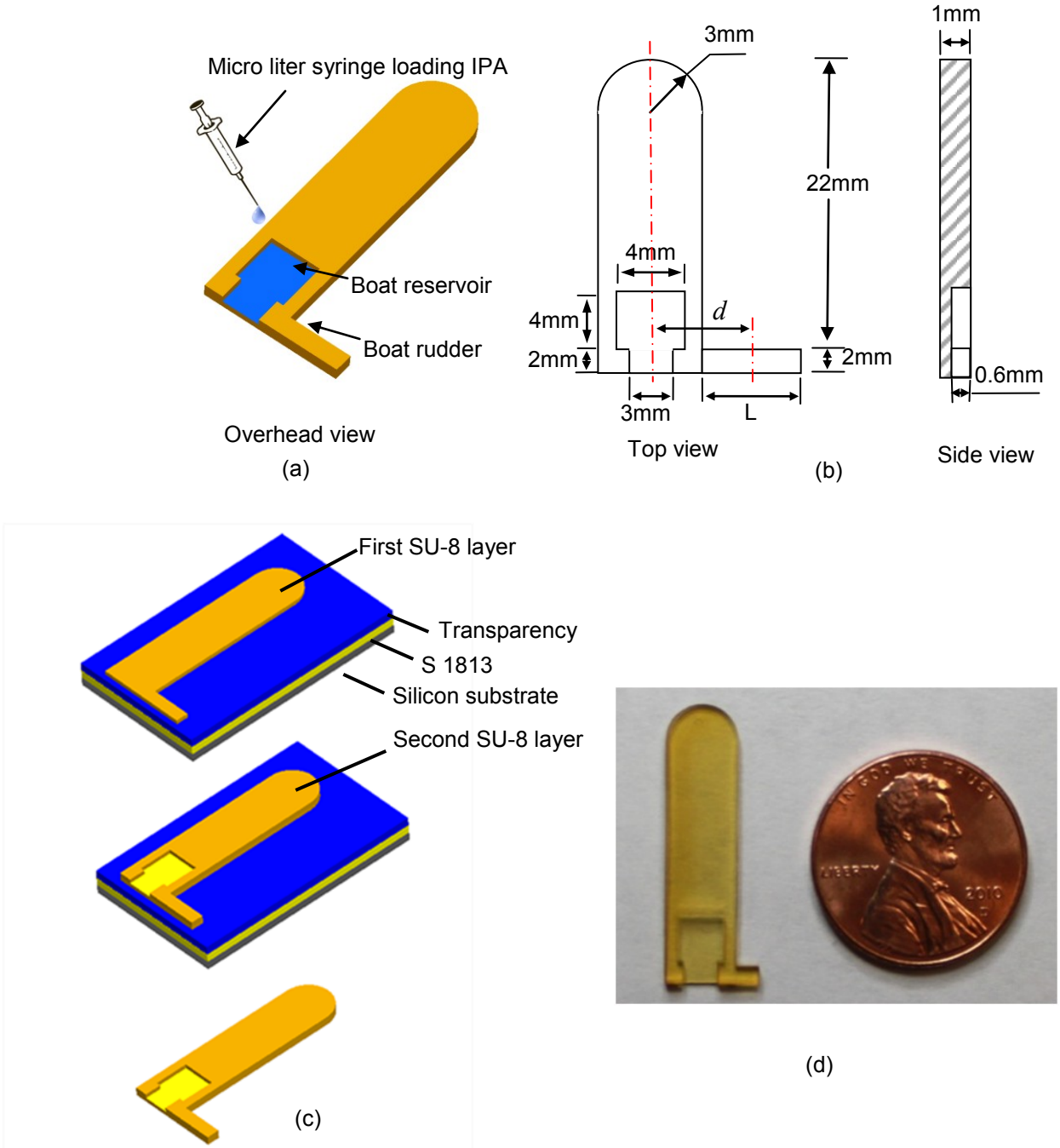

Figure 3.2: Schematics and fabrication process of a SU-8 microboat with a side rudder: (a) 3-D view of the SU-8 boat. A syringe with precision of 0.05 μl was use to load IPA into the reservoir in the experiments. (b) A representative microboat generated. (c) Procedure to fabricate a microboat.

3.3 Experimental Results And Discussions

In our previous work [9-10], we tested in straight and circular channels the microboats that did not have side rudders. In this work, we considered the motions of this type of microboats in an open water area. We also tested the microboats which had side rudders, and determined a relationship between the length of the rudder and the radius of the approximately circular motion. The radius was obtained according to the recorded trajectory.

All the microboats were tested in a 32-cm-long, 23-cm-wide glass container, which was partially filled to a depth of 1 cm with distilled water. A paper marked with 1 cm x 1 cm square patterns was placed underneath the glass container for locating the microboat. The water was changed after each test. At the beginning of every test, 1.2 μl IPA was loaded in the reservoir of a microboat using a syringe. Subsequently, the microboat began to travel due to the difference between fore-to-aft surface tensions. The microboat finally stopped when the IPA was exhausted. The motion was recorded by an HD digital camera (SONY HDR-XR500 with a frame rate of 30 fps). The video recording was then analyzed using Matlab R2010a. Each motion lasted 10--20 s, and the position of the microboat was tracked every 0.1 s. Accordingly, about 100--200 locations were used to analyze each motion.

3.3.1 Tests on Microboats without Side Rudders

Figure 3.3 shows two representative test results of a microboat without a rudder. After the IPA was loaded into the reservoir, the microboat accelerated during the first second. After that, its speed gradually decreased due to the increase in water resistance. The average speed during the motion was of the order of 0.1 m/s. The size of the glass container limited the largest travel distance. The microboat would collide with the wall of the glass container and turn to move along another direction. The microboat finally stopped after the IPA was exhausted. Through the two representative trajectories shown in Figure 3.3, we observed that the microboat was capable of moving along a relatively straight path before collision, while

sometimes it might turn slightly in its motion.

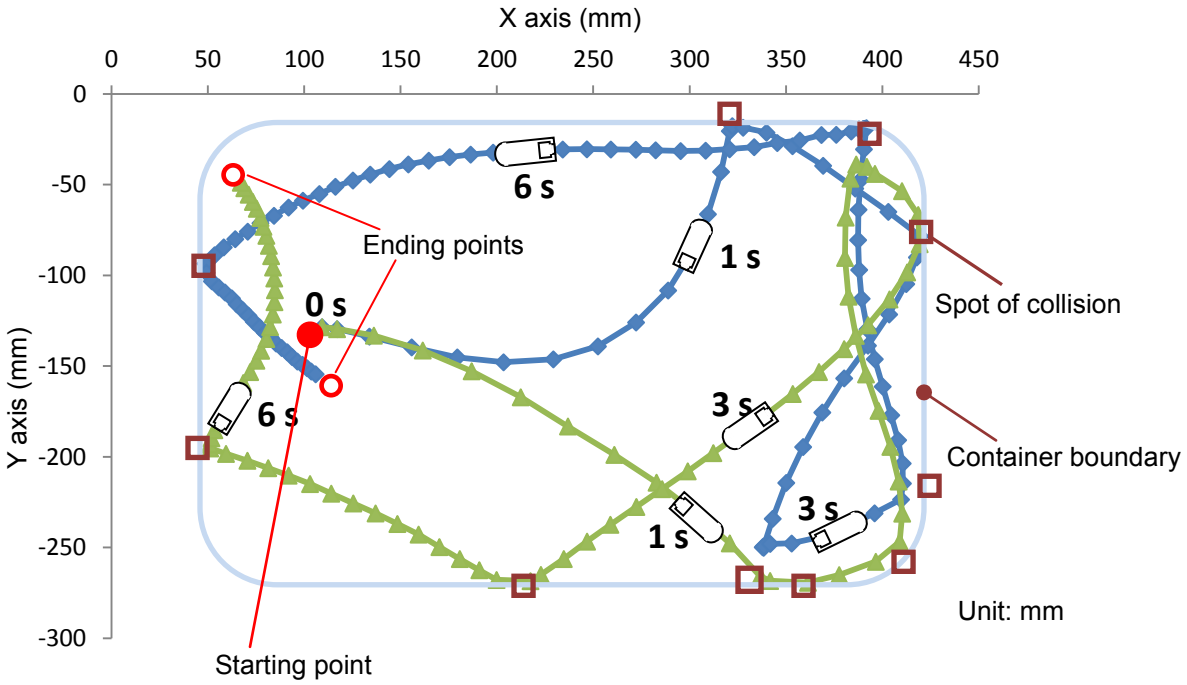

Figure 3.3: Two trajectories of the microboat without a side rudder recorded in the two tests, respectively (denoted by two different colors). The data points were obtained every 0.1 s.

To better understand why the microboat made a slight turn despite not having a rudder, we investigated the IPA flow in the reservoir using a stationary test (Fig. 3.4). The microboat was fixed on the water surface. The water level was adjusted to ensure that the microboat had the same draft as that in the previous tests. After 1.2 µl IPA was dropped into the reservoir, it first flowed to the closest wall of the reservoir and then split into two (left and right) branches (Fig. 3.4a). After that, both branches flowed towards the stern along the bottom corner of the reservoir. As shown in figure 3.4a, at 0.3 s, the right branch began to exit the nozzle, while the left one had not started exiting yet. At this moment, it is reasonable to consider that the driving force was acting on the spot where the right branch exited. This driving force did not pass through the gravity center of the microboat; consequently, a moment was generated that turned the boat in the counter-clockwise direction (Fig. 3.4e). After contacting with water, IPA flowed out faster. At 1.7 s, both branches flowed out of the nozzle and contacted with water. They also

formed similar flow profiles, which means that their flow rates were relatively the same (Fig 3.4b). At this point, the driving force passed through the center of boat and no moment was generated. At 4.7 s, the two branches were again different in their flow profiles. All 1.2 μl IPA was exhausted in 11 s. It could be concluded that the self turning was partially induced due to asymmetric flow profiles of the two IPA branches. Naturally, the asymmetry of the microboat in its geometry with respect to the centerline, caused by fabrication faults, would also induce the radial motion. If this was the case, then the turning direction of such motions should be consistent. As observed from the initial stages of the two trajectories (Fig. 3.3), the turning directions were not the same. This indicated that in our case the asymmetric flow profiles of the IPA branches might be the dominant factor affecting the turning direction.

In addition, as what we observed in [8], water did not flow back into the reservoir during the process that the IPA was leaving the reservoir. Otherwise, the IPA in the reservoir would drive the water due to the difference in their surface tensions. Therefore, the IPA that just exited the reservoir nozzle still remained its concentration of 91%.

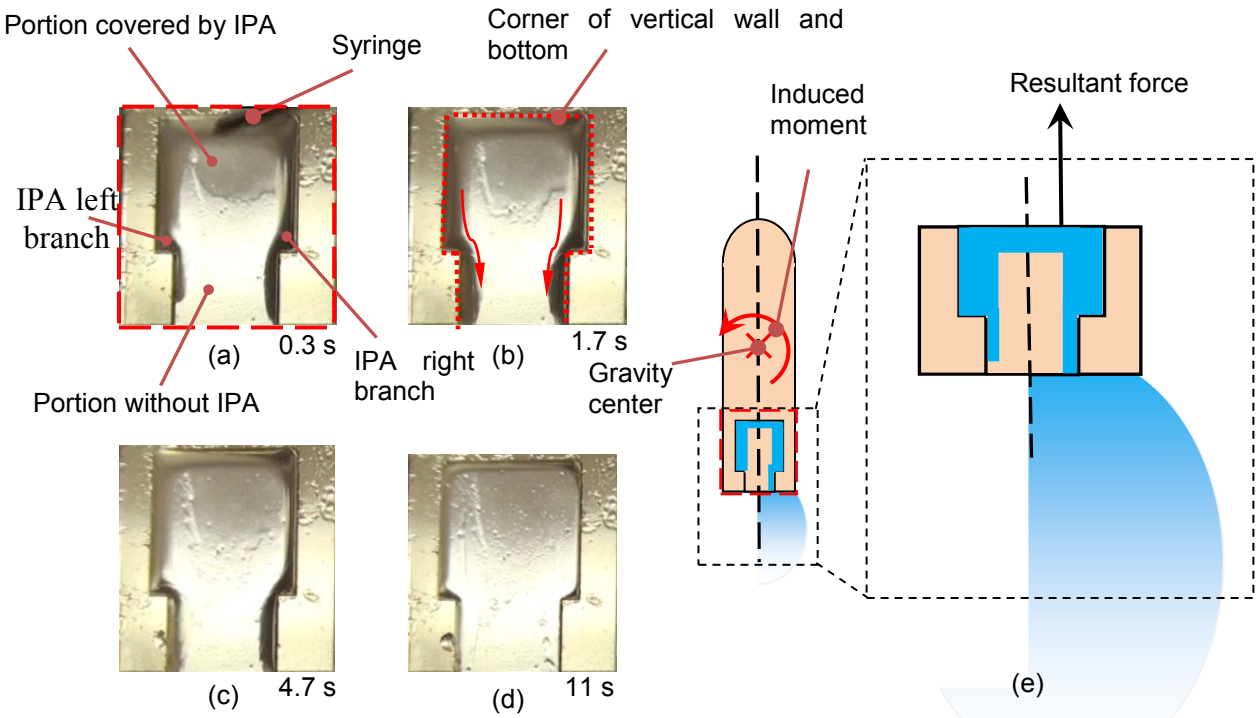

Figure 3.4: The process that IPA flows out of the reservoir (a) at 0.3 s, (b) at 1.7s, (c) at 4.7 s, and (d) at 11 s. (b) Schematic of induced moment that rotates the microboat.

3.3.2 Tests on Microboats with Side Rudders

Fig. 3.5 showed representative test results of microboats with 2, 4, and 8-mm-long rudders, respectively. Fig. 3.5a gives sequential snapshots of the first loop in the approximately circular motion of the microboat with the 2-mm long rudder. After the acceleration during the first second of the motion, the speed of boat began to decrease from the maximum speed, which was around 0.14 m/s. The corresponding trajectory was close to a circle. Figs. 3.5b-d are complete trajectories of microboats with 2, 4 and 8-mm-long rudders, respectively. After about 1 s of acceleration, the microboat with the 2-mm-long rudder has the highest speed, while the microboat with an 8-mm-long rudder has the lowest speed among the three boats (Fig. 5e). Subsequently, the microboat with the 2-mm-long rudder keeps traveling with lowest

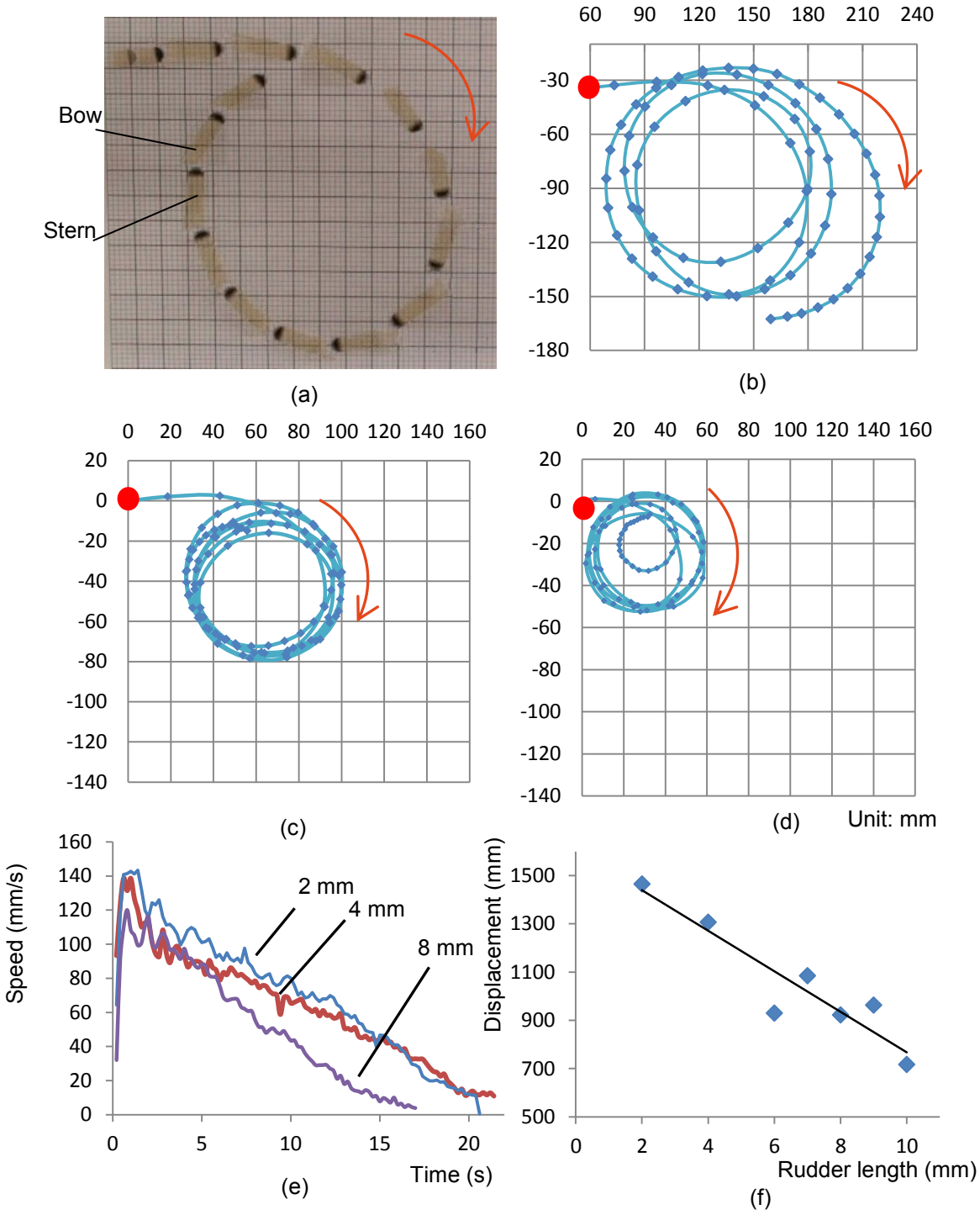

Figure 3.5: Experimental results: (a) sequential snapshots of a radial motion for the microboat with the 2-mm-long rudder, moving trajectories of the microboats with (b) 2-, (c) 4-, (d) 8-mm-long rudders, (e) their speed-time curves and (f) relationship between total displacement and rudder length.

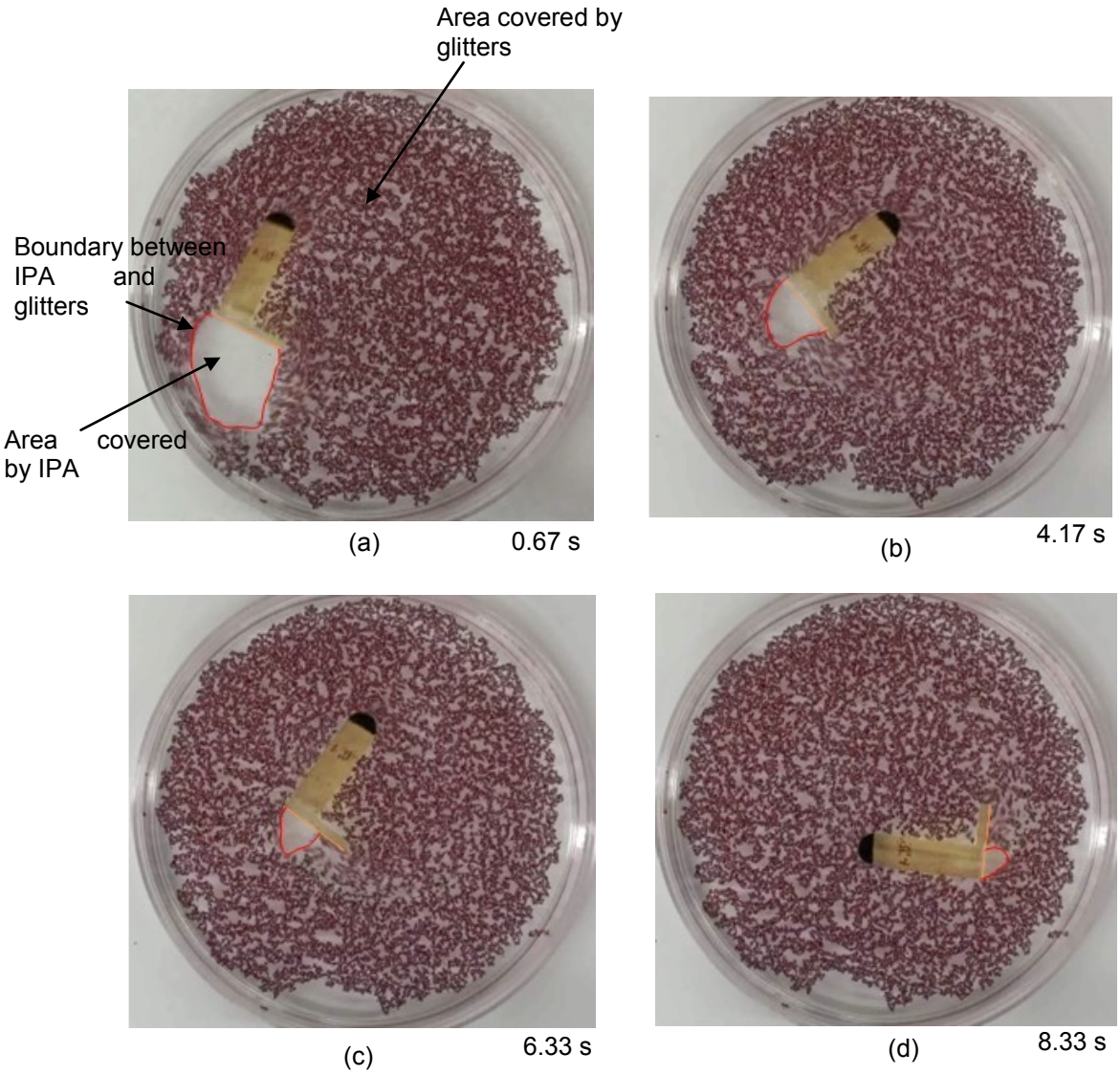

Figure 3.6: Sequential snapshots of IPA covered area when the microboat with the 6-mm-long rudder was having a radial motion: (a) at 0.67 s IPA covered the whole rear part of microboat, (b) at 4.17 s IPA covered the stern and 4 mm of the rear part of the rudder, (c) at 6.33 s IPA covered the stern and 2 mm of the rear part of the rudder, and (d) at 8.33 s IPA covered only the stern.

deceleration until it stops completely at 22 s. In comparison, the microboat with an 8-mm-long rudder travels with highest deceleration and stops at 17 s. The average radius of the path and the total travel distance both decreased with the increase in the rudder length (Figs. 3.5f and 3.7b).

The propulsion caused by the surface tension difference could also be applied to drive glitter powder. Thus, we used the glitter powder to visualize the propulsion of all eight microboats. We observed that glitter powder around the stern was pushed away, and that an area without this powder (called empty area thereafter) was formed behind the stern. During the first 11 s of the motion, the IPA covered the whole stern of a microboat. However, the coverage on the rear part of the side rudder varied with time. Take the microboat with the 6-mm-long rudder as an example (Fig. 3.7). At 0.67 s, IPA covered the rear part of the rudder. At 4.17 and 6.33 s, the covered rudder lengths were 4 and 2 mm, respectively. After 8.33 s, there was no coverage of the IPA on the side rudder. At the boundary of the empty area, we observed that the glitter powder was not moving. This implied that the concentration of the IPA at the interface of the empty area and the glitter powder was 0. On the other hand, the concentration of IPA at the reservoir nozzle was 91%. Thus, there was a concentration gradient in the empty area. The concentration of the IPA decreased with the increase in the distance from the reservoir nozzle. Since the empty area was small (its largest dimension was 12 mm in the case of microboat with the 6-mm-long rudder, for example), the concentration actually decreased sharply over the distance. This also implied that the corresponding surface tension decreased dramatically with the distance [57]. In the next section, for simplicity, we assumed that only the stern was covered by the IPA (with 91% concentration). Based on this assumption, the propulsive force was considered to be constant, and the problem of considering the motions of the microboats was simplified accordingly.

3.3.3 Theoretical and Numerical Modeling

To predict the radius of the first loop based on the rudder length, we built a theoretical model to consider the motions of the microboats. According to the free-body diagram shown in Fig. 3.1, the radial motion of a microboat may be described by the following three equations of motion:

$$I\frac{dw(t)}{dt} = M_{dv} - M_{dg}, \tag{3.1}$$

$$m\frac{dv_x(t)}{dt} = F_{dv}\cos\theta(t) - F_{xdg}, \tag{3.2}$$

$$m\frac{dv_y(t)}{dt} = F_{dv}\sin\theta(t) - F_{ydg}, \tag{3.3}$$

where I denotes the moment of inertia, m the mass of the microboat with rudder, w the angular velocity, v_x and v_y the translational speeds in x and y directions respectively, and θ the angle of rotation at that moment. In Eq. (3.1), M_{dv} and F_{dv} are the driving torque and force (Fig. 3.6), which are determined, respectively, by

$$M_{dv} = F_{rdg}\times d, \qquad F_{dv} = (\sigma_w - \sigma_i)W, \tag{3.4}$$

where the F_{rdg} is the drag force acting on side rudder, d is the distance between the middle lines of the microboat and the rudder (Fig. 3.1), σ_w and σ_i are the surface tensions of water and IPA, respectively, W is the width of the microboat. In the Eqs. (3.1)-(3.3), M_{dg} is the moment induced by the drag, while F_{xdg} and F_{ydg} are the components of total drag in x and y directions, respectively (Fig. 3.6). These three items, as well as F_{rdg}, can be determined by the equations,

$$M_{dg} = \int_{-\frac{L}{2}}^{\frac{L}{2}} \eta\, w(t) r^2\, dr,\ F_{xdg} = \eta\, v_x(t) W_c,\ F_{ydg} = \eta\, v_y(t) W_c,\ F_{rdg} = \eta\, v(t) W_r, \tag{3.5}$$

where L is the length of the microboat, W_c is the characteristic length of boat and equals one half of the summation of boat length and width, W_r is the length of the side rudder and η is the a coefficient. . According to [58], drag coefficient C_d and Reynolds number R_e for a flow around a flat plate are defined as follows:

$$C_d = \frac{2F_{dg}}{\rho v^2 W D},\ R_e = \frac{\rho v D}{\mu}, \tag{3.6}$$

where ρ is water density, *D* and *W*, respectively, represent the dimensions of the flat plate along and perpendicular to the flow direction, and μ denotes the kinematic viscosity of fluid. Eq. $(3.6)_1$ holds for a flat plate in a laminar flow. The flow in our case is laminar since the Reynolds number is around 1000. Furthermore, since the ratio between the width and thickness of a boat was 6, the boat could be considered as a flat plate. Therefore, Eq. $(3.6)_1$ is applicable to this work. In addition, we propose

$$C_d = \frac{\alpha}{R_e}, \tag{3.7}$$

where α is an unknown coefficient. After plugging Eq. (3.6) into Eq. (3.7), we have

$$F_{dg} = 0.5\alpha\mu v W. \tag{3.8}$$

For simplicity, let

$$\eta = 0.5\alpha\mu, \tag{3.9}$$

which leads to

$$F_{dg} = \eta v W. \tag{3.10}$$

Likewise, we obtain Eqs. $(3.5)_2$-$(3.5)_4$ followed by the determination of Eq. $(3.5)_1$.

After inserting Eqs. (3.4) and (3.5) into Eqs. (3.1)-(3.3), we have

$$I\frac{d\omega(t)}{dt}=(\sigma_w-\sigma_i)W_b\times d-\int_{-\frac{L}{2}}^{\frac{L}{2}}\eta v_x(t)\omega(t)r^2dr\,, \tag{3.11}$$

$$m\frac{dv_x(t)}{dt}=(\sigma_w-\sigma_i)W_b\cos\theta(t)-\eta v_x(t)W_c, \tag{3.12}$$

$$m\frac{dv_y(t)}{dt}=(\sigma_w-\sigma_i)W_b\cos\theta(t)-\eta v_y(t)W_c. \tag{3.13}$$

η that is involved in Eqs. (3.11)-(3.13) is found as follows. According to the in-situ observation, the IPA was completely exhausted within around 11 s after it had started exiting the reservoir (Fig. 3.4). Thus, after the first 12 s of a motion, there should be no driving force and consequently the microboat should suffer only drag forces. The corresponding equation of motion is

$$m\frac{dv(t)}{dt}=-\eta\,v\left(t\right)W_c\,. \tag{3.14}$$

Subsequently, according to this equation, η could be calculated based on experimentally measured values of $v\left(t\right)$ (Fig. 3.5e). For example, in the case of a 2-mm-long rudder boat, we have *m*=1.67 g and W_c =16.5 mm. By Eq. (3.14), the corresponding η was calculated to be 2.0 $^{\mathrm{g}}\!/_{\mathrm{mm\cdot s}}$.

After the determination of η, $\omega(t)$, $v_x(t)$ and $v_y(t)$ were calculated by solving Eqs. (3.11)-(3.13) using Matlab. The initial position and speeds were all set to be zero. The driving force was considered to be constant before the complete consumption of the IPA. The first trajectory loops that were simulated are given in Fig. 3.8a. Numerically and experimentally determined relationships of the radius of motion with the length of rudder are given in Fig. 3.8b. It can be seen from Fig. 3.8b that, when the length of a rudder ranged between 3 mm and 7 mm, the

numerical results had a good match with those of experiments. However, with the increase in the rudder length, the simulated radius of motion became gradually smaller than the corresponding experimental value. In addition, there was a large error when the rudder was 2 mm long.

For the simulation, we simplified the model by assuming: (i) there was no IPA coverage on the back side of the side rudder, and (ii) 91% IPA covered the stern. Accordingly, the driving force was simplified as the multiplication of the boat width and the surface tension difference between water and 91% IPA. In reality, the IPA may cover part of or the entire side rudder, as observed from Figure 6. Accordingly, an additional force would be generated on the side rudder due to the difference in the surface tensions between the front and rear portions of this rudder. The opposite moment generated by this additional force would partially cancel the driving moment induced by the drag. Hence, the total moment that rotates a boat is reduced, and the radius of motion in reality should be larger than the one predicted by the simulation. Furthermore, the opposite moment should increase with the length of the side rudder, making the total moment that rotates the boat decrease with the rudder length. Accordingly, the difference between numerical and experimental results also increases with this rudder length. Given that the rudder was very short relative to the length of the boat (for example, 2 mm long), both the opposite and driving moments were small. As shown in Figure 4, an additional moment could also be induced by the asymmetric IPA flow inside the boat reservoir, which may be comparable to these two moments in this case. Consequently, a large error may be generated in the simulation result due to the neglect of the additional and opposite moments.

The IPA exited the reservoir via the two corners of the nozzle in the first 11 s (Fig. 3.4). The IPA was diluted by the surrounding water once it left the nozzle. These two points imply that the average IPA concentration behind the stern may be below 91% after about 0.3 s. Thus, the second assumption (i.e., 91% IPA covered the stern) made in our simulation may only hold for the first loop of the motion, and would be violated afterwards. Accordingly, we only simulated

the first loop on the motion in this work.

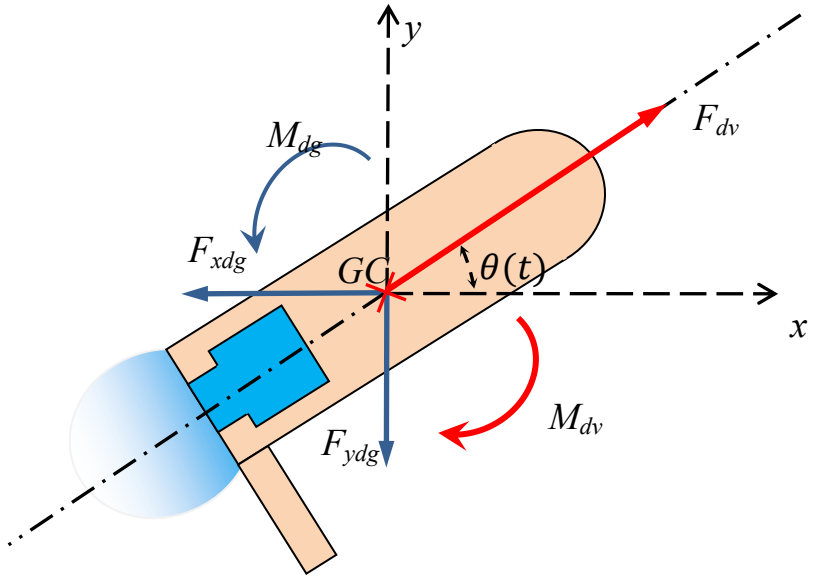

Figure 3.7: A complete free-body diagram of a microboat. M_{dv} and F_{dv} are the driving torque and force, respectively, M_{dg} is the moment induced by the drag, while F_{xdg} and F_{ydg} are the components of total drag in x and y directions, respectively.

.

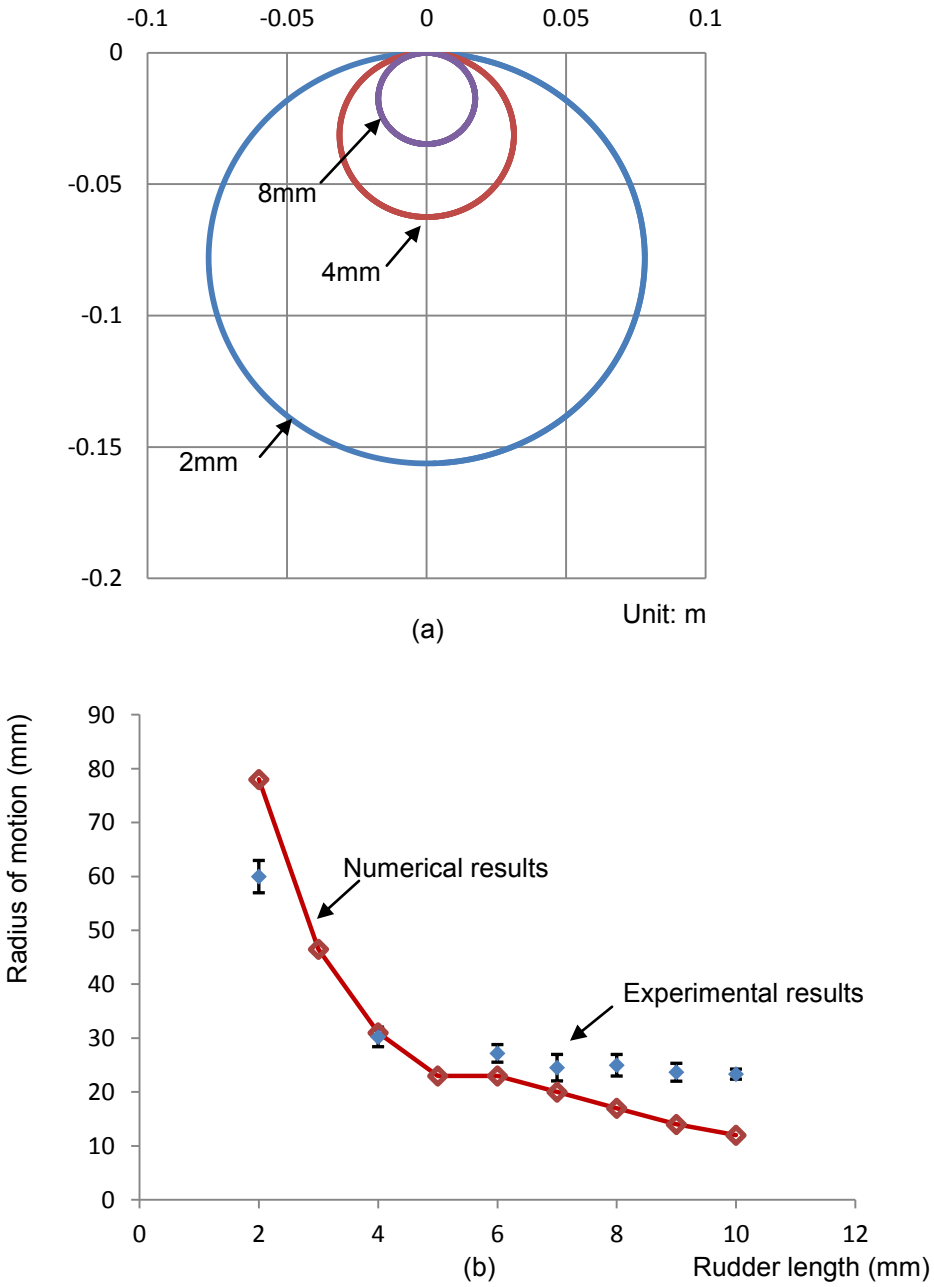

Figure 3.8: (a) Representatively simulated trajectories of 2-, 4-, and 8-mm-long rudders microboats. (b) Comparison between the numerical and experimental results: radius of motion vs. rudder length (the error bars were determined by 8 measurements).

3.7 Summary And Conclusions

In this chapter, we developed a type of microboat that had side rudders. Eight microboats were tested. The lengths of their rudders ranged from 0 to 10 mm. Experimental results demonstrate: (i) through a side rudder, it is feasible to control the radial motion of a microboat; (ii) the radius of a radial motion decreases as the length of a rudder increases; and (iii) the total travel distance and the maximum speed both decrease as the length of a rudder increases. A theoretical model was also developed to consider the motions of these microboats. The corresponding numerical results had a reasonably good agreement with the experimental results, and the mismatch between numerical and experimental results increased with the length of the side rudder due to the simplified consideration in the simulation.

CHAPTER 4

PROPULSION OF A MICRO SUBMARINE USING A THERMALLY OSCILLATORY APPROACH

Microboats can have a longitudinal and radial motion on water surface, but its driving force is from the air water interface. Once it is in the water, its driving mechanism will not be applied. In this chapter, we demonstrate a novel driving mechanism which is capable to propel a micro vehicle under water. This vehicle has a comparable size with microboat. Motivated by the driving mechanism of a putt-putt toy boat, we explore the feasibility to propel a micro submarine using a thermally oscillatory approach. This driving mechanism only requires a simple design and does not involve any complicated propulsive systems. We investigate the design, fabrication, actuation and horizontal motions of the corresponding micro submarines. Based on the understanding gained through preliminary tests on two manually fabricated putt-putt boats, we designed and fabricated the prototype of a micro submarine. Similar to a putt-putt boat, the prototype also uses a thermally oscillatory process for propulsion. In a cyclic period of this process, due to the expansion and shrinkage of a vapor bubble inside the reservoir of the submarine, liquid is first ejected outside and then sucked into the reservoir. Due to the difference in liquid flow directions between ejection and suction stages, a thrust is produced to propel the submarine. At an applied voltage of 16 V and pulse frequency of 100 Hz, the submarine was found to have the highest speed of 1.8 mm/s and longest travel distance of 12.6 mm. The corresponding thrust was estimated to be 67.6 nN.

4.1 Introduction

Macro submarines are widely employed for military and civil uses, such as defense, exploration, tourism, oil and gas platform inspections and pipeline surveys. Likewise, micro

submarines can also be employed on demand, for example, to deliver chemical and biological solutions in microfluidic applications, or to carry sensors for detecting specific targets in liquids. However, little work has been done on micro submarines, although much research has been done on microsystems that are movable on solid or liquid surfaces, such as comb drives [76], micromotors [77], microflies [78], surface tension-driven gels [39], miniaturized boats [9-14] and flotillas [9,10]. Thus, in this work, we explore the possibility of developing micro submarines.

Two requirements should be met by a micro submarine: (i) it should be easily manufactured to reduce fabrication effort and cost; and (ii) similar to a macro submarine, it should be mobile under liquid. In the case of macro submarines, the motions are controlled by propellers and their control systems [79,80]. Due to small sizes of micro submarines, conventional submarine-manufacturing techniques are not suitable for producing them. Instead, ultra-violet (UV) lithography is suited at fabricating such small items. Nevertheless, it is costly and time-consuming to generate propellers and their control systems. Thus, the critical obstacle in developing micro submarines is to find an appropriate propulsive approach that eliminates the use of complicated systems.

Microdevices may be actuated by thermal [81, 82], electrostatic [76,83-86], and magnetostatic [77,87,88] and acoustic [89] forces, as well as by surface tensions [4-10]. Electrostatic, magnetostatic and acoustic approaches require the introduction of external electrical, magnetic and acoustic fields, respectively, to guide the movements of the microdevices. Accordingly, they limit the applications of the submarines, making them only applicable to the places set up with the electrical, magnetic or acoustic fields. We have recently developed surface tension-driven miniaturized boats and flotillas [9-14]. Since surface tensions only exist at liquid surfaces, surface tension-based approaches do not apply to submarines that may need to travel under liquid. It is also noticed that thermal approaches have been applied to actuate large-scale rockets and airplanes. In these approaches, a thrust is produced by burning fuel to generate a high-speed jet, which provides a force to make the vehicle move along the

opposite direction of the jet. However, since a micro submarine has a limited space to store fuel, the adoption of the thermal approaches would limit the travel distance of the micro submarine. Moreover, thermopneumatic [47], electrohydrodynamic [48] and electrowetting-on-dielectric [49] methods are also applied to actuate small objects in liquids. Nevetheless, it appears that the corresponding thrusts may not be large, since the total travel distances are 1.7 mm [47] or less [48, 49].

The propulsive approach that is adopted in this work is a thermally oscillatory method, which is motivated by a propulsive approach employed in a so-called putt-putt or pop toy boat [90, 91]. The adopted propulsive approach only requires a thermal ejector, which includes a resistive heater and a reservoir. Due to the ease of fabricating the thermal ejector using UV lithography, the development of a micro submarine becomes feasible. Based on this propulsive approach, we develop the prototype of a micro submarine, and also explore its horizontal motions.

This chapter is outlined as follows. Driving mechanism is introduced in sub-section 4.2. Preliminary tests on putt-putt boats are presented in sub-section 4.3. Design and fabrication of micro submarines are described in sub-section 4.4. Experimental results and discussions are given in sub-section 4.5. Finally, in sub-section 4.6, this work is summarized and concluded.

4.2 Driving Mechanism

4.2.1 Determination of Thrust during Outflow

Like jet moving forward by discharging a fast moving gas, the propulsion force on microsubmarine results from the moving water. When water was pushed out of the chamber, the reacting force propelled the microsubmarine forwards. This phenomenon can be explained by the classic Newton's law of motion. However, the movement of water in the chamber is alternating. The same reason, one may be confused about the reason why the microsubmarine would not drew back when water flow in the chamber. If so, it wouldn't move forward but oscillate in one place instead. Actually, the inflow of the same magnitude does not produce an

equal thrust as outflow. The imbalance make possible microsubmarine always moves in one direction.

Because of the viscosity, the water leaves microsubmarine as a jet. During the inflow, the water is not a jet but flow from all around into nozzle. In either case, the motion can be described by the basic equations:

$$m\frac{\partial^2 x}{\partial t^2}+D(v)=P-\frac{\partial^2 (mh)}{\partial t^2}, \tag{4.1}$$

where *m* is the mass of the microsubmarine and liquid at time t, x is the coordinate with exit of nozzle as origin, $D(v)$ is the drag force on the microsubmarine, $v=\frac{\partial x}{\partial t}$ is the speed of the microsubmarine, P is the driving force, h is the distance from the x coordinate origin to the center of mass. If we assume P is the resolution of all surface pressure and momentum stresses expressed as a vector. Thus,

$$P=i\iint\left\{\rho U\left(U\cdot n\right)+np\right\}dS, \tag{4.2}$$

Where i is the unit x coordinate vector, ρ is the density of water, p is the pressure on the surface, U is the water velocity at the surface, n is the unit normal vector at the surface and S is the surface include exit plane of the nozzle. To further simplify the equation, it is reasonable to consider the oscillatory motion as a “steady state” though in oscillatory manner. In this case Eq. (4.2) can be averaged over one cycle using the notation

$$\frac{1}{T}\int_0^T Gdt=\{[G]\}, \tag{4.3}$$

Leads to

$$\left\{\left[m\frac{\partial^2 x}{\partial t^2}+D\left(v\right)\right]\right\}=i\iint\left\{\rho\{\left[U\left(U\cdot n\right)\right]\}+n\{[p]\}\right\}dS-\frac{1}{T}\frac{\partial (mh)}{\partial t}]_0^T, \tag{4.4}$$

The last term in equation (4.4) equals zero, when $\frac{\partial(mh)}{\partial t}$ has the same value at the beginning or end of one cycle. During exhaust process, the jet leaves the nozzles in a direction normal to its exit plane. The pressure in the jet is equal to the static pressure of the surrounding liquid. Thus,

$$i\iint\left\{\rho\{\left[U_e\left(U_e\cdot n\right)\right]\}+n\{[p_e]\}\right\}dS\cong i\iint\rho\{\left[U_e\left(U_e\cdot n\right)\right]\}dS=\rho\{\left[U_e{}^2\right]\}a, \quad (4.5)$$

where a is the total cross-sectional area of the nozzles. Finally, it is obtained that

$$\{[P]\}=\rho\{\left[U_e{}^2\right]\}a, \quad (4.6)$$

where ρ is the density of IPA, U_e is the velocity of the flow, and a is the cross sectional area of two nozzles.

4.2.1 Determination of Thrust during Inflow

Different from exhaust process, during inflow, the liquid returns to the chamber from all directions. At the moment it entering the nozzles, the fluid velocity will not normal to the nozzle exit plane. The pressures will vary over the microsubmarine and exit plane surface. In order to estimate the magnitude of the thrust, we first consider the liquid as incompressible fluid, the governing equation is written as

$$\frac{\partial U}{\partial t}+(U\nabla)U=-\nabla(\Omega+p/\rho)+\mu(\nabla^2U)/\rho, \quad (4.7)$$

Where μ denotes the dynamic viscosity, and Ω the gravitational potential. After being integrated over the fluid volume outside the boat and averaged over one cycle, we rearrange the equation and obtain that

$$\rho\iiint\{[(U\nabla)U]\}dV+\iiint\{[\nabla p]\}dV=-\rho\iiint U\Big]_0^T dV-\rho\iiint\nabla\Omega dV+\mu\iiint\{[\nabla^2U]\}dV. \quad (4.8)$$

Note $U(T)-U(0)=0$, because U is the same at the beginning and end of one cycle. Applying Gauss' theorem, we obtain

$$\iint \{\rho\{[U(U\cdot n)]\}+n\cdot\{[p]\}\}dS=-\rho\iint n\cdot\Omega dS-\mu\iiint\{[\nabla(\nabla\cdot U)]\}dV$$
$$+\mu\iiint\{[\nabla\times(\nabla\times U)]\}dV. \tag{4.9}$$

Since the gravitational potential Ω generate no thrust in horizontal direction, the first term on the right vanishes. Also, the liquid is incompressible in our case, so the ∇U equals zero. Thirdly, since inflow is approximately irrotational, $\nabla\times U$ equals zero or very small. Thus

$$\iint\{[U_i\left(U_i\cdot n\right)\}]+n\{[p_i]\}dS\cong 0. \tag{4.10}$$

Also, the thrust, if there are any, during in flow is pointing to opposite direction of moving direction. Therefore, the thrust is considered only generated during the exhaust of liquid. The net thrust can be determined by Eq. (4.6).

4.3 Preliminary Tests

According to [90], the putt-putt boat is originated in an 1891 British patent for water pulse engines invented by Thomas Piot. Based on the description and schematic of such a boat [90, 91], we manually fabricated a large putt-putt boat (Fig. 4.1a). The propulsive system in this boat includes a candle, a shallow Al chamber, and two pipes that connect to the Al chamber and lead to the rear of the boat. In a water tank, this boat moved in an approximately periodic manner with the period of 0.18 s (Fig. 4.1b). In each period, the speed first increased to about 12cm/s and then decreased to 0. We also manually manufactured a small putt-putt boat with a transparent chamber and a transparent pipe for two purposes (Figs. 4.2a and 4.2b): (i) have a deep understanding of the propulsive mechanism described in [91] through in-situ observation of the thermal oscillatory process, and (ii) examine whether a resistive heater can replace a candle to generate a water jet (since a candle cannot be used in the micro submarine).

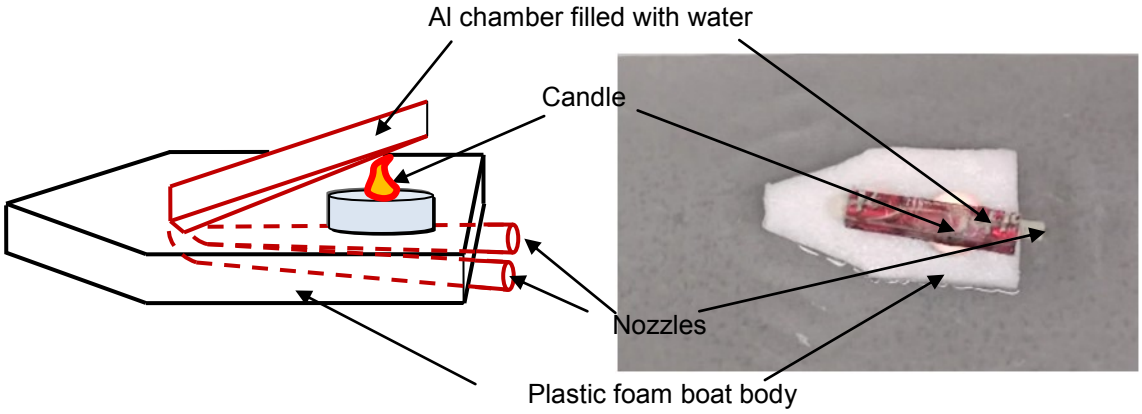

(a)

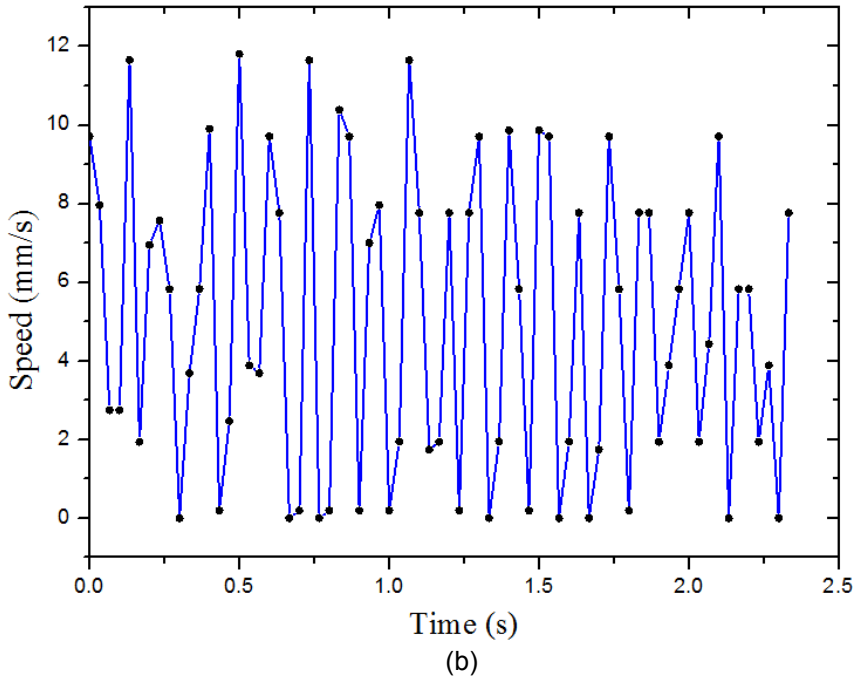

(b)

Figure 4.1: (a) A large putt-putt boat and its schematic, and (b) experimentally measured speed-time curve.

This small boat was fixed, and water inside its chamber was heated up by a commercial ceramic heater (resistance is 10 Ω) at an applied DC voltage of 5 V. It was clearly observed that, as described in [91], a propulsive cycle consisted of two processes: exhaust and suction. At the beginning of the exhaust process, the shallow chamber and pipe were filled with water (Figs. 4.2a1 and 4.2c1). Shortly after the resistive heater was turned on, steam formed in the shallow chamber. As more vapors were produced, pressure increased. Consequently, the steam drove part of water in the chamber and pipe out of the boat (Fig. 4.2a2). This part of water exited the rear of the boat in the form of a jet, completing the exhaust process (Figs. 4.2a3 and 4.2c2). After part of water in the chamber and the pipes were driven out by the heating, some part of vapor transported to the section with low temperature. It condensed back to water. Accordingly, pressure was reduced. When it was lower than the outside (atmospheric) pressure, water surrounding the boat was drawn into the pipes and chamber (Figs. 4.2b and 4.2c3). In the exhaust process, the water was jetted out of the pipe in the form of an approximately straight column (Fig. 4.2c2), while in the suction process, water was drawn into the pipe through all the directions (Fig. 4.2c3). Thus, the jetted water had a larger longitudinal component of linear momentum than the drawn water. According to conservation law of linear momentum, during a single propulsive cycle, the boat was driven forward.

The testing results of these two putt-putt boats indicate three points: (i) the thermal oscillatory approach may be applied to propel a submarine underwater, since the propulsion does not require that the propelled vehicle should stay on a liquid surface; (ii) a resistive heater, instead of a candle, can be applied to generate a jet at a low voltage (it was 5 V in the test); (iii) compared with other thermal approaches of propulsion, this thermally oscillatory method does not need fuel. Since it is simple to fabricate the required chamber, nozzle and resistive heater using microfabrication techniques, the thermal oscillatory method is adopted here to propel micro submarines.

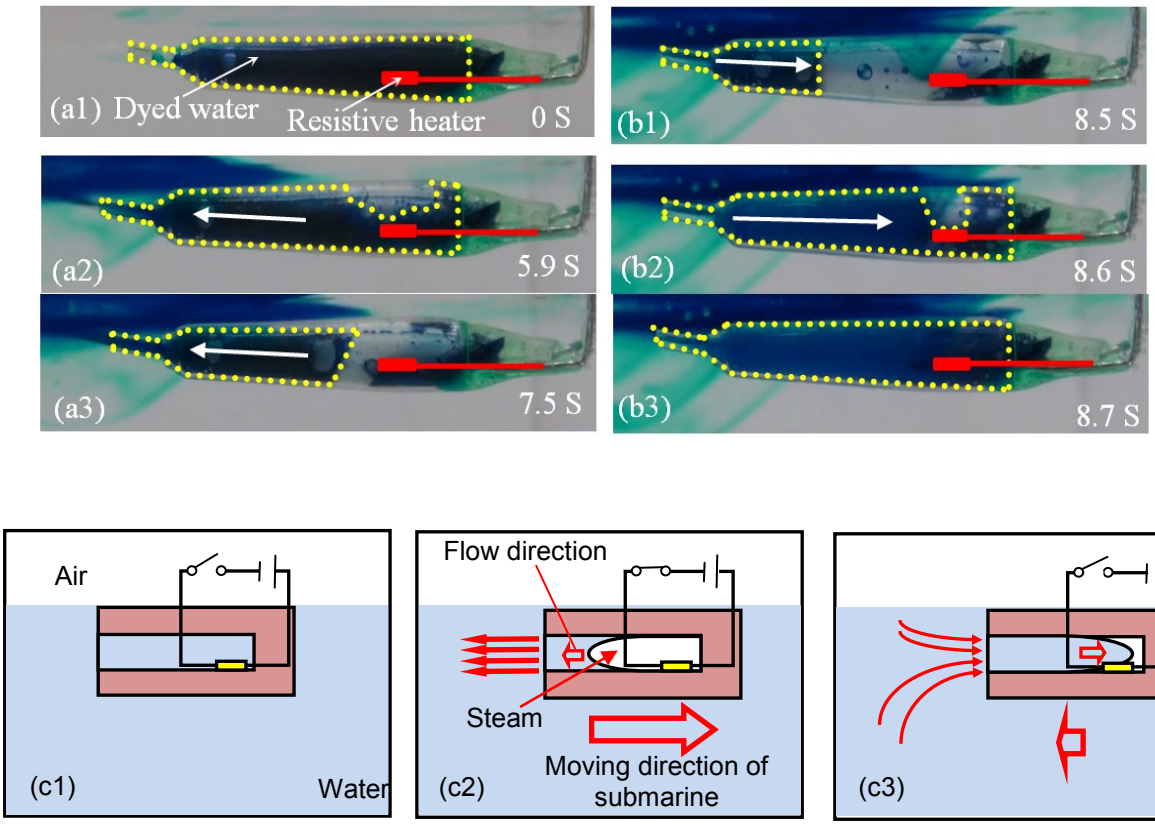

Figure 4.2: In-situ observed exhaust process at (a1) t=0 s, (a2) t=5.9 s, (a3) t=7.5 s. In-situ observed suction process at (b1) t=8.5 s, (b2) t=8.6 s, (b3) t=8.7 s. Illustration of a thermally oscillatory process: (c1) stationary state (heater is switched off), (c2) exhaust process, and (c3) suction process.

4.4 Design And Fabrication Of Micro Submarines

Based on the understanding gained in the preliminary tests on the putt-putt boats, the micro submarine is designed to have two portions (Fig. 4.3). The top portion includes two SU-8 layers (Fig. 4.3a). The second SU-8 layer has a reservoir and two nozzles, and the first SU-8 layer seals the tops of the reservoir and nozzles. The bottom portion includes a serpentine-shapes Au heater and two contact pads, which is located on top of an SU-8 layer (Fig. 4.3b). This SU-8 layer also seals the bottoms of the reservoir and nozzles. The thermal ejector consists of the Au heater, reservoir and two nozzles. Once the heater is turned on, the thermal ejector produces a jet, providing a thrust to drive the submarine along the direction opposite to that of the jet.

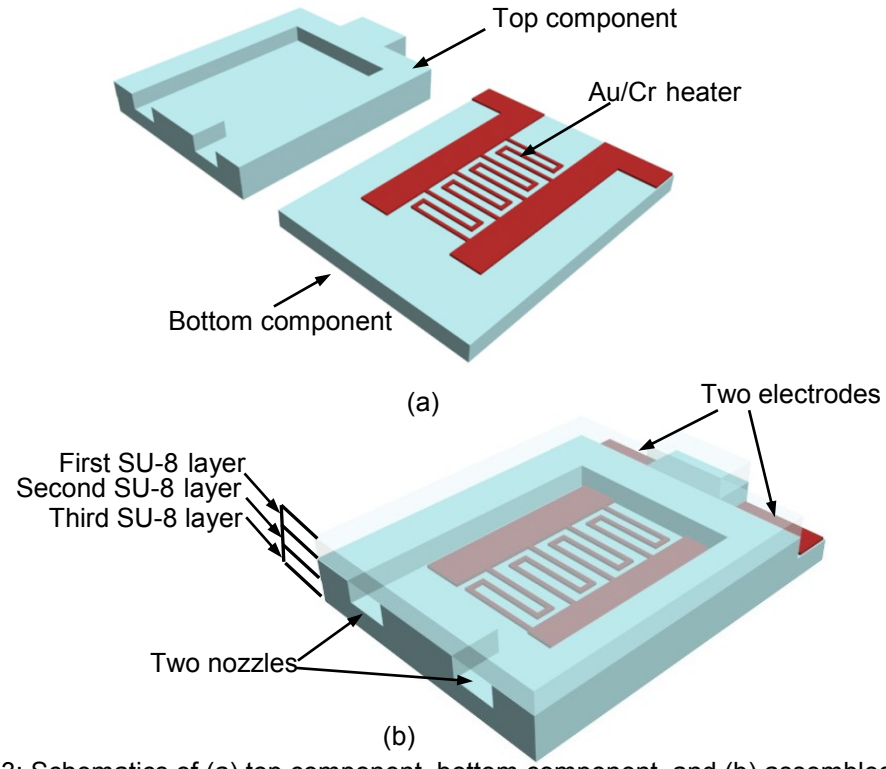

Figure 4.3: Schematics of (a) top component, bottom component, and (b) assembled microsubmarine.

Isopropyl alcohol (IPA) is chosen as the tested liquid, since it has a low mass density (0.76×10^3 kg/m^3) and low boiling temperature (82.5°C). SU-8 is chosen to be the structural material for micro submarines due to two reasons. First, the density of SU-8 is $1.16\text{x}10^3$ kg/m^3 (according to our measurement), larger than that of IPA. This difference in the two densities enables the SU-8 to stay under IPA. Second, SU-8 is a negative photoresist. It can be patterned to desired shapes using UV lithography and its thickness can be controlled for producing SU-8 submarines with proper thicknesses. SU-8 has been widely applied in the MEMS area for various high-aspect-ratio patterning purposes [92-94]. It can also function as a good structural material in microsystems, such as in bio microfluidic device [95,96], boats [9-12] and flotillas [13,14]. The density of PDMS is $0.97\text{x}10^3$ kg/m^3 [97]. It is not a photoresist. It is normally patterned by a molding process [98], which may not be good at three-layer patterning as required in generating a micro submarine. Since it is relatively simple to directly fabricate micro submarines out of SU-8 using UV lithography, this material is adopted in this work accordingly. Metals and silicon have much higher densities than water, and might not be good structural materials for micro submarines.

A three-step procedure given below is adopted to fabricate the micro submarines (Fig. 4.4): (i) generate the bottom portion (Fig. 4.4a), (ii) produce the top portion (Fig. 4.4b), and (iii) bond the two portions together, followed by bonding two Au wires (interconnects) to their contact pads (Fig. 4.4c).

In the first step (Fig. 4.4a), an SU-8 layer is patterned on top of an S1813-coated Si wafer using UV lithography, followed by the generation of Au heaters and contact pads on this layer using UV lithography. S1318 is a positive photoresist, and is employed here as the sacrificial material to release SU-8 structures from the Si wafer as will be seen in the second and third fabrication steps.

The second step includes three sub-steps (Fig. 4.4b): (i) spin-coat the first SU-8 layer on a S1813-coated Si wafer, and pattern it to form the top layer of a submarine using the UV lithography; (ii) spin-coat the second SU-8 layer on the first one, and pattern it to form the middle layer of the submarine using the UV lithography; and (iii) remove these two SU-8 layers (i.e., the top portion of the submarine) from the Si wafer by etching S1813 using its developer.

The third fabrication step includes four sub-steps. In the first sub-step, the SU-8 layer in the top portion is first coated with a thin SU-8 coating, the top portion is then flipped over and placed on the top of the SU-8 layer of the bottom portion, and finally the whole sample is heated at 95 °C for 30 min to cure the thin SU-8 coating. In the second sub-step, the whole sample is released from the Si wafer by etching S1813 using its developer. In the third sub-step, two identical Au wires with a diameter of 25 μm are connected to the two contact pads of the submarine, respectively, using conductive silver epoxy. Finally, in the fourth step, the top surface of micro submarine was coated by a layer of Teflon completing the fabrication of micro submarines.

A representative micro submarine is generated and its dimensions are given in Figs. 4.5(a) and 4.5(b). The top, middle and bottom layers of SU-8 are 200, 500 and 260 μm thick, respectively. The reservoir and nozzle had the dimensions of 5 × 4 × 0.5 mm3 and 1 × 1 × 0.5 mm3, respectively. The total mass of the micro submarine is 39 mg, and the total volume of the reservoir is 12 mm3. The electrical resistance of the Au heater is 450 Ω. The Au heater has a serpentine-shape line, which is 100 μm wide and 48.6 mm long, separated by a spacing of 100 μm (Fig. 4.5c). As shown in Fig. 4.3(d), using the above fabrication process, we have generated a prototype of micro submarines. The prototype is 8 mm long, 6 mm wide and 0.96 mm thick (Fig. 4.5a-b).

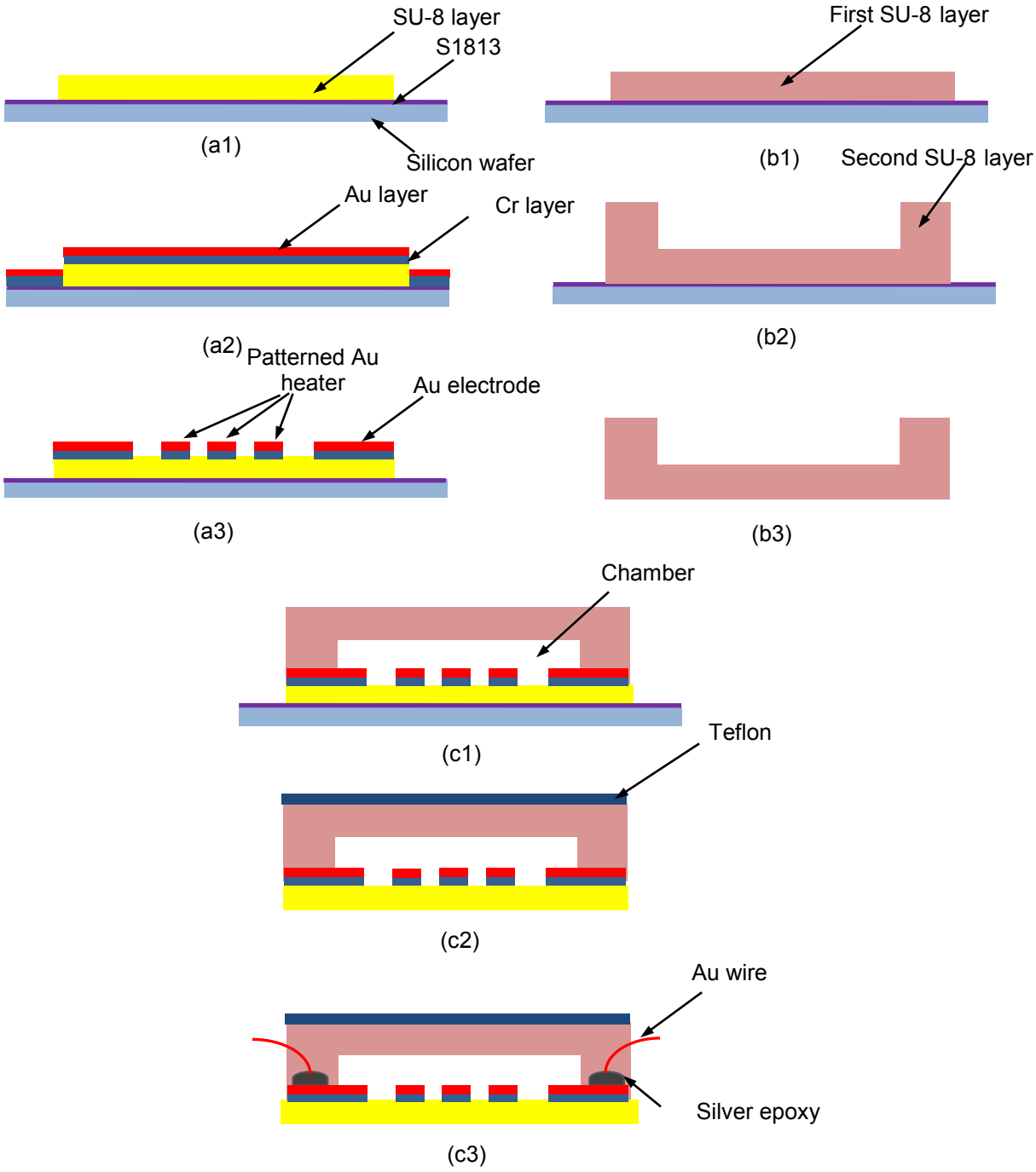

Figure 4.4: Procedures to fabricate the microsubmarine (not to scale): Procedures to fabricate (a) the bottom and (b) top portions. (c) Procedures of bonding top and bottom portions together, and connect them with the interconnects (two Au wires) them.

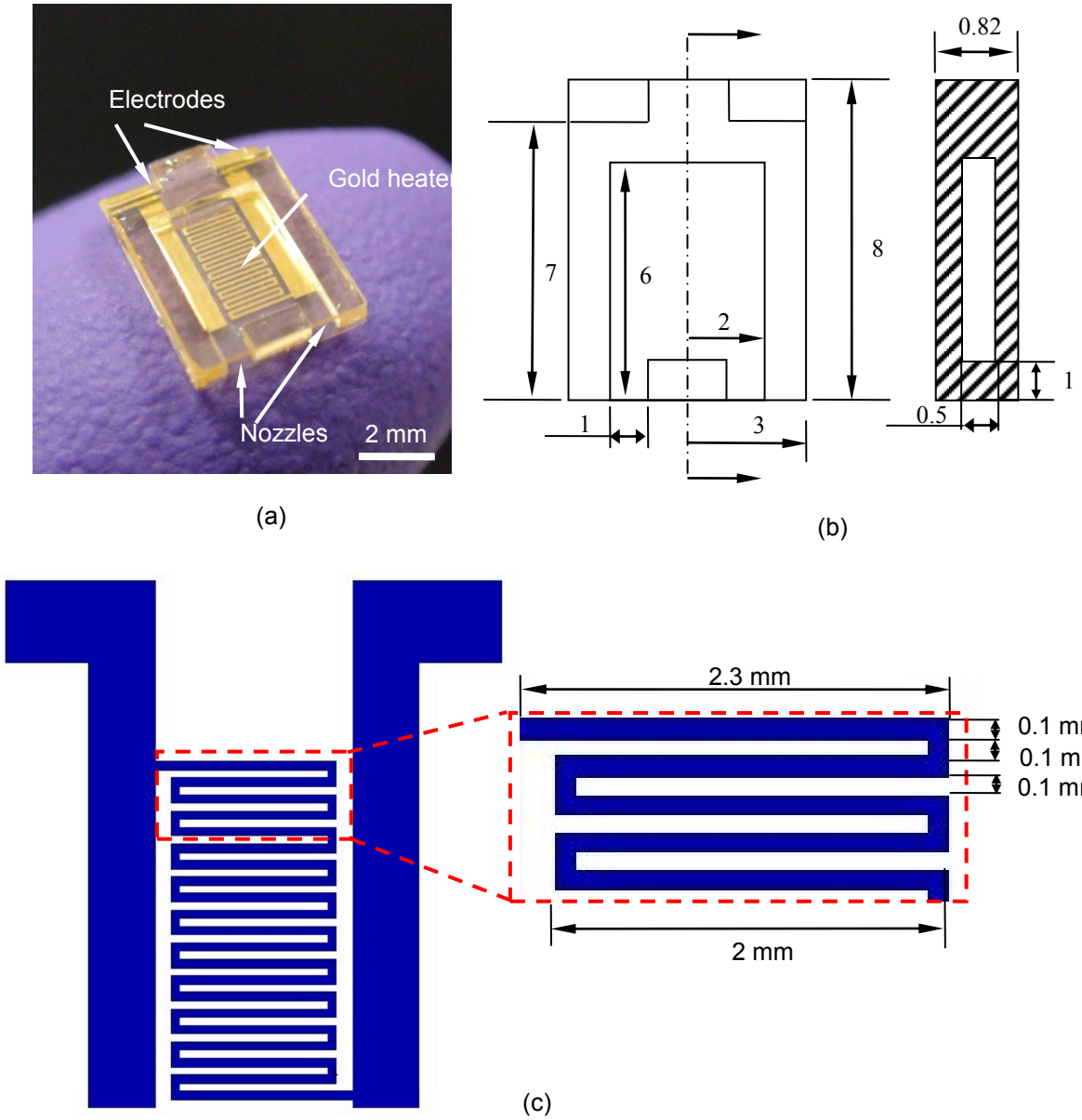

Figure 4.5: (a) Fabricated microsubmarine, (b) dimensions of the microsubmarine (unit: mm) and (c) dimensions of the heater.

4.5 Experimental Results And Discussions

Three types of tests are done to explore the performance of the micro submarine, which are presented in the following three sub-sections, respectively. The first type of tests is to examine the thermal oscillatory process, the second type is to optimize applied voltage, pulse frequency and duty for the purpose of maximizing the propulsive force generated during a thermal oscillatory process, and the third is to investigate the motion of the submarine. In all the tests, the actuating pulse was generated by a power system consisting of a function generator (SFG-2004 of Instek) and a power amplifier (PZD350A-1-L-CE of Trek) (Fig. 4.6a). All these tests are conducted in a plastic container with a diameter of 9 cm, which is partially filled to a depth of 0.5 cm with IPA. In the first and second types of tests, the submarine is fixed (Fig. 4.6b), while it is not in the third type of tests (Fig. 4.6c). The behaviors of vapor bubbles in the first and third types of tests are recorded using a video camera (HDR-XR500 of SONY with a rate of 30 frames per second), while such behaviors under high pulse frequency in the second type of tests is recorded using a high-speed video camera (TS3-61 of Fastec with a rate of 1250 frames per second).

4.5.1 Thermal Oscillatory Process

As what was done in the second preliminary test introduced in Section 2, a voltage of 5 V was continuously supplied to the Au heater in a micro submarine. We found that, due to overheating, this heater was broken shortly after it had been turned on. Accordingly, in the subsequent tests, the applied voltage was provided in a form of square waves (i.e., increase and decrease the voltage in a periodic manner) to avoid overheating of the heater. In addition, to observe the flow patterns around the submarine, particularly around the nozzle area, during a thermal oscillatory process, the IPA solution in the plastic container was mixed with dark PEDOT particles, which have diameters in the range of 100 to 500 μm.

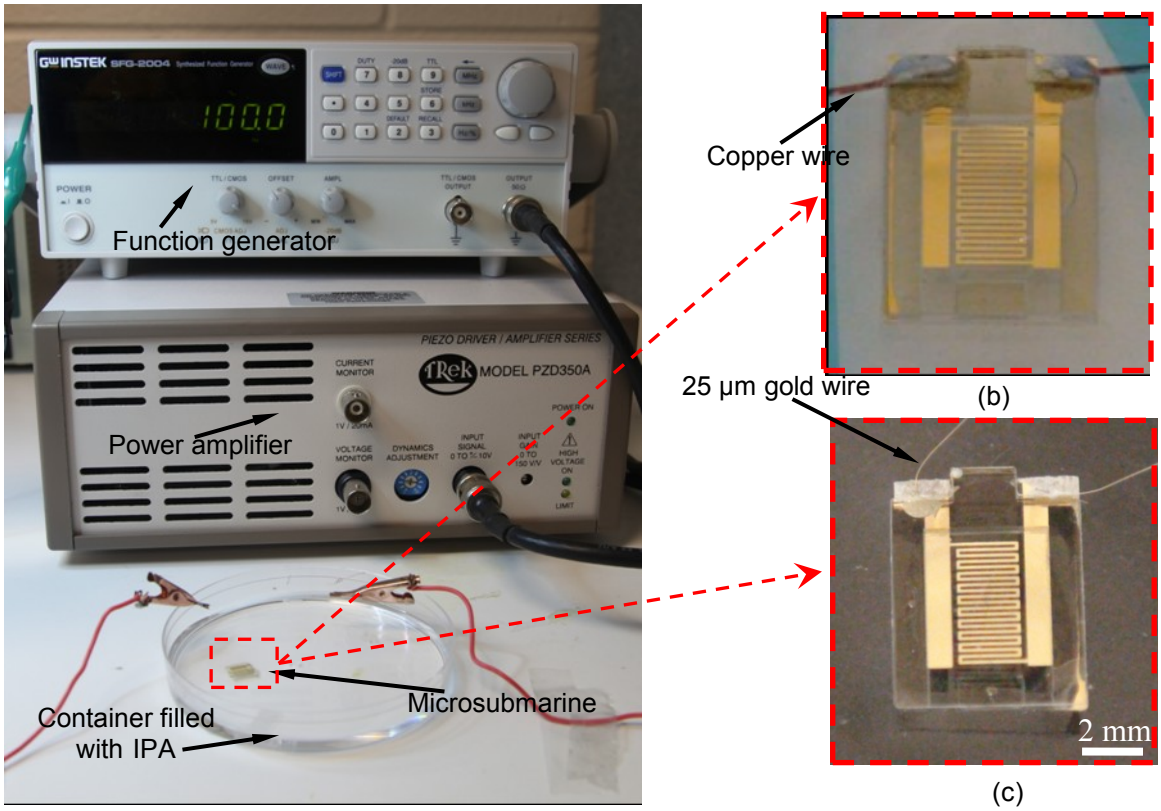

Figure 4.6: Experimental setup has the (a) Power amplifier and function generator was used to power the micro submarine in all tests, (b) the micro submarine was connected and by copper wires in first and second test and (c) the micro gold wires in third test respectively.

The behaviors of thermal bubbles were observed at an applied voltage of 13 V and a pulse frequency of 1 Hz. A representative relationship of the bubble volume with time is given in Fig. 4.7 There existed four stages during a thermal oscillatory process, in which a bubble had different behaviors. At the first stage (0 to 7 s), it took 3.2 s for a bubble to nucleate at the heater surface, and the bubble then continued to grow until t=7 (the corresponding volume was 0.25 mm3). At the second stage (7 to 25 s), the bubble started to have obvious expanding and shrinking behaviors, while it still increased its size. At the third stage (25 to 35 s), after t=25 s, its volume reached the maximum values of 3.5 mm3 in expansion and of 2.5 mm3 in shrinkage in a cycle. The volumes remained about the same during different cycles. The heater was turned off at the fourth stage when t>35 s. The bubble gradually decreased its volume to 1.1 mm3 at t=43 s, and remained this volume for at least 5 min. In addition, we noticed that the

oscillating frequency of the bubble was the same as the applied pulse frequency at the second and third stages. In the second and third types of tests, we mainly used the behaviors of the bubbles in their third stage, since they had repeatable behaviors at this stage.

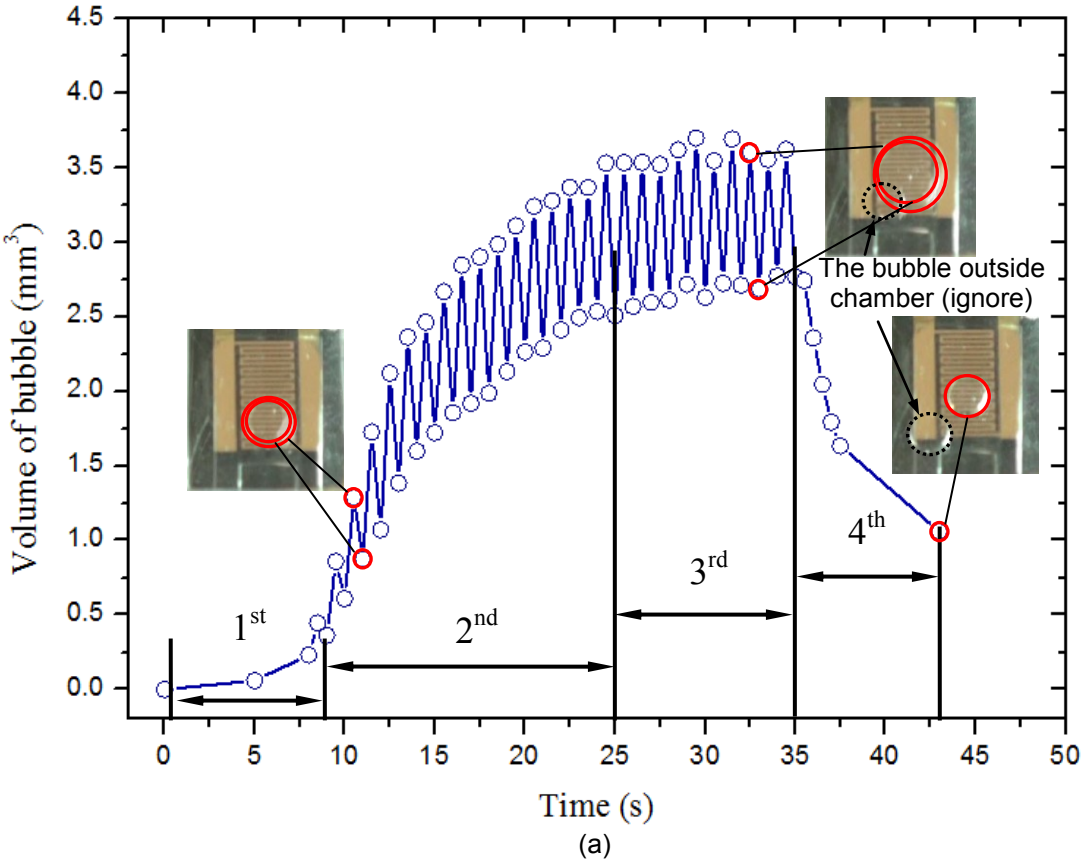

(a)

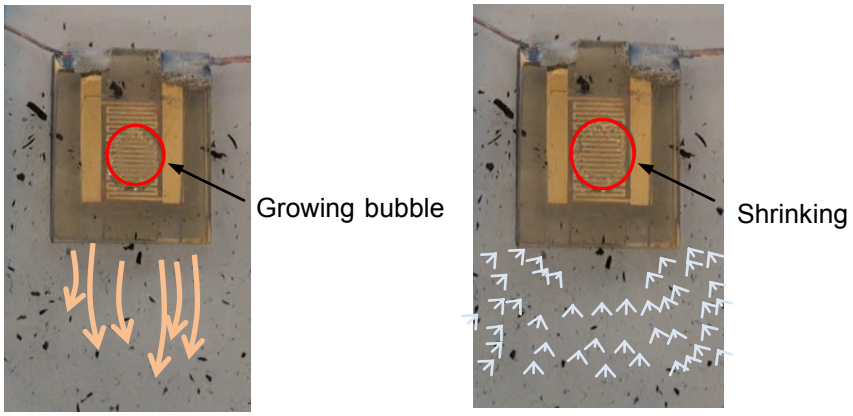

(b1) (b2)

Figure 4.7: (a) The behavior of the generated bubble when the applied voltage is 13 V, pulse frequency is 1 Hz and duty is 50%. Flow pattern behind the micro submarine when bubble was (b1) growing and (b2) shrinking. The arrow shows the moving direction and speeds of particles.

The ejection and suction of IPA during a thermal oscillatory process were similar to those found in the case of the second preliminary test (Fig. 4.2). During the exhaust process, when a bubble gradually increased its size, the particles located outside the nozzles moved away from the nozzles in a jet form (Fig. 4.7b1), indicating that an IPA jet was ejected from the reservoir. In the suction process, as the bubble gradually shrank, the particles behind the submarine were moving back towards the nozzles from almost all directions (Fig. 4.7b2), implying that IPA was drawn into the reservoir through almost all the directions. Accordingly, due to the difference between the exhaust and suction processes in the flow directions, a thrust should be produced to drive the submarine forward.

4.5.2 Optimization of parameters

In order to optimize applied voltage, pulse frequency and duty for the purpose of maximizing the propulsive force, we estimate the mean propulsive force generated during a cycle of thermal oscillation. It can be seen from Eqs. (4.6) that the thrust of the putt-putt boat are directly related to the exit speed of the jet during the exhaust process. Thus, to control the motion of such a boat, it is important to know how to control this speed during the exhaust process.

Let V and V_b denote the volumes of the reservoir and vapor bubble, respectively. V is constant, while V_b is a function of time (t) in a period. T is the period while T_e is the pulse duration in one cycle. We have

$$\{[U_e{}^2]\} = \frac{1}{a^2 T}\int_0^{T_e}[\frac{d(V-V_b)}{dt}]^2 dt = \frac{1}{a^2 T}\int_0^{T_e}(\frac{dV_b}{dt})^2 dt. \quad (4.11)$$

According to Eq. (4.11), in order to determine $\{[U_e{}^2]\}$, it is necessary to know $\frac{dV_b}{dt}$ and T_e, which are determined through experiments. At a time instant, V_b is calculated as the multiplication of the lateral bubble area with the reservoir height. As shown in Fig. 4.8, the

volume-time relations were experimentally determined, respectively, at frequencies of 1, 10, 25 and 50 Hz when applied voltage and duty were fixed to be 13 V and 50%. For each frequency, as well as in the tests that will be subsequently presented, the volume of the bubble first linearly increased during the expansion process and then decreased with time during the shrinking process. Let $k = \frac{dV_b}{dt}$ denote the slope of the volume-time curve at the expansion process. Accordingly, *k* is a constant for a given pulse frequency, and Eq. (4.11) becomes

$$\{[U_e^{\,2}]\} = \frac{k^2 T_e}{a^2 T}. \tag{4.12}$$

Let *D* denote the duty. Then, we have

$$D = \frac{T_e}{T}, \tag{4.13}$$

which actually equals the applied duty. Subsequently, with the aid of Eqs. (4.12) and (4.13), Eq. (4.6) can be re-written as

$$\{[P]\} = \frac{\rho k^2 D}{a}. \tag{4.14}$$

This equation implies that the thrust increases with the increase in both D and k. In addition to duty, applied voltage and pulse frequency also affected the thrust. Thus, to generate a large thrust, next we determined the optimal values of these three parameters in the following order: (i) fixed the duty and pulse frequency and determined an optimal value of applied voltage, (ii) fixed this optimal value of applied voltage, together with the duty, and found an optimal value of pulse frequency, and (ii) determined an optimal value of the duty when the optimal values of another two parameters were fixed. During this process of finding the optimal values, the corresponding trust was determined using Eq. (4.14).

We first fixed duty to be 50% and frequency to be 1 Hz, determined the relationship of k and voltage, and further calculated the relationship of the trust and voltage. Based on Eq. (4.14), since the duty was fixed, the thrust increased or decreased with the increase or decrease in k (Fig. 4.9). Four points were found. First, when the applied voltage from 1 to 16 V (Fig. 4.9), the thrust also increased, had a peak value at 16 V, and started to drop at 19 V. Second, at 22 V, only the second stage was observed, which meant the bubble grew and oscillated simultaneously. After about 20 s of growth at this applied voltage, the IPA vapor occupied the whole chamber, no liquid IPA was ejected out of the reservoir, and also no liquid IPA was sucked into the reservoir. Thus, there was no thrust during such a cycle. When the IPA bubble further expanded, part of this bubble got out of the chamber, and was broken away from the part of the bubble still inside the reservoir. Subsequently, liquid IPA was able to be sucked back in the chamber, restarting the thermal oscillatory process. Third, when the applied voltage was 22 V or above, the heater would be broken after running for 2 min or longer. Since most of time the reservoir was occupied by IPA vapor only, the temperature of the heater kept increasing, making this heater easy to break. Thus, the largest voltage tested in our experiments was 22 V. Fourth, if the voltage was lower than 10 V, the thrust would be small. At 1 and 4 V, the heat generated by heater was not even large enough to nucleate a visible bubble. Only after applied voltage beyond 7 V, the bubble was generated and its size slightly increased with the increase of voltage.

We then fixed the voltage and duty to be 16 V and 50 %, respectively, and found the relationship between the thrust and pulse frequency, which varied from 1 to 500 Hz (Fig. 4.10). We found that the thrust has a maximum value at 100 Hz (Fig. 4.10). The value of the thrust first increased with increase of frequency and then decrease with it. The largest thrust was obtained at the frequency of 100 Hz. If the frequency was too high (such as 300 Hz), the bubble behaved as in the case that voltage was continuously applied. The accumulation of heat made the corresponding bubble not shrink much during a cycle, and consequently not much liquid IPA

was sucked into the reservoir, resulting in a small thrust. In case the frequency was too low (such as 1 Hz), the accumulated heat was not large enough for the bubble to grow quickly, also resulting in a small thrust. As observed from Fig. 5.10, 100 Hz was an optimal frequency, yielding the largest k and the thrust.

Finally, we fixed the voltage as 16 V and frequency as 100 Hz to study the relationship between the thrust and duty. As seen from Fig. 4.11, the duty was varied from 20% to 80% with an increment of 10%. The thrust initially increased when the duty increased from 20% to 50%, and then decreased when the duty increased from 50% to 80%. Hence, the largest thrust appeared at duty of 50%, which was 67.6 nN.

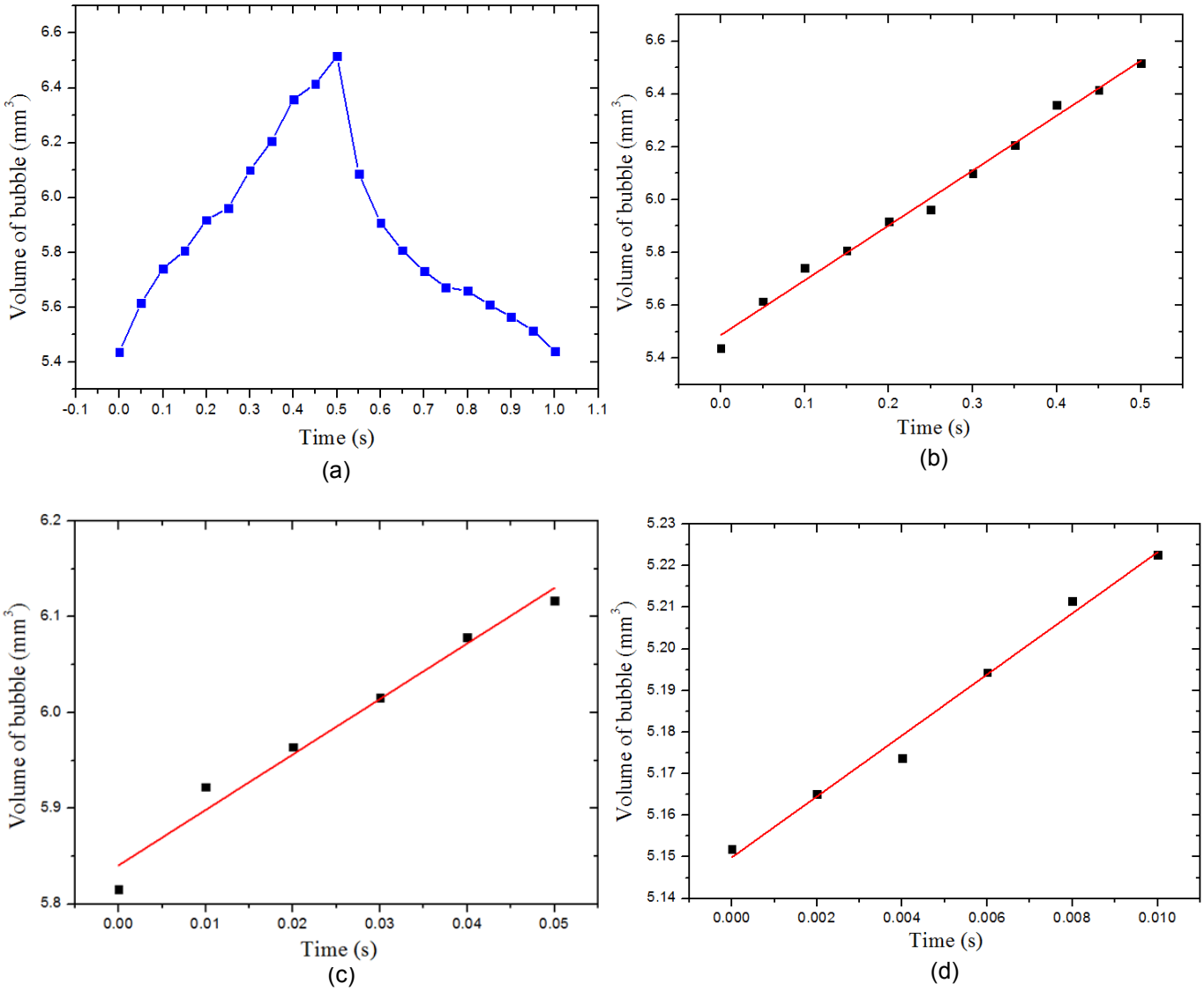

Fig. 4.8: Volume-time relationship in one cycle when frequency is (a) 1 Hz. Volume-time relationship and linear curve fitting during bubble growth in one cycle when frequencies are (b) 1, (c) 10 and (d) 50 Hz and duty is 50%.

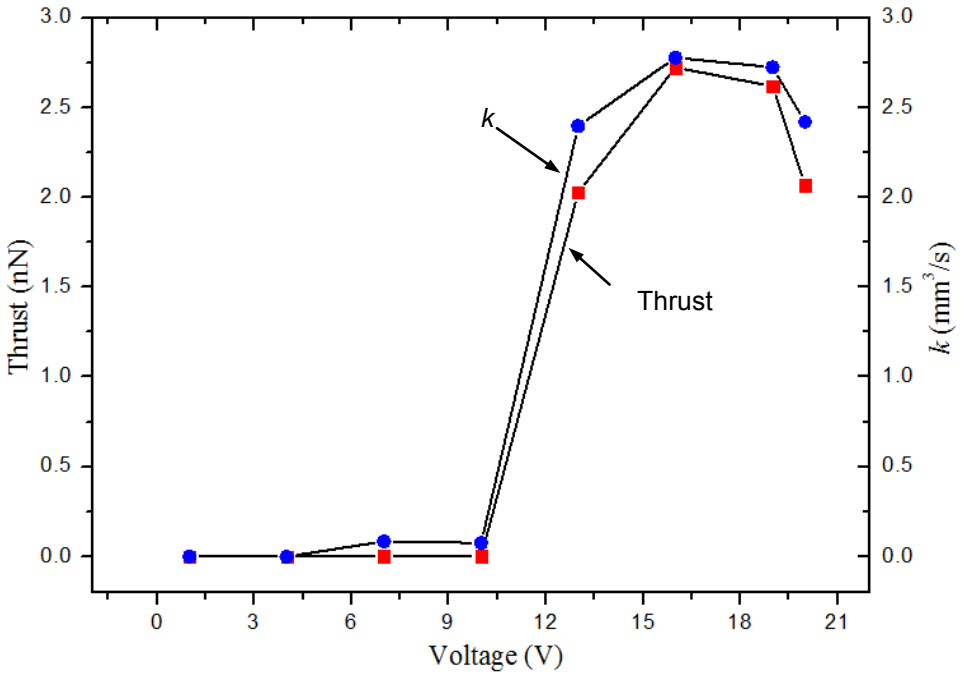

Figure 4.9: Thrust- and *k*-voltage relationships when frequency is 1 Hz and duty is 50%.

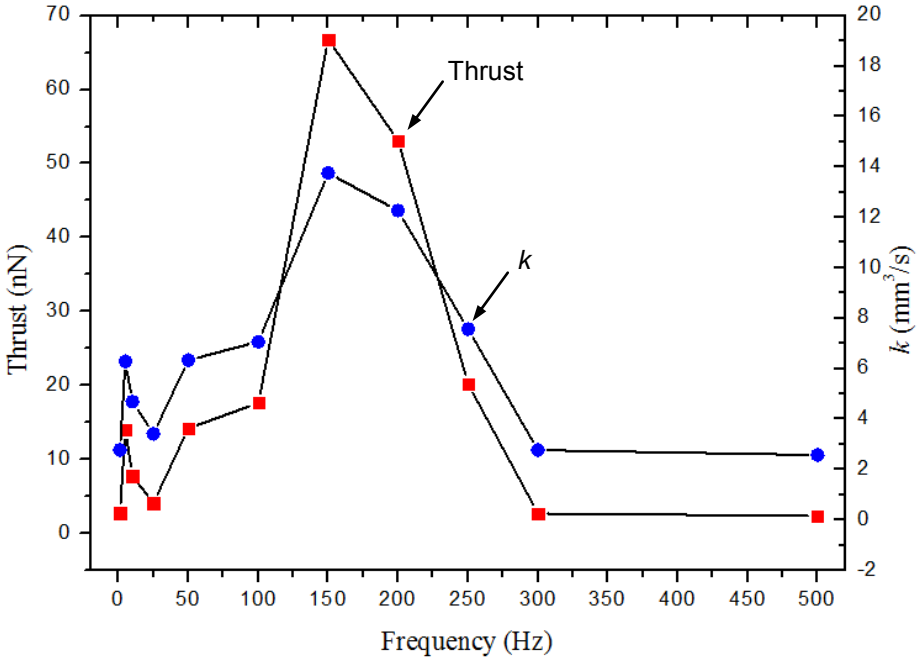

Figure 4.10: Thrust- and *k*-frequency relationships when voltage is 16 V and duty is 50%.

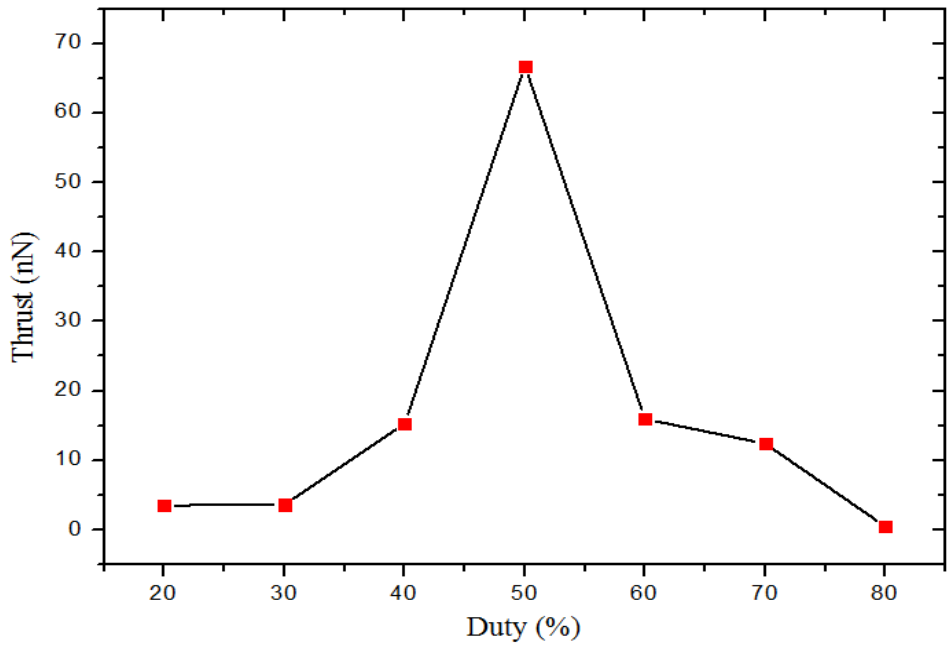

Figure 4.11: Thrust-duty relations during a cycle at 16 V and 100 Hz.

In summary, in the second type of tests, the optimal values of voltage, frequency and duty were, respectively, 16 V, 100 Hz, and 50%, resulting a thrust of 67.6 nN.

4.5.3. Motions

In order to examine the motion of micro submarine, we did the third type of tests, and connected it with two Au wires with identical diameters of 25 μm. Due to the constraint of the Au wires, which linked the prototype of the submarine to the external power-supply device, the moving path of the submarine was slightly curved. When the applied voltage was 16 V, the pulse frequency was 100 Hz and duty was 50 %, it took the submarine about 4 s to start moving, reached the highest speed of 1.8 mm/s at 9.5 s, and stopped at 17 s due to the balance of the thrust with the forces provided by the two Au wires (Fig. 4.12). The total travel distance was 12.6 mm.

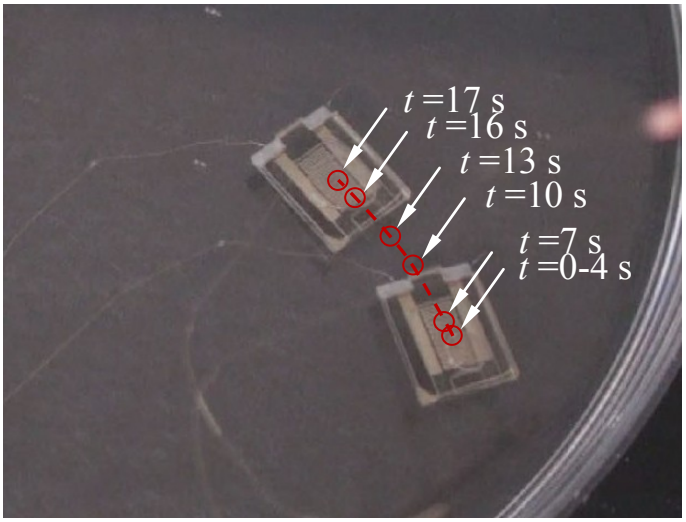

(a)

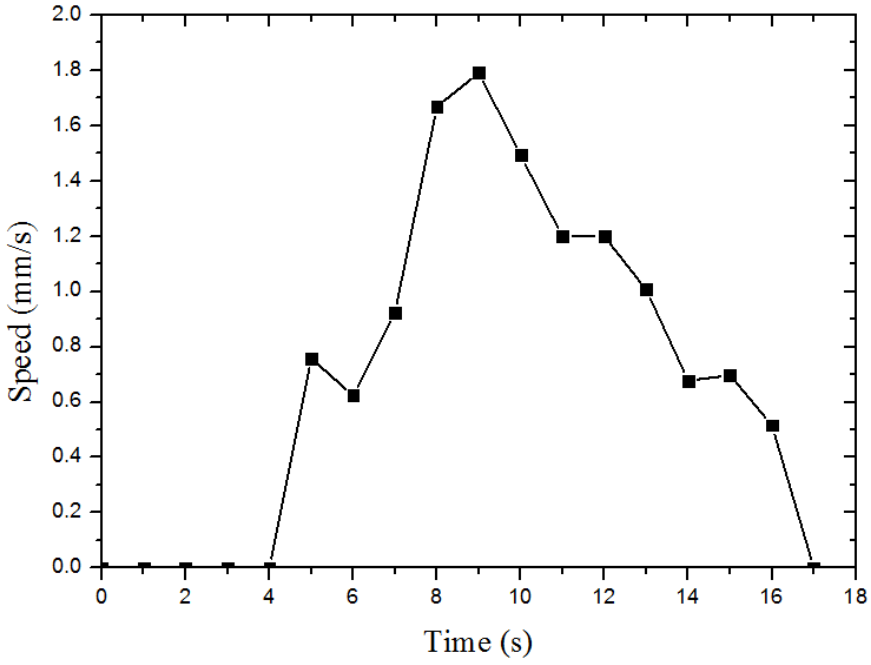

(b)

Figure 4.12: Experimental results: (a) sequential snapshots of a radial motion for the micro submarine constrained by two micro gold wires (frequency equals 100 Hz, voltage is 16 V and duty is 50%; red circles represent the geometric center of the microsubmarine), (b) the speed-time curve.

The submarine mainly suffers IPA resistance and the wire constraint. The IPA resistance slows down the submarine, while does not limit the travel distance of this submarine. On the other hand, in addition to the speed, the Au wires particularly limit the travel distance of the prototype. Accordingly, we estimate the effect of these two wires on the travel distance. In the experimental setup, the wires are suspended in air to avoid their contact with IPA, since we found that such contact increased their resistance to the movement of the submarine. One end of the two wires is fixed on the wire-supply device, and the other end is attached to the submarine and moves with it. Let's denote the two ends by a and b, respectively. We set up a simple model to understand the constraint of these two wires, which are combined together and modeled as a cantilever beam. The end a is considered to be fixed. However, the end b is open, but suffers a concentration force, which equals the thrust of the submarine at the end of the motion when this submarine stops movement. Let P and L denote this concentration force and the average length of the two wires. Thus, we have [99]

$$\delta = \frac{PL^3}{3EI}, \tag{4.15}$$

where δ denotes the deflection at b, E is Young's modulus of Au wires, which was measured to be 58 GPa, and I is the area moment of inertia of the two wires, whose expression is $I = \frac{\pi d^4}{32}$ with d as the wire diameter. It is observed from Eq. (4.15) that δ increases with the increase in P and L while decreases with the increase in d. In our case, the wires with diameters as small as 25 μm are used, the maximum length of the two wires is 10 cm (the longer ones are easy to bend and get contact with IPA), and P equals the optimized thrust of 67.6 nN. Subsequently, by Eq. (4.15), δ is estimated to be 10.1 mm. This result implies that, for the given setup and prototype, the maximum travel distance should be in the order of 10 mm. This is actually our case, in which the maximum travel distance measured is 12.6 mm. Although the further optimization of the setup and the submarine, such as reduction of the wire

diameters, increase of their effective lengths and improvement of the thrust, may increase the travel distance, it is expected that the total travel distance is still limited due to the constraint of the wires. Hence, in the near future, we plan to develop wirelessly powered submarines, which eliminate the need of wire connection, for the purpose to increase their travel distances.

In addition to testing the prototype using the optimized parameters obtained in the second type of tests, we also fixed the duty to be 50%, and examined its motions by varying applied voltage and pulse frequency: applied voltage was changed from 1 to 22 V with an increment of 3 V, and the pulse frequency of the voltage varied from 1 to 500 Hz. In all cases, it took 1 to 5 s to form a visible, oscillating bubble in the reservoir. Three situations were observed regarding the mobility of the submarine. First, when the applied voltage was 7 V or below, the submarine did not move for any tested frequency, indicating that the generated thrust was not large enough to overcome the constraint of the Au wires. Second, the submarine began to move when applied voltage was 13 V for all the tested frequencies. Third, at an applied voltage of 22 V, the submarine moved first. However, after t=10 s, it stopped for 1-2 s and restarted again. The four points observed in the second type of tests actually explained the occurrence of these three situations.

4.6 Summary And conclusions

In this work, through experimental and theoretical investigations, we developed the prototype of a micro submarine based on a thermally oscillatory approach of propulsion. We investigated the design, fabrication, actuation and horizontal motions of this prototype. The prototype had a thermally oscillatory process similar to that of the putt-putt toy boat. The propulsive parameters were optimized. At an applied voltage of 16 V, pulse frequency of 100 Hz, and duty of 40%, the submarine was found to have the speed as high as 1.8 mm/s and the travel distance as long as 12.6 mm. The corresponding thrust was calculated to be 67.6 nN. Also, it was considered that the constraint of the wire connections limited the travel distance of the submarine. Thus, in the near future, we plan to develop wirelessly powered submarine to

eliminate this constraint. Furthermore, in this work, we focus on the horizontal motions of the submarine. In the near future, we also plan to explore its vertical motions (i.e., rising and sinking under liquid), as well as and corresponding design, based on our recent work, which used trapped bubbles to increase buoyancy for the purpose of raising a small object from under liquid [100].

CHAPTER 5

FLOATING UP OF A MICROSUBMARINE IN WATER USING MICROPILLARS

In last chapter, we demonstrate the possibility of using a novel driving mechanism to propel a micro submarine under water. Beside the longitudinal motion, we also have interests to explore its vertical motion. Submarines use upthrust to sink or float. The upthrust is generated by changing the average density of a submarine. A tank usually is adopted in submarine. If a submarine is about to dive, its average density is increased by pumping water into the tank. When the average density of the submarine is greater than that of seawater, it happens by displacing water, it begins to sink. In the opposite, by pumping water out of the tank, the submarine will float up.

Due to the difficulty of introducing a sealed tank into a micro vehicle, we explored a novel technique to decrease the average density of the micro submarine. In this chapter, we demonstrate the possibility of floating up a micro submarine by incorporating micropillars onto its surfaces. Air is trapped in between micropillars, so the average density of the micro submarine is lowered. This technique also apply to other under water device for example micro submarine or micro robot. In the near future, we would explore the technique of control the volume of trapped air.

5.1 Mechanism Of Air Trapping

When a water droplet is placed on a solid rough surface, it may stay one of two possible states those are Wenzel state [101] and Cassie-Baxter sate [102] (Fig. 5.1). In the Cassie-Baxter state, water drop only partially contact with the solid surface. A layer of the air is trapped in between the micro structures on the surface. On the contrary, in Wenzel state, the water fully contact with the solid surface. There is no air trapped in between. When the droplet is resting on

the surface and surrounded by gas, a characteristic contact angle θ is formed. When contact angle is larger than 90°, we consider the surface as one with low wettability. It is also called hydrophobic surface. The reason why water does not penetrate into the gaps of the micropillars is because the effort of the surface tension. When a rough surface is fully submerged in water, air may also be trapped in between the micro structures. Because the density of the air is very low compare to a solid fragment, its average density will be decreased due to the trapped air. It will float up in water after it is fully submerged. When the fragment is located at a higher water depth, the water pressure will push the water into gaps and squeeze the air into a smaller volume. Therefore, after the fragment is pushed beyond certain depth, it cannot float up anymore.

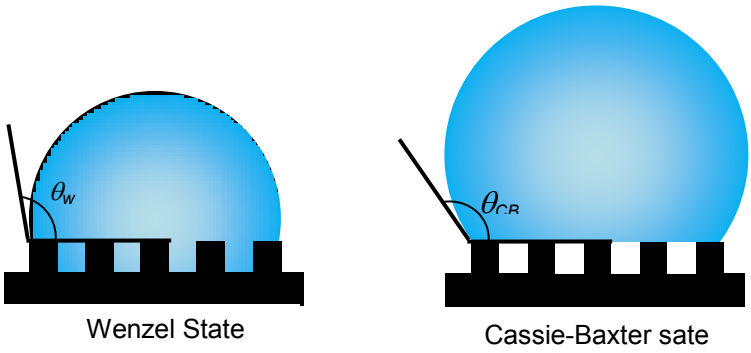

Figure 5.1: Schematics of the Wenzel state and the Cassie-Baxter state.

5.2 Design Principles And Theoretical Modeling

Without loss of generalization, in this work we consider the case that an array of micropillars is incorporated on the bottom of a solid fragment (Fig. 5.2). The analysis below also applies to the case that the micropillars are incorporated on the top of a solid fragment. Let V_s and *t* denote the volume and thickness of the solid fragment respectively. Micropillars may have rectangular or circular cross-sections (Figs. 5.2b and 5.2c). In Sub-sections 5.2.1 and 5.2.2, we first consider the situation that rectangular micropillars are used to increase buoyancy of a solid fragment. The corresponding results are then modified for the case of circular micropillars in

Sub-section 5.2.3. Set a_1, a_2, and t_p, respectively, denote the length, width and height of a rectangular micropillar (Fig. 5.2b). Let b_1 and b_2 denote the distances between neighboring micropillars along two lateral dimensions, respectively. Set S_p to be the surface area of the region covered by the rectangular micropillars (Fig. 5.2b). We consider two cases. In the first case water does not get into the gaps between micropillars when a solid fragment is placed under water. This implies that air/water interfaces are suspended at the top edges of the micropillars, and that air trapped in the gaps between micropillars is not much compressed. However, in the second case, water gets into the gaps between micropillars, air/water interfaces are stationary on the side surfaces of the micropillars, and trapped air is compressed. These two cases are considered in Sub-sections 5.2.1 and 5.2.2, respectively.

5.2.1 The case when the gaps between micropillars are not filled with water

When the micropillar-covered fragment is released under water, along the vertical direction the fragment suffers four forces (Fig. 5.2d): gravity, water pressure-induced force, air-pressure induced force, and surface tension-induced force. Let G, F_w, F_a, and F_s, respectively, denote the magnitudes of the vertical components of these four forces. Set p_0 to be atmospheric pressure. Since the trapped air is not much compressed, its pressure is still considered to be p_0. Based on this point and pressure distributions, we have

$$G = \rho_s g V_s + n\rho_p g a_1 a_2 t_p,$$

$$F_w = \rho_w g(V_s + na_1 a_2 t_p) - (S_p - na_1 a_2)[p_0 + \rho_w g(h+t)],$$

$$F_a = p_0(S_1 - na_1 a_2)\ F_s = -\gamma \cos\theta L, \tag{5.1}$$

where ρ_w, ρ_p and ρ_s represent densities of water, pillars and solid fragment, respectively, n is the number of micropillars generated on the fragment, γ is surface tension of water, L is the total length of air/water/solid contact lines (these lines are marked in Fig. 5.2b), and θ is local

contact angle on the micropillars (Fig. 5.2d). Set θ_e to be intrinsic contact angle on the micropillars. Since these micropillars are considered to have hydrophobic surfaces, $\theta_e > 90°$. When air/water interfaces are suspended on the top edges of micropillars, $90° < \theta \le \theta_e$ [65, 66].

Define *F* to be

$$F = F_w + F_a + F_s - G. \tag{5.2}$$

Accordingly, based on the balance of the four forces along the vertical direction, the fragment rises up to water surface or moves down to water bottom when $F>0$ or $F<0$.

To have a better understanding about *F*, we explore the relation between surface tension and water pressure. Consider force balance on part of the air/water interface around a micropillar (Fig. 5.3). Due to geometric symmetry, surface tension applied on the outer boundary of the considered interface is along the horizontal direction. In the vertical direction, this part of the interface suffers surface tension (applied on the inner boundary of the interface), water pressure and air pressure (Fig. 5.3b). Let *H* denote the height difference between the outer and inner boundaries of this interface. When air/water interfaces are suspended on the top edges of micropillars, the maximum height difference (i.e., the maximum deflection of an air/water interface), $H_{\max}$, is [67]

$$H_{\max} = \frac{\sqrt{b_1^{\,2} + b_2^{\,2}}\,(1 - \sin\theta_e)}{2\cos\theta_e}, \tag{5.3}$$

which corresponds to the situation that $\theta = \theta_e$, and $\sqrt{b_1^{\,2} + b_2^{\,2}}$ represents the distance between two diagonal micropillars (Fig. 5.3b). The micropillar heights are required to be much larger than $H_{\max}$, i.e.,

$$t_p >> H_{\max}. \tag{5.4}$$

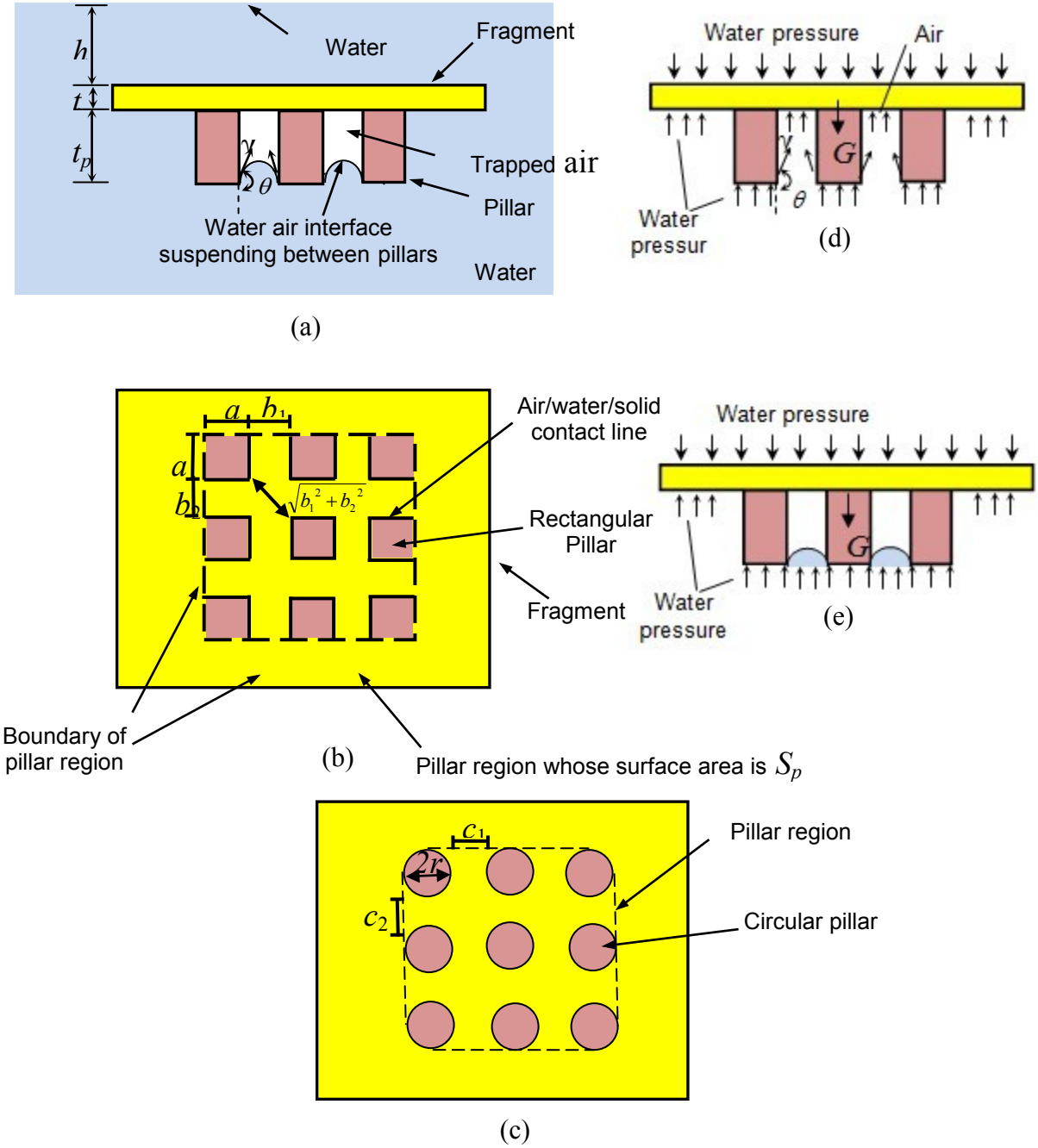

Figure 5.2: (a) Side view of a micropillar-incorporated fragment. Bottom views of this fragment when it was incorporated with (b) rectangular or (c) circular micropillars. (d) Free-body diagram of a micropillar-incorporated fragment. (e) Free-body diagram of the object formed by the micropillar-incorporated fragment, trapped air, and small neighborhoods of air/water interfaces. Only three pillars are drawn in (a) to have enough space to show air/water interfaces clearly. Thick, solid lines in (b) are air/water/solid contact lines. Also, vertical components of water and air pressures were considered in the two free-body diagrams.

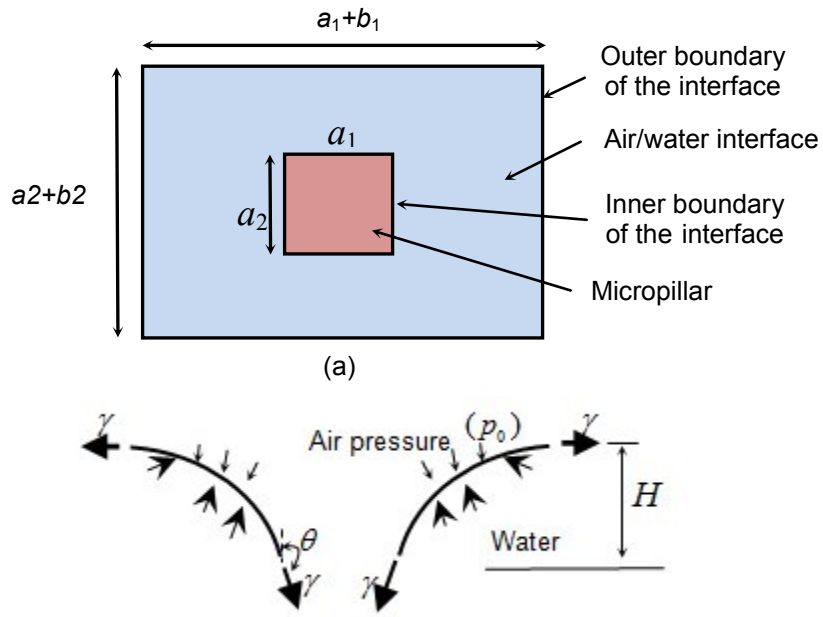

Figure 5.3: (a) Part of the air/water interface around a micropillar (bottom view of the solid fragment), and (b) free-body diagram of this part of the air/water interface (cross-sectional view).

Accordingly, *H* is much smaller than $(h+t+t_p)$. Thus, water pressure on the air/water interface has a constant value of $[p_0+\rho_w g(h+t+t_p)]$. The balance of the forces along the vertical direction leads to

$$\rho_w g(a_1 b_2 + b_1 a_2 + b_1 b_2)(h+t+t_p) = -2(a_1+a_2)\gamma\cos\theta. \tag{5.5}$$

This equation is equivalent to Eq. (14) in reference 68 when the latter equation is applied here. With the aid of Eqs. (1) and (5), it follows from Eq. (5.2) that

$$F = \rho_w g(V_s + S_p t_p) - (\rho_s g V_s + n\rho_p g a_1 a_2 t_1). \tag{5.6}$$

The first term on the right-hand side of this equation represents the buoyancy (it equals the weight of the displaced water), and the second term denotes the total weight of the solid fragment and the micropillars. Thus, *F* represents the difference between the buoyancy and the total weight of the micropillar-incorporated fragment.

In case we do not have any air trapped between the micropillars, the buoyancy becomes smaller and is $\rho_w g(V_s + na_1 a_2 t_p)$. If we further assume that $\rho_p = \rho_s$ (i.e., the solid fragment and the micropillars have the same density), then Eq. (5.4) becomes

$$F = (\rho_w - \rho_s) g(V_s + na_1 a_2 t_p). \tag{5.7}$$

This equation implies that, when there is no air trapped between the micropililars, whether the fragment rises up to water surface depends on the density difference between water and the micropillar-incorporated fragment. If $\rho_s > \rho_w$, then the fragment sinks down to the water bottom. Otherwise, it is suspended inside water (when $\rho_s = \rho_w$) or gets back to water surface (when $\rho_s < \rho_w$). In addition, as observed from Eq. (5.6), surface tension does not directly contribute to the buoyancy. Its role is to prevent water from getting into the gaps between micropillars, retaining the volume of trapped air and consequently increasing buoyancy.

Eq. (5.6) can also be derived by considering free-body diagram of an object that consists of the fragment, micropillars, trapped air, and water located in the neighborhoods of air/water interfaces (Fig. 5.5d). Along the vertical direction, this object suffers two forces: gravity, and water pressure-induced force. According to Inequality (5.4), the portion of water that is included in the considered object has a small volume in comparison with the object, and consequently its weight is neglected in considering the gravity of the object. It is readily shown that the balance of the forces along the vertical direction also leads to Eq. (5.6).

Let V_p and V_a represent the volumes of all the pillars and the trapped air, respectively. We have

$$V_p = na_1 a_2 t_p,\ V_a = S_p t_p - V_p. \tag{5.8}$$

According to these two equations, two simple design criteria are given below for increasing V_a:

(i) increase the micropillar-covered region by increasing the spacings between micropillars when the number, heights and cross-sectional areas of micropillars

are fixed, and, on the other hand, there exist limits for these spacings (i.e. b_1 and b_2), which will be discussed in Sub-section 5.2.2; and

(ii) increase the micropillar heights when the micropillar-covered region, the number and cross-sectional areas of micropillars are fixed.

Set V_{acr} to be the critical value of V_a for *F*=0. Then, by Eqs. (5.6) and (5.8), we

$$V_{acr} = \frac{(\rho_s - \rho_w)V_s + (\rho_p - \rho_w)V_p}{\rho_w}. \tag{5.9}$$

Following the two design criteria used to increase V_a , we derive the minimum area of micropillar-covered region, $S_{p\min}$, and the minimum micropillar height, $t_{p\min}$, that can make a solid fragment get back to water surface when other geometric parameters are fixed. With the aid of Eq. (5.8), it follows from Eq. (5.9) that

$$S_{p\min} = \frac{(\rho_s - \rho_w)V_s + \rho_p V_p}{\rho_w t_p}, \tag{5.10}$$

$$t_{p\min} = \frac{(\rho_s - \rho_w)V_s}{\rho_w S_p - \rho_p A}, \tag{5.11}$$

where *A* represents the total cross-sectional area of micropillars and equals na_1a_2 when the micropillars are rectangular. Both Eqs. (5.10) and (5.11) are equivalent to Eq. (5.9), and give the design criteria, respectively, for S_p and t_p when all other geometric parameters are fixed for a given solid fragment.

5.2.2 The case when the gaps between micropillars are partially filled with water

When the spacing between two neighboring micropillars is large, water may get into the gap between these two micropillars. The gaps between micropillars have both side and top openings. As shown in Fig. 5.5b, the widths of the side openings are b_1 and b_2 , while the

largest size of a top opening is $\sqrt{b_1^{\,2} + b_2^{\,2}}$. Thus, it is easier for water to penetrate into the gaps through the top openings. To avoid the penetration of water into these gaps, by Eq. (5.5) and according to the range of θ (i.e., $90^0 < \theta \le \theta_e$), it is readily shown that b_1 and b_2 should meet the condition $(a_1 b_2 + b_1 a_2 + b_1 b_2) \le \dfrac{-2(a_1 + a_2)\gamma \cos\theta_e}{\rho_w g(h + t + t_p)}$ when other parameters in this inequality are fixed. The inequality also defines the possible values of b_1 and b_2 that can be chosen for the first design criterion given in Sub-section 5.2.1. It also follows from Eq. (5.5) that, when the dimensions of the solid fragment, as well as contact angles, are given, the critical water pressure, p_{wcr} , for this penetration to occur is

$$p_{wcr} = p_0 - \frac{2(a_1 + a_2)\gamma \cos\theta_e}{(a_1 b_2 + b_1 a_2 + b_1 b_2)}. \tag{5.12}$$

When this pressure is reached, $\theta = \theta_e$. Two points can be observed from Eq. (5.12). First, when θ_e is less than $90°$ (i.e., the micropillar surface is hydrophilic), p_{wcr} is lower than p_{o} . Water pressure at or below water surface is equal to or larger than p_{o} . Hence, during the process of immersing a micropillar-covered fragment, once the heads of micropillars have contact with water, water pressure is higher than p_{wcr} . Subsequently, water gets into the gaps between micropillars from the top openings of these gaps. The air that pre-exists in these gaps may be driven away through the side openings of the gaps that have not been sealed by water. Consequently, no much air may be trapped into these gaps after the corresponding fragment is completely immersed in water. Accordingly, the volume of the trapped air is small, and may not contribute much to buoyancy. Hence, the micropillar surface should not be hydrophilic. Second, when θ_e is larger than 90^0 (i.e., the micropillar surface is hydrophobic), p_{wcr} is higher than p_{o}

. With the aid of Eq. (5.12), it is readily shown that the critical depth, h_{cr}, for water pressure to reach p_{wcr} is

$$h_{cr} = \frac{-2(a_1 + a_2)\gamma \cos\theta_e}{\rho_w g(a_1 b_2 + b_1 a_2 + b_1 b_2)} - (t + t_p). \tag{5.13}$$

$(h_{cr} + t + t_p)$ represents the critical water depth that the micropillar heads are located when water penetration occurs. It can be observed from Eq. (5.13) that, when the dimensions and distances of micropillars are in the same order, $(h_{cr} + t + t_p)$ increases with the decrease in the geometric sizes of the micropillars. In practical applications, the dimensions and distances of micropillars may be in the order of 10 μm or 100 μm. In case these geometric sizes have the same order of 10 μm, by Eq. (5.13) the order of $(h_{cr} + t + t_p)$ ranges from 0 to 1 m when θ_e varies between $90°$ and $180°$. If these geometric sizes have the same order of 100 μm, then the order of $(h_{cr} + t + t_p)$ ranges from 0 to 0.1 m when θ_e changes from $90°$ to $180°$. In these calculations, the values of γ, ρ_w, and *g* were set to be 72.8 mN/m, 10^3 kg/m^3 and 9.8 N/kg, respectively.

When micropillars are completely immersed inside water, the micropillar-covered region is surrounded by water. Once water penetrates into the gap between the micropillars, the air that pre-exists in the gaps between the micropillars has nowhere to escape. This trapped air is compressed due to the penetration of water. The degree of compression depends on water depth. Next, we determine the critical water depth, $\overline{h}_{cr}$, that makes the volume of compressed air decrease to V_{acr}. When a solid fragment is released at this critical depth, it is not able to rise up to water surface. The following three assumptions are made in deriving $\overline{h}_{cr}$: (i) the air/water interface does not have contact with the bottom of the gaps (this assumption is true due to the requirement given in Inequality (5.4); (ii) water slowly moves into the gaps (this holds when the

solid fragment is pressed deep inside water at a low speed); and (iii) air is not dissolved in water during the compression.

Based on the first two assumptions, air/water interfaces are stationary on the side surfaces of micropillars. Accordingly, we have $\theta = \theta_e$. Let p_a and V_{ac}, respectively, denote the pressure and volume of compressed air. It follows from the third assumption that the ideal gas law is applicable here. Thus, we have

$$p_a V_{ac} = p_0 V_a . \tag{5.14}$$

Considering the force balance on the portion of air/water interface shown in Fig. 5.6, replacing p_0 and θ with p_a and θ_e, respectively, and assuming that the penetration depth of water is much smaller than $(h + t + t_p),$ with the aid of Eq. (5.11) we have

$$p_a = p_0 + \rho_w g(h - h_{cr}). \tag{5.15}$$

By Eqs. (5.14) and (5.15), we get

$$V_{ac} = \frac{p_0 V_a}{p_0 + \rho_w g(h - h_{cr})}. \tag{5.16}$$

This equation is valid only when the trapped air is compressed (i.e., $h > h_{cr}$). If $h \le h_{cr}$, then V_{ac} equals V_a and is constant since the trapped air is not compressed. However, if $h > h_{cr}$, then V_{ac} is less than V_a and decreases with the increase in h. These results imply: (i) when $h \le h_{cr}$ the buoyancy is constant, and (ii) if $h > h_{cr}$ then the buoyancy decreases with the increase in water depth. Finally, in terms of Eqs. (5.9), (5.12) and (5.16), we derive the expression of $\bar{h}_{cr}$:

$$\bar{h}_{cr} = \frac{p_0}{\rho_w g}\left(\frac{V_a}{V_{acr}} - 1\right) + h_{cr}. \tag{5.17}$$

It is observed from this equation that, even if V_a is only slightly larger than V_{acr}, then the corresponding $\bar{h}_{cr}$ is still large. For example, when V_a is $1.1V_{acr}$, the first term on the right-hand side of Eq. (5.17) is 1.02 m, indicating that $\bar{h}_{cr}$ is larger than 1.02 m. Accordingly, the compression of trapped air due to water penetration is not a concern when the corresponding fragment is employed in a place that has a water depth less than 1 m.

5.2.3 The situation that circular micropillars are employed to increase buoyancy

In this sub-section, we consider the situation when circular micropillars are employed to increase the buoyancy of a solid fragment. Let *r* denote the radius of a circular micropillar (Fig. 5.1c). Let c_1 and c_2 denote the distances between neighboring micropillars along two lateral dimensions, respectively. Following the same line of reasoning as those in Sub-sections 5.2.1 and 5.2.2, we found that the expressions of V_{acr}, $S_{p\min}$, $t_{p\min}$ and $\bar{h}_{cr}$ in the case of circular micropillars are the same as those for the case of rectangular micropillars since these expressions do not involve particular geometric dimensions of micropillars. On the other hand, due to the involvement of the geometric dimensions, the expressions of $H_{\max}$ and h_{cr} have to be changed for the case of circular micropillars as follows:

$$H_{\max} = \frac{[\sqrt{(c_1+2r)^2+(c_2+2r)^2}-2r](1-\sin\theta_e)}{2\cos\theta_e}, \tag{5.18}$$

$$h_{cr} = \frac{-2\pi r\gamma\cos\theta_e}{\rho_w g[c_1c_2+2(c_1+c_2)r+(4-\pi)r^2]} - (t+t_p), \tag{5.19}$$

which are different from their counterparts in the case of rectangular micropillars. According to Eq. (5.19), the following three understandings that we have gained about $(h_{cr}+t+t_p)$ in the case of rectangular micropillars still apply to the case of circular micropillars: (i) when the dimensions and distances of circular micropillars are in the same order, $(h_{cr}+t+t_p)$ increases with the decrease in the geometric sizes of the micropillars, (ii) if geometric sizes of

circular micropillars have the same order of 10 μm, then the order of $(h_{cr}+t+t_p)$ ranges from 0 to 1 m when θ_e varies between $90°$ and $180°$, and (iii) when these geometric sizes have the same order of 100 μm, the order of $(h_{cr}+t+t_p)$ ranges from 0 to 0.1 m when θ_e changes from 90° to 180°. In addition, since the expression of $\overline{h}_{cr}$ in the case of circular micropillars is the same as that in the case of rectangular micropillars, the compression of trapped air also does not affect that the corresponding fragment gets back to water surface in shallow water.

In summary, according to the above considerations about the cases of rectangular and circular micropillars, in order to have a released solid fragment rise up to water surface, two requirements have to be met: (i) V_a should be larger than V_{acr}, and (ii) *h* should be less than $\overline{h}_{cr}$. When V_a is designed to be relatively larger than V_{acr} (e.g., V_a >1.1 V_{acr}), the second requirement is automatically met in shallow water (e.g., water with a depth below 1 m) since the corresponding value of $\overline{h}_{cr}$ is larger than the maximum water depth. In addition, to avoid the penetration of water into gaps between micropillars, *h* should be less than h_{cr}. Eqs. (5.9)-(5.11), (5.13) and (5.17) give the expressions of V_{acr}, $S_{p\min}$, $t_{p\min}$, h_{cr}, and $\overline{h}_{cr}$, respectively, for the case of rectangular micropillars, and Eqs. (5.9)-(5.11), (5.19) and (5.17) give the expressions of V_{acr}, $S_{p\min}$, $t_{p\min}$, h_{cr}, and $\overline{h}_{cr}$, separately, for the case of circular micropillars. These equations are important results of this work.

5.3 Fabrication Of Micropillar-Incorporated Fragments

In this chapter, SU-8 100 was chosen as the structural material for both solid fragments and micropillars due to two reasons. First, SU-8 is a negative photoresist. It has been widely applied in the MEMS area for various structures, including gears [69], wheels [70], reservoirs [71], boats [9] and flotillas [13]. SU-8 can be patterned to desired shapes using ultra-violet (UV)

lithography, and its thicknesses can be controlled to produce SU-8 fragments and micropillars with proper thicknesses and heights. Second, the density of SU-8 was measured to be 1.16×10^3 kg/m^3, higher than that of water (10^3 kg/m^3). This meets the requirement that the micropillar-incorporated solid fragment should be more dense than water for the purpose to validate the derived theoretical relationships, such as Eq. (5.8).

The fabrication of a micropillar-incorporated SU-8 fragment is as follows:

1. Spin-coat S1813 at 1000 rpm for 30 s on a Si wafer.
2. Slowly place a transparency on the S1813-coated Si wafer from one edge of this wafer to the other edge, and make sure the transparency has good contact with the S1813. Bake the sample on a hot plate at 100°C for 60 s.
3. Spin-coat a first SU-8 layer on the transparency at a speed of 1000 rpm, pre-bake it at 65°C for 30 min followed by baking it at 95°C for 2.5 hrs, and expose the SU-8 to UV light through a mask. The exposure energy is 700 $\mathrm{mJ/cm^2}$, and the first SU-8 layer is about 200 μm thick. This SU-8 layer is exposed but not etched. Only the portion of the SU-8 that later serves as the solid fragment is exposed, and the exposed area is defined using the corresponding pattern on the mask.
4. Spin-coat a second SU-8 layer on the first SU-8 film and expose the second SU-8 layer to UV light through another mask. The spinning speed and exposure time are selected according to [72] in order to generate micropillars with desired heights. The portion of the SU-8 that is exposed serves as micropillars after the fabrication, and the exposed area is again defined employing the pattern on the corresponding mask.
5. Post-bake the entire sample first at 65°C for 5 min then at 95°C for 45 min.
6. Develop it in SU-8 developer for over 2 hrs, which removes the unexposed SU-8 in the sample.

7. Finally, spin-coat teflon on micropillars, dissolve S1813 using acetone, and remove the transparency, together with the generated fragment, from the Si wafer.

Two masks were used in the fabrication for patterning the solid fragment and micropillars, respectively. SU-8 is hydrophilic. Its intrinsic contact angle was measured to be $80°$. To make micropillar surfaces become hydrophobic, micropillars were coated with a thin layer of teflon in the third fabrication step. According to our measurement, the intrinsic contact angle was 105° on a teflon-coated SU-8 surface. At the end of the fabrication process, the SU-8 fragment was released from the substrate using a new method that our group has developed [73]. The transparency had a circular shape of diameter 4.5 in, which was a little wider than a 4 in Si wafer for easily grabbing the edge of this transparency and peeling it off from the substrate in the fabrication third step. The transparency was stable during the fabrication process, i.e., no damages were observed visually when it was exposed to the employed chemicals such as acetone, S1813, SU-8 and SU-8 developer. This transparency was cut out of a normal transparent film used for presentation slides. S1813 is a positive photoresist. The intermediate unexposed S1813 layer between the transparency and the substrate served as the adhesion layer to make the transparency have the intimate contact with the Si wafer. Also, it served as the UV light adsorption layer, and good SU-8 patterns were generated accordingly. When the transparency was directly placed on the Si substrate, air gaps might exist between the transparency and the Si wafer, reflecting the UV light improperly from the Si wafer to the SU-8 layer during exposure, generating poor patterns. The transparency, together with the SU-8 fragment, were released from the Si substrate via etch of S1813 using acetone. After that, the micropillar-incorporated SU-8 fragment was easily separated from the transparency underneath even by hands.

After the transparency was carefully placed on the S1813, we did not visibly observe any air bubbles between these two layers. In case there existed any bubbles, they could be removed by putting the sample in a vacuum environment. After the SU-8 structures had been

developed, air bubbles might be present due to multiple baking processes involved in the fabrication, which expanded the sizes of the tiny air gaps that pre-existed between the transparency and S1813. These air bubbles actually favored the etching of S1813 because they increased the distances between the transparency and S1813 at their spots, making acetone have easier access to S1813. During the process of releasing the transparency, together with the SU-8 fragment, from the substrate, as what was done in [74], a surgical knife (or razor, or something with a very thin edge) was employed to lift the edge of the transparency a little bit every several minutes. The reason to do so is that, although S1813 is dissolved in acetone, part of the released transparency above the dissolved S1813 may become stuck to the substrate, which prevents the acetone from further dissolving the remaining layer of S1813. Since the surgical knife just had contact with the transparency, not the SU-8 fragment, the lifting process did not damage the SU-8 fragment, which was also the reason why the transparency was introduced to aid in the releasing process. Within 20 min, the transparency, together with the SU-8 fragment could be removed from the substrate.

We also used another approach to release the SU-8 fragments. In this approach, these fragments were fabricated on an S1813-coated Si wafer, which eliminated the use of a transparency. At the end of the fabrication, we found that it was difficult to etch S1813 using acetone. The etching stopped at the perimeter of the SU-8 fragment due to the deflection of the released SU-8 structure. Accordingly, acetone did not have direct contact with S1813. To solve this etch-stopping problem, the sample was placed in boiling water (instead of in heated acetone since acetone is easy to evaporate). S1813 was dissolvable in the boiling water. Also, due to dramatic movement of water, the deflection of the released SU-8 structure could not completely block the contact of water with S1813. Accordingly, the SU-8 fragment was removed from its substrate after it had been put in the boiling water for over 3 hrs. Compared with the transparency-based releasing approach, this method is straightforward and eliminates the use of the transparency, while takes a much longer time to accomplish the releasing process.

Four micropillar-covered SU-8 fragments were fabricated using the aforementioned three-step procedure. A representative fragment generated is shown in Fig. 5.4b. All the four fragments have rectangular shapes. Their length and width are in the mm scale while their thicknesses are in the micro scale. The whole bottom of each fragment is covered by 100×100 μm^2 square micropillars with a space of 100 μm. The dimensions of the four micropillar-covered SU-8 fragments are given in Table 5.1. They have slight difference in their lengths, widths, thicknesses, and masses. For simplicity, the four micropillar-covered SU-8 fragments are called Fragments 1, 2, 3 and 4, respectively, according to their order listed in Table 5.1. The micropillars on the four fragments have different heights. Accordingly, different amounts of air are trapped in these micropillars, resulting in different increases in the buoyant forces of the fragments.

The strategy used to design the micropillars includes two steps: (i) select the spacings, widths and lengths of micropillars and the micropillar-covered regions, and (ii) make sure that the heights of fabricated micropillars are much larger than $H_{\max}$ and $t_{p\min}$, which are calculated using Eqs. (5.3) and (5.11), respectively. The calculated values of $H_{\max}$ are 9.3 μm, while the predicted values of $t_{p\min}$ are between 57.8 and 63.6 μm (Table 5.1). Both the values of $H_{\max}$ and $t_{p\min}$ are much smaller than the heights of the corresponding micropillars that were fabricated.

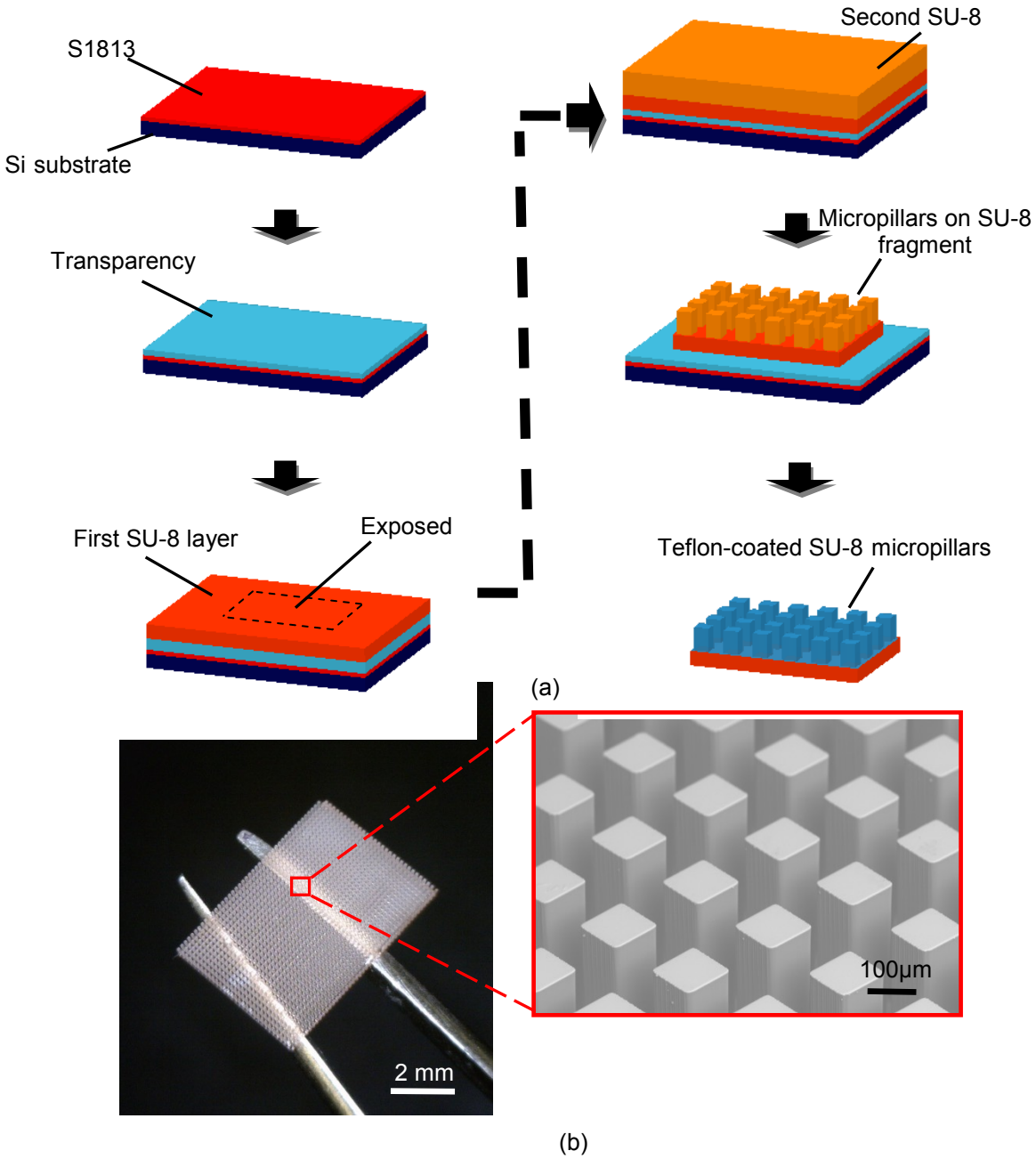

Figure 5.4: (a) Procedure to fabricate a micropillar-incorporated SU-8 fragment (not to scale). (b) Perspective view of a fabricated SU-8 fragment with micropillars (left) and SEM picture of 100 X 100 μm^2 micropillars (right).

5.4 Experimental Results And Discussions

Two points were particularly examined through experiments using the four fragments: (i) whether these fragments could get back to water surface after they are released under water, and (ii) whether Eqs. (5.9) and (5.10) could give good predictions of V_{acr} and $S_{p\min}$, respectively. All the fragments were tested in a transparent glass beaker with a diameter of 5 cm and a height of 8 cm. This beaker was partially filled to a depth of 5.5 cm with distilled water. A stainless steel ruler was placed in the center of the beaker to measure the water depth at which a fragment was released (Fig. 5.5). The rising or sinking process was recorded by a camcorder (model: SONY HDR-XR 500 with 30 frames per second). The video was then played in software Adobe Premiere Elements 3.0 for detailed analysis. Three video clips (one related to Fig. 5.5 and two corresponding to Fig. 5.6) are provided as supporting information.

5.4.1 SU-8 fragments with increased buoyancies

Figure 5.5 shows a typical test that was conducted to examine whether a SU-8 fragment could rise up to water surface from under water. In this test, a fragment was initially placed on water surface (Fig. 5.5a). Due to the effect of surface tension, it could still float on the water surface although its density was higher than that of water. A pair of tweezers was used to press the fragment into water. After this solid fragment was released from the pair of tweezers at the water depth of 2.0 cm, it got back up to the water surface in 0.1 s. According to our tests, all the four SU-8 fragments rose up to water surface even if they were released from the beaker bottom (the corresponding water depth was 5.5 cm). These results indicate that the buoyant forces of the four fragments are larger than their weights, and that the incorporation of micropillars into a SU-8 fragment increases its buoyancy and makes it able to move back to water surface.

The values of V_{acr}, h_{cr}, and $\bar{h}_{cr}$ of the four fragments were determined, respectively, using Eqs. (5.9), (5.12) and (5.17) and given in Table 5.1. Take Fragment 1 as an example.

These values were 3.3 mm^3, 2.6 cm and 58.8 m, respectively, which imply: (i) the minimum volume of the trapped air that makes Fragment 1 rise up from under water was 3.3 mm^3; (ii) the minimum water depth for water to get into gaps between micropillars was 2.6 cm; and (iii) the critical water depth for this fragment to sink down to water bottom is 58.8 m. In the case of Fragment 1, the value of V_a was 17.9 mm^3, larger than the minimum required value of 2.7 mm^3. Furthermore, the maximum water depth at which Fragment 1 was released was 5.5 cm, less than the critical water depth of 58.8 m. In Sub-section 5.3.3, two requirements were given for a released fragment to get back to water surface from under water. According to the above comparisons, these two requirements are met for Fragment 1. The same applies to another three fragments. Thus, in our experiments, all the four fragments rose up to water surface after they were released inside water.

In addition, as shown in Fig. 5.6, a silver sheet was observed at the surface of the micropillar-covered region when a fragment was placed under water. As indicated in reference [74], the air/water interface at the top of micropillars reflected light, showing a silver color. On the other hand, we did not observe such a silver sheet on the other side of the fragment which did have any micropillars. These observations imply that air was trapped in between micropillars when a fragment was submerged into water. Due to the trapped air, buoyancy was increased, thus making the fragment capable of moving back to water surface.

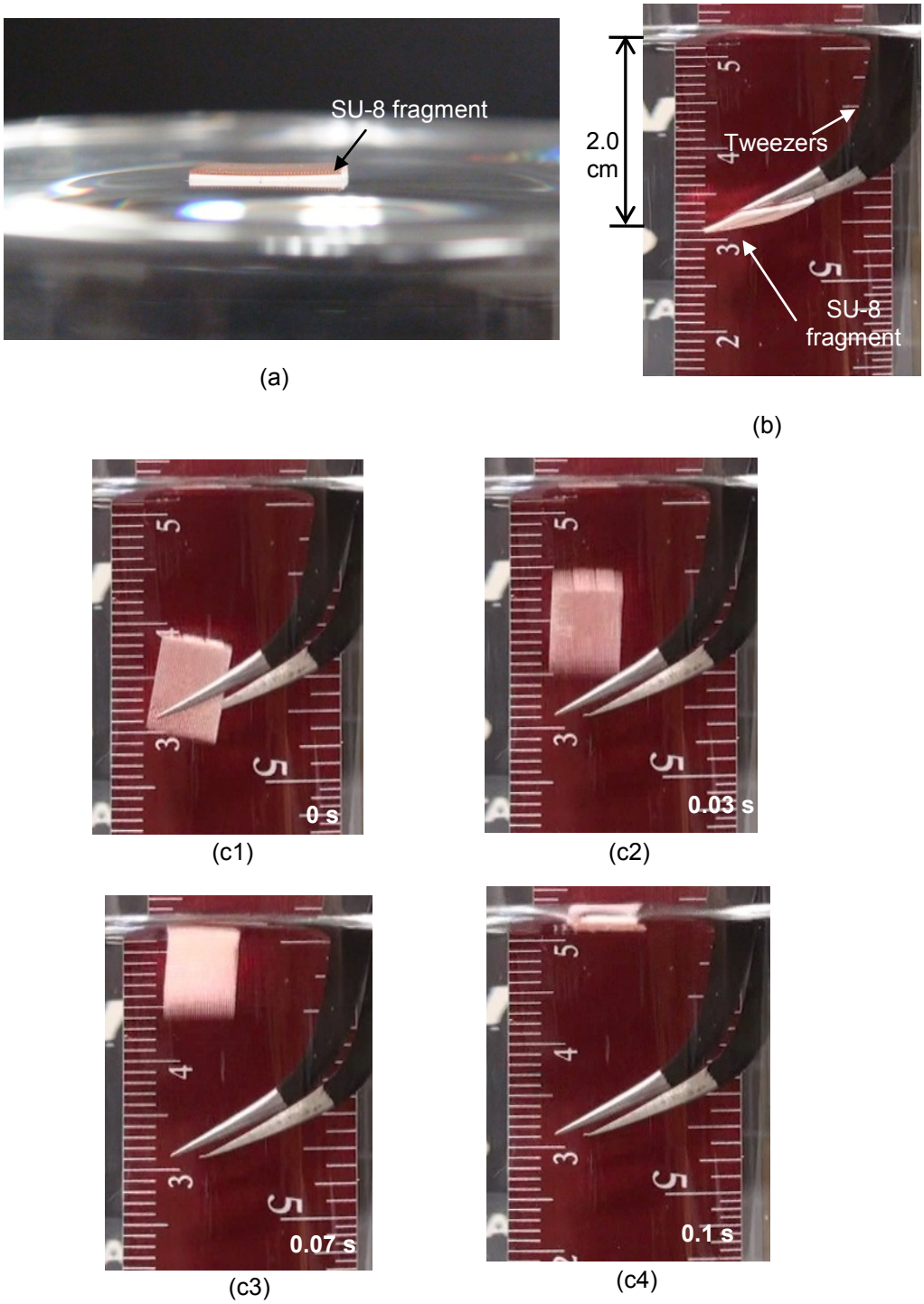

Figure 5.5: (a) A SU-8 fragment was floating on the water surface. (b) This fragment was compressed down to 2 cm below water surface. The snapshots recording the processing of fragment rising up from the water depth of 2 cm: (c1) at 0 s, (c2) at 0.03 s, (c3) at 0.07 s and (c4) at 0.1 s.

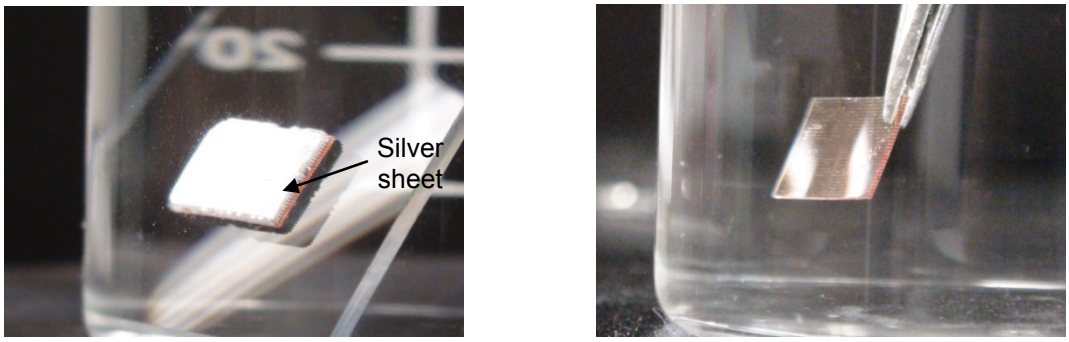

(a) (b)

Fig. 5.6: (a) A silver sheet was observed on the side of the solid fragment that had micropillars. (b) Such a silver sheet was not observed on a smooth SU-8 surface that did not have any micropillars. (A related video clip is provided as supporting information).

5.4.2 Validation of Eqs. (5.9) and (5.10)

We also validated Eqs. (5.9) and (5.10) using the four fragments. For this purpose, we compared experimentally determined V_{acr} and $S_{p\min}$ with the ones predicted using Eqs. (5.9) and (5.10), respectively. The values of V_a and S_p of the four fragments were much larger than the theoretically predicted V_{acr} and $S_{p\min}$ (Table 5.1). Take Fragment 1 as an example again. To experimentally determine V_{acr}, its V_a was reduced by decreasing S_p. The value of S_p was gradually decreased by removing a portion of micropillars with a razor as follows (Fig. 5.7): (i) under an optical microscope carefully removed some micropillars from Fragment 1 (Fig. 5.7a), (ii) test whether the resulting fragment could still rise up to water surface when it was released at a water depth less than 2 cm, which was smaller than the theoretically predicted h_{cr} of 2.6 cm, (iii) if yes continued to remove micropillars until the resulting fragment sank down to water bottom after release (Figs. 5.8b and 5.8c). As shown in Fig. 5.8a, Fragment 1 could still get back to water surface when its S_p was reduced to 9.09 mm^2. However, when its S_p was further reduced to 9.00 mm^2, it sank down to water bottom after release (Fig. 5.8b). These

results imply that $S_{p\min}$ was between 9.00 and 9.09 mm^2, close to the theoretical value of 9.13 mm^2 determined using Eq. (5.6). Accordingly, the experimentally determined value of V_{acr} was between 3.06 to 3.10 mm^3, close to the theoretical value of 3.04 mm^3 that was calculated using Eq. (5.9). Another three fragments were also tested in this manner. As shown in Table 2, the corresponding experimentally determined values of V_{acr} and $S_{p\min}$ were also close to the theoretically predicted ones, indicating that Eqs. (5.9) and (5.10) give good predictions of V_{acr} and $S_{p\min}$, respectively.

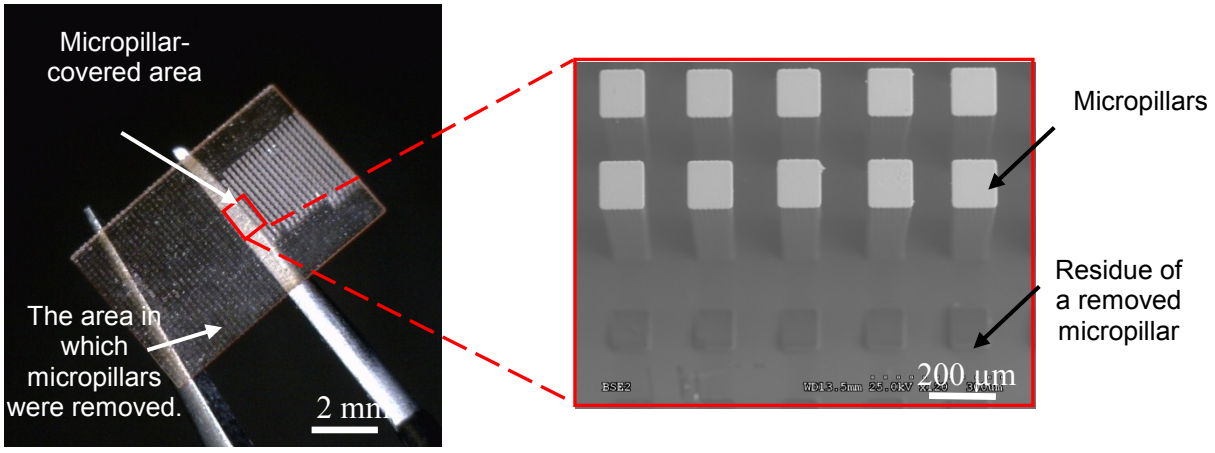

(a)

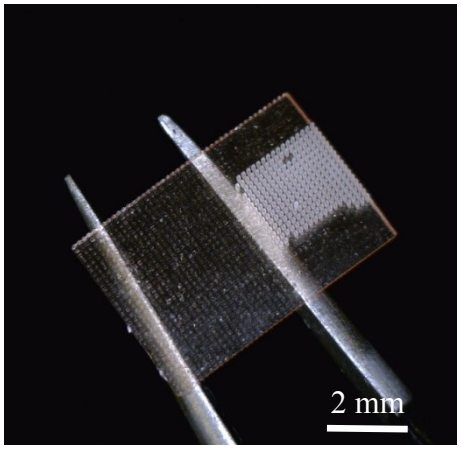

(b)

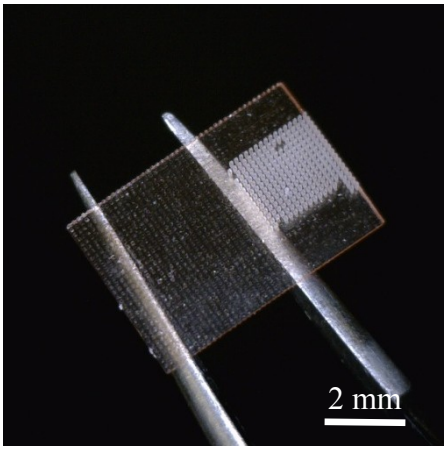

(c)

Figure 5.7: Micropillar-covered area of Fragment 1 was reduced to (a) 9.24 mm^2, (b) 9.12 mm^2, and (c) 9.00 mm^2, respectively, after gradually removing micropillars, (a), (b) and (c) are optical images while the insert in (a) is a SEM picture.

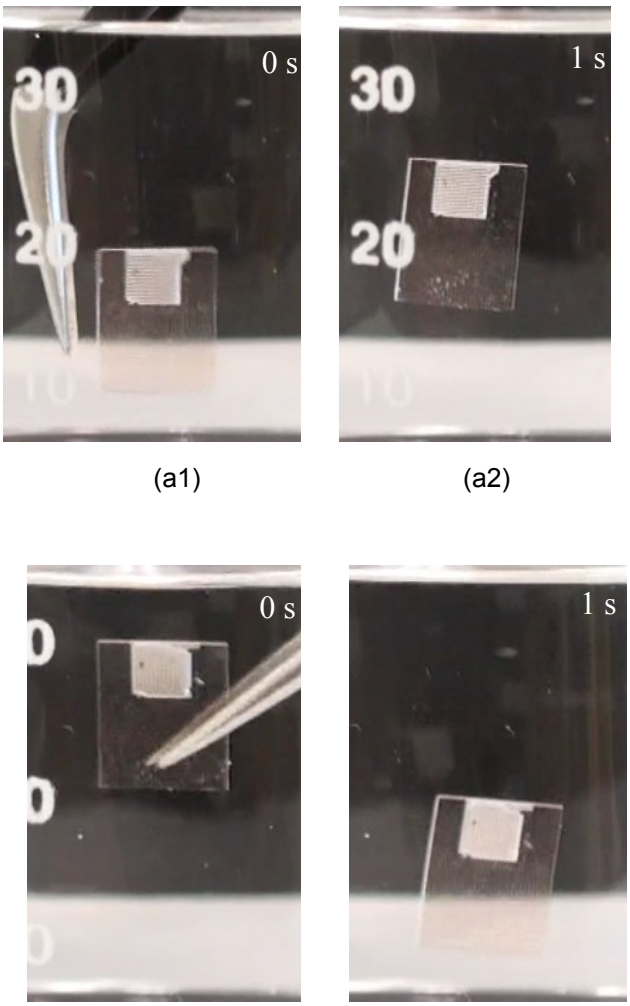

Figure 5.8: Tests to determine whether Fragment 1 still rose up to water surface after its S_p was reduced. Two snapshots (a1) at 0 s and (a2) at 1 s after the release from tweezers when S_p of Fragment 1 was reduced to 9.09 mm^2. Two snapshots (b1) at 0 s and (b2) at 1 s after the release from tweezers when S_p of Fragment 1 was reduced to 9.00 mm^2 (two corresponding video clips are provided as supporting information).

Table 5.1: Measured and calculated results of four micropillar-covered SU-8 fragments.

Sample	Fragment			Total mass of fragment and pillars (mg)	Pillars		
	Length (mm)	Width (mm)	Thickness (μm)		t_p (μm)	$t_{p\min}$ (μm)	$H_{\max}$ (μm)
1.	8.80	6.06	200	14.7	445	57.8	9.3
2.	8.80	6.04	202	14.8	371	58.4	9.3
3.	8.84	6.05	200	14.0	263	57.8	9.3
4.	9.06	6.06	220	16.4	466	63.6	9.3

Table 5.1 – *Continued*

Sample	Trapped air volume		Area of pillars region		Pillars	
	V_a (mm^3)	V_{acr} (mm^3)	S_p (mm^2)	$S_{p\min}$ (mm^2)	h_{cr} (cm)	$\overline{h_{cr}}$ (m)
1.	17.9	3.3	53.3	9.13	2.6	58.8
2.	14.8	3.1	53.2	10.40	2.6	50.6
3.	10.6	2.8	53.5	12.78	2.6	37.6
4.	19.2	3.5	54.9	9.36	2.6	56.7

Table 5.2: Measured and calculated results of four micropillar-covered SU-8 fragments whose micropillars were partially removed.

Sample	Area of micropillar-covered region		Volume of trapped air	
	Measured V_{acr} (mm^3)	Calculated V_{acr} (mm^3)	Measured S_p (mm^2)	CalculatedS_{pmin} (mm^2)
1.	3.06—3.10	3.04	9.00—9.09	9.13
2.	2.97—3.01	2.89	10.77—10.86	10.40
3.	2.42—2.48	2.52	11.88—11.97	12.78
4.	3.15—3.19	3.27	9.22—9.29	9.36

5.5 Design of parameters

Incorporation of micropillars would make trapping air on the surface of an object possible. This layer of air will lower the average density of the object and make it float up in water. Based on aforementioned equations, the parameters can be selected according to the needs of applications. The increase of buoyancy generated by micropillars is determined by its dimensional parameters including length a_1, width a_2, thickness t_1, covered area of the micropillars S_1 and spacing between micropillars b_1 and b_2. The spacing can be determined first because it decides whether water will be trapped between micropillars or not. Theoretically, the thickness of the pillars must be lower than the critical depth of the micropillars. The critical depth can be determined by Eq. 4.13. If this condition does not apply, the water will penetrate into gaps of micropillars before the water seal the sides of micropillars. Consequently, some area of gaps of micropillars will be filled with water. For the sake of safety, we choose the spacing a_2 and b_2 around 100 μm. Based on our experimental results, this value can make sure the trapping of air even though under the condition of the external vibration. The density of

the micropillars is considered as a constant of ρ_p.

If the mass, volume and the surface area can be covered with pillars (width and length are given) of the object are known as M_1, V_1 and S_1 ($W_1 \times L_1$), the dimension of the micropillars can be calculated following procedures:

(i) Initially choose a_1 and a_2 with a value larger than the minimum dimension of adopted fabrication approach (1 μm in our case). Also, they have to satisfy the inequality

$$\frac{\rho_w (a_1 + b_1)(a_2 + b_2)}{\rho_p a_1 a_2} > 1. \tag{5.20}$$

This condition makes sure each unit less dense than water (Fig. 5.6a).

(ii) Choose the thickness of the micropillars. The aspect ratio of the micropillar is determined by t_1 / a_1. If the aspect ratio is higher than 10 there are difficulties in fabrication. Also, it can overcome lower external force and broken easily. Therefore, we choose the aspect ratio as 5 or lower than 5.

(iii) Calculated the row m_1 and column n_1 of micropillars based on

$$m_1 = \frac{W_1 + b_2}{a_2 + b_2}, n_1 = \frac{L_1 + a_1}{a_1 + b_1}. \tag{5.20}$$

(iv) Verify the dimensions of micropillars with two sub steps:

(a) The inequality must satisfied in order to guarantee the buoyancy is larger than the gravity of the object

$$\rho_w (V_1 + t_1 S_1) g - (M_1 + \rho_p a_1 a_2 t_1 m_1 n_1) g = C > 0 \tag{5.21}$$

If $C < 0$, go back to the step (i) and choose new a_1 and a_2 with a smaller dimension. To achieve a maximum loading capacity, a larger C is preferred.

(b) The $\bar{h}_{cr}$ can be determined by Eq. 5.17. If the calculated $\bar{h}_{cr}$ is higher than

the required $\bar{h}_{cr}$, the design of the dimension of pillars finished. Otherwise, we need to go back to step (i) and decrease the value of the a_1 and a_2. If the minimum value of a_1 and a_2 cannot satisfy one of above conditions, this method may not applicable for the current design.

The procedures given above can be followed to design the micropillar layer. The spacing and dimensions of the pillars are chosen as two design parameters when the area of the micropillars is known.

5.6 Summary and Conclusions

In this chapter, through theoretical and experimental investigations, we demonstrated the possibility of applying micropillars to make a solid fragment, which has a higher density than water, to rise up to water surface from under water. Air was trapped in between micropillars, enlarging the volume of displaced water and thus increasing buoyancy. The critical values of trapped air, micropillar-covered area, micropillar height and water depth for a micropillar-incorporated fragment to get back to water surface were formulated. Two requirements were given for such a fragment to have a buoyant force larger than its weight. The critical point is to make the volume of trapped air much larger than the minimum required volume. Consequently, the corresponding fragment could even rise up to water surface in deep water. Four micropillar-incorporated SU-8 fragments were fabricated and tested. The experimentally determined critical values of micropillar-covered areas and trapped air volumes had good match with theoretically predicted ones. In addition, through force analysis, we showed that surface tension did not provide a supporting force when a fragment was completely immersed in the water. Instead, the role of surface tension was to retain the volume of trapped air. Since the incorporation of the micropillars may make a heavy fragment get back to water surface from under water, the presented results have potential applications in developing miniaturized devices, such as submarines and water robots, that may need to rise up to water surface.

CHAPTER 6

SUMMARY AND CONCLUSIONS

In summary, this dissertation aims to (i) test translational and rotational motions of microboats, (ii) investigate the circular motions of microboats with rudders, (iii) introduce a technique to reduce the drag and enhance the loading capacity of microboat or microsubmarine and (iv) develop microsubmarines driven by thermal oscillatory approaches..

First, we demonstrated that in the chapter 2, in addition to propelling an mm-scaled SU-8 boat, Marangoni effect could also induce dramatic squat and trim phenomena in the motions of the boat. In addition, we found that the motion of the boat in a channel included two stages. In the first stage, it was propelled by surface tension gradients, accompanied with dramatic squat and trim movements. However, in the second stage, in which the propellant was used up, the boat was driven by a water wave, generated in the first stage. These results might also apply to surface tension-driven motions of other miniaturized objects.

Second, in chapter 3 we developed a type of microboats that had side rudders. Eight microboats were tested. The lengths of their rudders ranged from 0 to 10 mm. Experimental results demonstrate: (i) through a side rudder, it is feasible to control the radial motion of a microboat; (ii) the radius of a radial motion decreases as the length of a rudder increases; and (iii) the total travel distance and the maximum speed both decrease as the length of a rudder increases. A theoretical model was also developed to consider the motions of these microboats. The corresponding numerical results had a reasonably good agreement with the experimental results, and the mismatch between numerical and experimental results increased with the length of the side rudder due to the simplified consideration in the simulation.

Third, through experimental and theoretical investigations, we developed the prototype of a micro submarine based on a thermally oscillatory approach of propulsion. We investigated the design, fabrication, actuation and horizontal motions of this prototype. The prototype had a thermally oscillatory process similar to that of the putt-putt toy boat. The propulsive parameters were optimized. At an applied voltage of 16 V, pulse frequency of 100 Hz, and duty of 50%, the submarine was found to have the speed as high as 1.8 mm/s and the travel distance as long as 12.6 mm. The corresponding thrust was calculated to be 67.6 nN. Also, it was considered that the constraint of the wire connections limited the travel distance of the submarine. Thus, in the near future, we plan to develop wirelessly powered submarine to eliminate this constraint. Furthermore, in this work, we focus on the horizontal motions of the submarine. In the near future, we also plan to explore its vertical motions (i.e., rising and sinking under liquid), as well as and corresponding design, based on our recent work, which used trapped bubbles to increase buoyancy for the purpose of raising a small object from under liquid.

Forth and finally, SU-8 fragment with micropillars was designed, generated and tested. through theoretical and experimental investigations, we demonstrated the possibility of applying micropillars to make a solid fragment, which has a higher density than water, to rise up to water surface from under the water. Air was trapped in between micropillars, enlarging the volume of displaced water and thus increasing buoyancy. The critical values of trapped air, micropillar-covered area, micropillar height and water depth for a micropillar-incorporated fragment to get back to water surface were formulated. Two requirements were given for such a fragment to have a buoyant force larger than its weight. The critical point is to make the volume of trapped air much larger than the minimum required volume. Consequently, the corresponding fragment could even rise up to water surface in deep water. Four micropillar-incorporated SU-8 fragments were fabricated and tested. The experimentally determined critical values of micropillar-covered areas and trapped air volumes had good match with theoretically predicted ones. In addition, through force analysis, we showed that surface tension did not provide a supporting force when

a fragment was completely immersed in the water. Instead, the role of surface tension was to retain the volume of trapped air. Since the incorporation of the micropillars may make a heavy fragment get back to water surface from under water, the presented results have potential applications in developing miniaturized devices, such as submarines and water robots, that may need to rise up to water surface.

REFERENCES

[1] Donald B R, Levey C G, Mcgray C D, Paprotny I and Rus D 2006 An untethered, electrostatic, globally controllable MEMS micro-robot *Microelectromechanical Systems, Journal of* **15** 1-15

[2] Ebefors T, Mattsson J U, Kälvesten E and Stemme G 1999 A walking silicon micro-robot *Proc. Transducers' 99*: Citeseer pp 1202-1205

[3] Hollar S, Flynn A, Bellew C and Pister K S J 2003 Solar powered 10 mg silicon robot *Micro Electro Mechanical Systems, 2003. MEMS-03 Kyoto. IEEE The Sixteenth Annual International Conference on*: pp 706-711

[4] Yamakita M, Kamamichi N, Kaneda Y, Asaka K and Luo Z-W 2003 Development of artificial muscle actuator using ionic polymer with its application to biped walking robots *Smart Structures and Materials*: International Society for Optics and Photonics pp 301-308

[5] Karpelson M, Gu-Yeon W and Wood R J 2008 A review of actuation and power electronics options for flapping-wing robotic insects *Robotics and Automation, 2008. ICRA 2008. IEEE International Conference on*: pp 779-786

[6] Miki N and Shimoyama I 1999 Magnetic rotational micro-wings applicable to microrobots *Intelligent Robots and Systems, 1999. IROS'99. Proceedings. 1999 IEEE/RSJ International Conference on*: IEEE pp 721-726

[7] Wood R J 2007 Liftoff of a 60mg flapping-wing MAV *Intelligent Robots and Systems, 2007. IROS 2007. IEEE/RSJ International Conference on*: IEEE pp 1889-1894

[8] Wood R J 2008 The first takeoff of a biologically inspired at-scale robotic insect *Robotics, IEEE Transactions on* **24** 341-347

[9] Luo C, Li H and Liu X 2008 Propulsion of microboats using isopropyl alcohol as a propellant *Journal of Micromechanics and Microengineering* **18** 067002

[10] Luo C, Qiao L and Li H 2010 Dramatic squat and trim phenomena of mm-scaled SU-8 boats induced by Marangoni effect *Microfluidics and Nanofluidics* **9** 573-577

[11] Qiao L, Xiao D, Lu F K and Luo C 2012 Control of the radial motion of a self-propelled microboat through a side rudder* *Sensors and Actuators A: Physical*

[12] Liu X, Li H, Qiao L and Luo C 2011 Driving mechanisms of CM-scaled PDMS boats of respective close and open reservoirs *Microsystem Technologies* **17** 875-889

[13] Li H, Qiao L, Liu X and Luo C 2012 Fabrication and testing of a self-propelled, miniaturized PDMS flotilla *Microsystem Technologies* **18** 1431-1444

[14] Li H and Luo C 2011 Development of a self-propelled microflotilla *Microsystem Technologies* **17** 777-786

[15] Neinhuis C and Barthlott W 1997 Characterization and distribution of water-repellent, self-cleaning plant surfaces *Annals of Botany* **79** 667-677

[16] Schönherr J 1982 Resistance of plant surfaces to water loss: transport properties of cutin, suberin and associated lipids *Physiological Plant Ecology* **2** 153-179

[17] Singh R A, Yoon E-S, Kim H J, Kim J, Jeong H E and Suh K Y 2007 Replication of surfaces of natural leaves for enhanced micro-scale tribological property *Materials Science and Engineering: C* **27** 875-879

[18] Onda T, Shibuichi S, Satoh N and Tsujii K 1996 Super-water-repellent fractal surfaces *Langmuir* **12** 2125-2127

[19] Bico J, Marzolin C and Quéré D 1999 Pearl drops *EPL (Europhysics Letters)* **47** 220

[20] Nosonovsky M and Bhushan B 2005 Roughness optimization for biomimetic superhydrophobic surfaces *Microsystem Technologies* **11** 535-549

[21] Joseph P, Cottin-Bizonne C, Benoit J-M, Ybert C, Journet C, Tabeling P and Bocquet L 2006 Slippage of water past superhydrophobic carbon nanotube forests in microchannels *Phys Rev Lett* **97** 156104

[22] Enright R, Eason C, Dalton T, Hodes M, Salamon T, Kolodner P and Krupenkin T 2006 Friction factors and Nusselt numbers in microchannels with superhydrophobic walls: *ASME* pp

[23] Manz A, Graber N and Widmer H 1990 Miniaturized total chemical analysis systems: a novel concept for chemical sensing *Sensors and Actuators B: Chemical* **1** 244-248

[24] Nguyen N T and Wu Z 2005 Micromixers—a review *Journal of Micromechanics and Microengineering* 15 R1

[25] Deshmukh A A, Liepmann D and Pisano A P 2000 Continuous micromixer with pulsatile micropumps *Technical Digest of the IEEE Solid State Sensor and Actuator Workshop (Hilton Head Island, SC)*: vol 736

[26] Tsai J-H and Lin L 2002 Active microfluidic mixer and gas bubble filter driven by thermal bubble micropump *Sensors and Actuators A: Physical* **97** 665-671

[27] Shuxiang G, Fukuda T and Asaka K 2003 A new type of fish-like underwater microrobot *Mechatronics, IEEE/ASME Transactions on* **8** 136-141

[28] Wang Z, Hang G, Li J, Wang Y and Xiao K 2008 A micro-robot fish with embedded SMA wire actuated flexible biomimetic fin *Sensors and Actuators A: Physical* **144** 354-360

[29] Byungkyu K, Deok-Ho K, Jaehoon J and Jong-Oh P 2005 A biomimetic undulatory tadpole robot using ionic polymer–metal composite actuators *Smart Materials and Structures* **14** 1579

[30] Shuxiang G, Yarning G, Lingfei L and Sheng L 2006 Underwater Swimming Micro Robot Using IPMC Actuator *Mechatronics and Automation, Proceedings of the 2006 IEEE International Conference on*: pp 249-254

[31] Xinyan D and Avadhanula S 2005 Biomimetic Micro Underwater Vehicle with Oscillating Fin Propulsion: System Design and Force Measurement *Robotics and Automation, 2005. ICRA 2005. Proceedings of the 2005 IEEE International Conference on*: pp 3312-3317

[32] Guo S, Pan Q and Khamesee M 2008 Development of a novel type of microrobot for biomedical application *Microsystem Technologies* **14** 307-314

[33] Tao M, Yong C, Guoqiang F and Deyi K 2002 Wireless drive and control of a swimming microrobot *Robotics and Automation, 2002. Proceedings. ICRA '02. IEEE International Conference on*: pp 1131-1136

[34] Fukuda T, Hosokai H and Kikuchi I 1990 Distributed type of actuators by shape memory alloy and its application to underwater mobile robotic mechanism *Robotics and Automation, 1990. Proceedings., 1990 IEEE International Conference on*: IEEE pp 1316-1321

[35] Fukuda T, Kawamoto A, Arai F and Matsuura H 1994 Mechanism and swimming experiment of micro mobile robot in water *Micro Electro Mechanical Systems, 1994, MEMS'94, Proceedings, IEEE Workshop on*: IEEE pp 273-278

[36] Fukuda T, Kawamoto A, Arai F and Matsuura H 1995 Steering mechanism of underwater micro mobile robot *Robotics and Automation, 1995. Proceedings., 1995 IEEE International Conference on*: IEEE pp 363-368

[37] Mojarrad M and Shahinpoor M 1997 Biomimetic robotic propulsion using polymeric artificial muscles *Robotics and Automation, 1997. Proceedings., 1997 IEEE International Conference on*: IEEE pp 2152-2157

[38] Sewa S, Onishi K, Asaka K, Fujiwara N and Oguro K 1998 Polymer actuator driven by ion current at low voltage, applied to catheter system *Micro Electro Mechanical Systems, 1998. MEMS 98. Proceedings., The Eleventh Annual International Workshop on*: IEEE pp 148-153

[39] Chung S K, Ryu K and Cho S K 2009 A surface-tension-driven propulsion and rotation principle for water-floating mini/micro robots *Micro Electro Mechanical Systems, 2009. MEMS 2009. IEEE 22nd International Conference on*: IEEE pp 1083-1086

[40] Song Y S and Sitti M 2007 Surface-tension-driven biologically inspired water strider robots: theory and experiments *Robotics, IEEE Transactions on* **23** 578-589

[41] Thomson J 1855 XLII. On certain curious motions observable at the surfaces of wine and other alcoholic liquors *The London, Edinburgh, and Dublin Philosophical Magazine and Journal of Science* **10** 330-333

[42] Scriven LE and Sternling CV 1960 The Marangoni effects. *Nature* **167**186–188

[43] Osada Y, Gong J, Uchida M and Isogai N 1995 Spontaneous motion of amphoteric polymer gels on water *Japanese journal of applied physics* **34** L511-L512

[44] Gong J, Matsumoto S, Uchida M, Isogai N and Osada Y 1996 Motion of polymer gels by spreading organic fluid on water *The Journal of Physical Chemistry* **100** 11092-11097

[45] Mitsumata T, Ikeda K, Gong J P and Osada Y 2000 Controlled motion of solvent-driven gel motor and its application as a generator *Langmuir* **16** 307-312

[46] Bassik N, Abebe B T and Gracias D H 2008 Solvent driven motion of lithographically fabricated gels *Langmuir* **24** 12158-12163

[47] Ku C M, Liao H H and Yang Y J 2011 MEMS-based buoyancy and propelling mechanisms for a micro-submarine *IEEE International Conference on Nano/Micro Engineered and Molecular Systems (NEMS) (Taiwan, Kaohsiung)* pp 744-747

[48] Wang J M, Lin T Y and Yang L J 2007 Electrohydrodynamic (EHD) micro-boat *IEEE International Conference on Nano/Micro Engineered and Molecular Systems (NEMS) (Thailand, Bangkok)* pp 584-587

[49] Mita Y, et al. 2009 Demonstration of a wireless driven MEMS pond skater that uses EWOD technology *Solid-State Electronics* **53** 798-802

[50] Constantine T 1960 On the movement of ships in restricted waterways *Journal of Fluid Mechanics* **9** 247-257

[51] Dand I and Ferguson A 1973 Squat of full ships in shallow water *Naval Architect* **15** 237–255

[52] Millward A and Bevan M 1986 The behaviour of high speed ship forms when operating in water restricted by a solid boundary *Royal Institution of Naval Architects Transactions* **128**

[53] Schofield R and Martin L 1988 MOVEMENT OF SHIPS IN RESTRICTED NAVIGATION CHANNELS *ICE Proceedings*: Ice Virtual Library pp 105-120

[54] Sheng ZB, Liu YZ (eds) 2003 Principles of ships (part I). Publishers of Shanghai Jiao Tong University, Shanghai, China, pp 293–301 (in Chinese)

[55] Su M 2007 Liquid mixing driven motions of floating macroscopic objects *Appl Phys Lett* **90** 144102-144102-3

[56] Varyani K 2006 Squat effects on high speed craft in restricted waterways *Ocean engineering* **33** 365-381

[57] Vazquez G, Alvarez E and Navaza J M 1995 Surface tension of alcohol water+ water from 20 to 50. degree. C *Journal of chemical and engineering data* **40** 611-614

[58] Munson B R, Young D F, Okiishi T H and Huebsch W W 1998. *Fundamentals of fluid mechanics*, Wiley New York.

[59] Keller J B 1998 Surface tension force on a partly submerged body *Physics of Fluids* **10** 3009

[60] Hu D L, Chan B and Bush J W 2003 The hydrodynamics of water strider locomotion *Nature* **424** 663-666

[61] Extrand C and Moon S I 2009 Will It float? Using cylindrical disks and rods to measure and model capillary forces *Langmuir* **25** 2865-2868

[62] Nosonovsky M and Bhushan B 2005 Roughness optimization for biomimetic superhydrophobic surfaces *Microsystem Technologies* **11** 535-549

[63] Lafuma A and Quéré D 2003 Superhydrophobic states *Nature materials* **2** 457-460

[64] Liu X and Luo C 2010 Fabrication of super-hydrophobic channels *Journal of Micromechanics and Microengineering* **20** 025029

[65] Oliver J, Huh C and Mason S 1977 Resistance to spreading of liquids by sharp edges *Journal of Colloid and Interface Science* **59** 568-581

[66] Luo C, Xiang M, Liu X and Wang H 2011 Transition from Cassie–Baxter to Wenzel States

on microline-formed PDMS surfaces induced by evaporation or pressing of water droplets *Microfluidics and Nanofluidics* **10** 831-842

[67] Extrand C 2004 Criteria for ultralyophobic surfaces *Langmuir* **20** 5013-5018

[68] Zheng Q-S, Yu Y and Zhao Z-H 2005 Effects of hydraulic pressure on the stability and transition of wetting modes of superhydrophobic surfaces *Langmuir* **21** 12207-12212

[69] Lorenz H, Despont M, Vettiger P and Renaud P 1998 Fabrication of photoplastic high-aspect ratio microparts and micromolds using SU-8 UV resist *Microsystem Technologies* **4** 143-146

[70] Dellmann L, et al. 1998 Two steps micromoulding and photopolymer high-aspect ratio structuring for applications in piezoelectric motor components *Microsystem Technologies* **4** 147-150

[71] Luo C, et al. 2006 Thermal ablation of PMMA for water release using a microheater *Journal of Micromechanics and Microengineering* **16** 580

[72] Information on fabrication procedure of SU-8 100: www.microchem.com/pdf/SU8_50-100.pdf.

[73] Luo C, Meng F and Francis A 2006 Fabrication and application of silicon-reinforced PDMS masters *Microelectron J* **37** 1036-1046

[74] Luo C, Govindaraju A, Garra J, Schneider T, White R, Currie J and Paranjape M 2004 Releasing SU-8 structures using polystyrene as a sacrificial material *Sensors and Actuators A: Physical* **114** 123-128

[75] Larmour I A, Bell S E and Saunders G C 2007 Remarkably simple fabrication of superhydrophobic surfaces using electroless galvanic deposition *Angewandte Chemie* **119** 1740-1742

[76] Tang W C, Nguyen T-C H and Howe R T 1989 Laterally driven polysilicon resonant microstructures *Sensors and Actuators* **20** 25-32

[77] Fan L-S, Tai Y-C and Muller R S 1989 IC-processed electrostatic micromotors *Sensors and Actuators* **20** 41-47

[78] Yan J, Avadhanula S, Birch J, Dickinson M, Sitti M, Su T and Fearing R 2001 Wing transmission for a micromechanical flying insect *Journal of Micromechatronics* **1** 221-237

[79] Barnaby K C 1967 *Basic Naval architecture* 5th *edition* (London: Hutchinson)

[80] Crane J 1984 *Submarine* (London: British Broadcasting Corp.)

[81] Satchell D 1987 Silicon microengineering for accelerometers *Int. Conf. on the Mechanical Technology of Inertial Devices (Newcastle, England)* vol 1 pp 191-193

[82] Venkatesh S and Culshaw B 1985 Optically activated vibrations in a micromachined silica structure *Electronics Letters* **21** 315-317

[83] Andres M, Tudor M and Foulds K 1987 Analysis of an interferometric optical fibre detection technique applied to silicon vibrating sensors *Electronics Letters* **23** 774-775

[84] Greenwood J 1984 Etched silicon vibrating sensor *Journal of Physics E: Scientific Instruments* **17** 650

[85] Nathanson H C, Newell W E, Wickstrom R A and Davis Jr J R 1967 The resonant gate transistor *Electron Devices, IEEE Transactions on* **14** 117-133

[86] Petersen K E and Guarnieri C 1979 Young's modulus measurements of thin films using micromechanics *J Appl Phys* **50** 6761-6766

[87] Ikeda K, Kuwayama H, Kobayashi T, Watanabe T, Nishikawa T, Yoshida T and Harada K 1990 Silicon pressure sensor integrates resonant strain gauge on diaphragm *Sensors and Actuators A: Physical* **21** 146-150

[88] Wang W, Yao Z, Chen J C and Fang J 2004 Composite elastic magnet films with hard magnetic feature *Journal of Micromechanics and Microengineering* **14** 1321

[89] Dijkink R, Van Der Dennen J, Ohl C and Prosperetti A 2006 The'acoustic scallop': a bubble-powered actuator *Journal of Micromechanics and Microengineering* **16** 1653

[90] Bass V The pop-pop pages (http://www.nmia.com/~vrbass/pop-pop/)

[91] Finnie I and Curl R L 1963 Physics in a toy boat *American Journal of Physics* **31** 289-293

[92] Lorenz H, Despont M, Vettiger P and Renaud P 1998 Fabrication of photoplastic high-aspect ratio microparts and micromolds using SU-8 UV resist *Microsystem Technologies* **4** 143-146

[93] Dellmann L, et al. 1998 Two steps micromoulding and photopolymer high-aspect ratio structuring for applications in piezoelectric motor components *Microsystem Technologies* **4** 147-150

[94] Luo C, et al. 2006 Thermal ablation of PMMA for water release using a microheater *Journal of Micromechanics and Microengineering* **16** 580

[95] Nijdam A, et al. 2005 Fluidic encapsulation in SU-8μ-reservoirs with μ-fluidic through-chip channels *Sensors and Actuators A: Physical* **120** 172-183

[96] Gadre A, et al. 2004 Fabrication of a fluid encapsulated dermal patch using multilayered SU-8 *Sensors and Actuators A: Physical* **114** 478-485

[97] Mark J 1999 *Polymer Data Handbook* (New York: Oxford Univ. Press)

[98] Xia Y and Whitesides G M 1998 Soft lithography *Annual review of materials science* **28** 153-184

[99] Gere J and Timoshenko S 1990 *Mechanics of Materials* (Boston: PWS Publishing)

[100] Qiao L, Xiang M and Luo C 2012 Increase buoyancy of a solid fragment using micropillars *Sensors and Actuators A: Physical* **182** 136-145

[101] Wenzel R N 1936 RESISTANCE OF SOLID SURFACES TO WETTING BY WATER *Industrial & Engineering Chemistry* **28** 988-994

[102] Cassie A B D and Baxter S 1944 Wettability of porous surfaces *Transactions of the Faraday Society* **40** 546-551

BIOGRAPHICAL INFORMATION

Lei Qiao received his BS degree in July 2008 from the School of Mechanical Engineering and Automation at Beihang University (BUAA) in China. During his undergraduate studies, he worked in Robotic Institute at BUAA as a research assistant and team leader to develop a robot used for exploring a harsh environment. His Bachelor's thesis is regarding how to solve Boolean combinations of numerical constraints. He has been a PhD student in the Department of Mechanical and Aerospace Engineering Department at the University of Texas at Arlington since the fall of 2008. His research interests are mainly related to development and testing of microactuators, including driving mechanism and motion control of microboats and microsubmarines. In the future, he would like to pursue a career in semiconductor industry.